EXPLORING THE ROBUSTNESS OF ORGANIC PHOTOVOLTAICS: MATERIALS, PROCESSING, AND STABILITY

Stephanie Samson

A dissertation submitted to the faculty of the University of North Carolina at Chapel Hill in partial fulfillment of the requirements for the degree of Doctor of Philosophy in the Department of Applied Physical Science in the College of Arts and Sciences.

Chapel Hill
2022

Approved by:

Jinsong Huang

Wubin Bai

Theo Dingemans

Sergei Sheiko

Wei You

ABSTRACT

Stephanie Samson: Exploring the Robustness of Organic Photovoltaics: Materials, Processing, and Stability
(Under the direction of Wei You)

Due to their unique properties, organic photovoltaics (OPVs) are more suitable than their inorganic counterparts in niche technologies requiring properties like flexibility, low-light/indoor efficiency, semi-transparency, and light weight. However, despite rapidly approaching the oft-cited 20% PCE benchmark for commercial viability, OPVs still lack the low cost and long lifetimes required for even niche applications. In this dissertation, we explored the contributions of processing, materials, and stability to the potential commercial viability of OPVs. We first aimed to demonstrate potential cost reduction through robustness against material variability. Through this and previous work with collaborators, we found that the morphologies (and PCEs) of systems using donor polymer PBnDT-FTAZ with various acceptors were insensitive to MWs ranging 30 kg/mol to 120 kg/mol. Such insensitivity can eliminate the need for tight MW control during synthesis, reducing costs. We then investigated the tolerance of OPVs to impurities. If material does not have to be entirely pure, this could be another cost reduction avenue. Using P3HT:PC$_{61}$BM as a model system, we investigated the effect and ultimate fate of solid additives. We found the system was remarkably tolerant to a gamut of acidic, basic, neutral, and even ionic species. Furthermore, despite high melting and boiling points of these solid additives, they were largely absent in the bulk active layer following device fabrication. Thus, not only did this study demonstrate the remarkable additive tolerance of P3HT:PC$_{61}$BM, but it also revealed that even high melting and boiling point solids may be volatilized and removed during typical OPV processing. Lastly, we explored methods of stabilizing morphology to increase lifetime. Utilizing P3HT copolymers integrating thermocleavable side chains (TCS), we demonstrated a polymer:fullerene system with remarkable thermal stability while maintaining PCE ~1.5%. As opposed to previous work wherein 100% of side chains were thermocleavable, this work demonstrated that a TCS density of 60% was more than sufficient for thermal stability while still affording appreciable PCE. Together, these works can inform OPV material selection and processing towards manufacture and use in commercial applications.

ACKNOWLEDGEMENTS

First, I would like to express my sincere thanks to my advisor, Professor Wei You, for his support over the last five years. With his guidance, enthusiasm, knowledge, and immense patience, he always helped push me in the right direction and was truly instrumental in making this work possible. I could not have asked for a better advisor. I would also like to thank my committee members, Professor Jinsong Huang, Professor Wubin Bai, Professor Theo Dingemans, Professor Scott Warren, and Professor Sergei Sheiko for their time, feedback, and support.

Second, I would like to thank the members of the You group and our collaborators. In particular, I would like to thank Dr. Liang Yan and Dr. Nicole Bauer for helping me learn about and work with organic semiconductor materials and for always being willing to answer my questions. Next, I would like to thank Dr. Jeromy Rech, Dr. Sungyun Son, Justin Neu, Jordan Shanahan, and Xiaowei Zhong for making and characterizing many of the materials used in this work and for helping me with additional experiements. I would also like to thank our collaborators in Professor Ade’s group at NCSU, especially Dr. Xhengxing Peng, Dr. Kan Ding, and Reece Henry for performing GIWAXS and RSoXS and aiding us with the data analysis.

I would also like to acknowledge CHANL, especially Dr. Carrie Donley who trained me on techniques and measured data essential to parts of this work, and the graduate school and NREL for financial support of this work.

Finally, I would like to thank my family and friends for their love and support.

TABLE OF CONTENTS

LIST OF TABLES

LIST OF FIGURES

LIST OF ABBREVIATIONS AND SYMBOLS

BHJ	Bulk heterojunction
3TZA	3-thiophene carboxylic acid
AFM	Atomic force microscopy
Al	Aluminum
AN	1-aminonapthalene
BA	benzoic acid
c-Si	Crystalline silicon
Ca	Calcium
CFL	Compact fluorescent light
CN	1-chloronapthalene
CS State	Charge separated state
CT State	Charge transfer state
CuSCN	Copper thiocyanate
CV	Cyclic voltammetry
Đ	Dispersity
D:A	Donor:Acceptor
D18	Poly[(2,6-(4,8-bis(5-(2-ethylhexyl-3-fluoro)thiophen-2-yl)-benzo[1,2-b:4,5-b’]dithiophene))-alt-5,5'-(5,8-bis(4-(2-butyloctyl)thiophen-2-yl)dithieno[3',2':3,4;2",3":5,6]benzo[1,2-c][1,2,5]thiadiazole)]
DIO	diiodooctane
EL	Electroluminescence
EQE	External quantum efficiency
ETL	Electron transport layer
FF	Fill Factor

FoM	Figure of merit
FREA	Fused ring electron acceptor
FTAZ	Shorthand for PBnDT-FTAZ, unless otherwise stated
FTIR	Fourier transform infrared spectroscopy
GIWAXS	Grazing incidence wide-angle X-ray scattering
HOMO	Highest occupide molecular orbital
HTL	Hole transport layer
I	Intensity
IC-SAM	4-[(1,3-dioxoinden-2-ylidene)methyl] benzoic acid
iFoM	Industrial figure of merit
ITIC	3,9-bis(2-methylene-(3-(1,1-dicyanomethylene)-indanone))- 5,5,11,11-tetrakis(4-hexylphenyl)-dithieno[2,3-d:2’,3’-d’]-s- indaceno[1,2-b:5,6-b’]dithiophene
ITO	Indium-doped tin oxide
J-V	Current Density-Voltage
J_{SC}	Short circuit current
k_B	Boltzmann's constant, 1.380649×10^{-23} J·K^{-1}
LED	Light emitting diode
LUMO	Lowest unoccupide molecular orbital
M_n	Number average molecular weight
MoOx	Molybdenum Oxide
MPP	Maximum power point
MW	Molecular weight
N2200	Poly{[N,N'-bis(2-octyldodecyl)naphthalene-1,4,5,8-bis(dicarboximide)-2,6-diyl]-alt-5,5'-(2,2'-bithiophene)}
NCC	Number of chromatographic column steps

NHC	Number of hazardous chemicals involved
NUO	Number of monomer isolation steps
NFA	Non-fullerene acceptor
NMR	Nuclear magnetic resonance
NSS	Number of synthetic steps
OPV	Organic photovoltaic
OSC	Organic solar cell
p	Extent of reaction
P3HT	Poly-3-hexylthiophene
PBnDT-FTAZ	poly(benzodithiophene-alt-dithienyl difluorobenzotriazole)
$PC_{61}BM$	Phenyl-C_{61}-butyric acid methyl ester
PCE	Power conversion efficiency
PCE10	Poly[4,8-bis(5-(2-ethylhexyl)thiophen-2-yl)benzo[1,2-b;4,5-b']dithiophene-2,6-diyl-alt-(4-(2-ethylhexyl)-3-fluorothieno[3,4-b]thiophene-)-2-carboxylate-2-6-diyl)]
PEDOT:PSS	poly(3,4-ethylenedioxythiophene) polystyrene sulfonate
PL	Photoluminescence
PSC	Polymer solar cell
PV	Photovoltaic
PyHCl	Pyridinium hydrochloride
RSoXS	Resonant soft X-Ray scattering
RY	Yield ratio
SAM	Self-assembled monolayer
SC	Synthetic complexity
SCLC	Space charge limited current
SEM	Scanning electron microscopy

SMA	Small molecule acceptor
STEM	Scanning transmission electron microscopy
STXM	Scanning transmission X-ray microscopy
T_{80}	Time it takes for PCE to degrade to 80% of its original value
TEM	Transmission electron microscopy
T_S	Time at which exponential burn-in has ended and linear long-term degradation begins
T_{S80}	Time it takes for PCE to degrade to 80% of PCE(T_s)
UPS	Ultraviolet photoelectron spectroscopy
V_{OC}	Open circuit voltage
XPS	X-ray photoelectron spectroscopy
ZnO	Zinc oxide
ε_0	Permitivity of free space, $8.8541878128 \times 10^{-12}$ F·m^{-1}
ε_r	Dielectric constant
Γ	Industrial figure of merit associated with the golden triangle: cost, lifetime, efficiency
μ	charge carrier mobility
Φ	Work function

CHAPTER 1: INTRODUCTION

Sunlight is a renewable resource so vast that harvesting a mere 0.002% of it would be more than sufficient to offset daily energy consumption.[1,2] Indeed, photovoltaic (PV) installations in just a few select high-insolation areas would be able to meet the world's energy needs, given a power conversion efficiency (PCE) of a mere 8%.[2] While this PCE requirement has been reached long ago, photovoltaics (or solar cells) still comprise only 15% of renewable energy generation in the United States, translating to 3% of total energy generation. However, this is not to say the potential of solar energy has gone unnoticed. While the current photovoltaic (PV) market is centered on large-scale energy generation, residential PV adoption has risen considerably over the past decade.[3–5] Furthermore, niche use cases have arisen which cannot be addressed with traditional rigid, opaque inorganic PV modules (e.g., Si). While organic photovoltaics (OPVs) lag in terms stability and technology readiness, OPVs have tunable optoelectronic and mechanical properties (due to the use of molecularly modifiable conjugated donor polymers),[6] are solution-processable at low temperatures,[7–9] have low embodied energy,[10] are lightweight,[11] are safer for the environment,[12–14] and are flexible.[15] These properties make OPVs amenable to large scale roll-to-roll production and use, and a natural candidate for integration in technologies that require mechanical compliance such as soft robotics,[16] medical sensing devices,[17] textiles,[18] and lamination to curved surfaces.[19] Unfortunately, integration into these technologies requires us to address the relatively high cost and short lifetime of OPVs.

1.1 History

Early work in OPVs was arguably traced back to the synthesis of highly-conductive polyacetylene by Shirakawa, MacDiarmid, and Heeger in 1977, [20] with the expectation that organic electronics could be cheaper, lighter, and more flexible than their inorganic counterparts. Early single-layer devices by Weinberger[21] and Marks[22] (utilizing polyacetylene and PPV, respectively) did not perform well due to inefficient exciton separation.[21] In 1986, Tang fabricated the first bilayer devices, ITO (Indium Tin Oxide)/CuPC/PV/Ag,[23] where the planar heterojunction (CuPC/PV) allowed for charge separation at the D:A interface.[24] In 1993, Sariciftci demonstrated the first bilayer polymer solar cell (ITO/MEH-PPV/C_{60}/Al)[25] with a PCE of 0.04%. This was improved upon by Halls in 1996, who simultaneously showed that the exciton diffusion length in the system was on the order ~10 nm, in line with previous findings.[26] Unfortunately, this is substantially shorter than the typical optical absorption length.[27–29] This created a dilemma: the active layer must be thick enough for sufficient light absorption while thin enough for the exciton to reach the D:A interface within its lifetime. A creative solution emerged in mid 1990s by Heeger and co-worksers,[30] where they used interpenetrating, bi-continuous networks of donor and acceptor, known as bulk heterojunctions (BHJs), to overcome this dilemma. Later patented by Sariciftci and Heeger in 1994,[31] this BHJ has quickly become the dominant architecture in modern OPVs (**Figure 1.1**). [32]

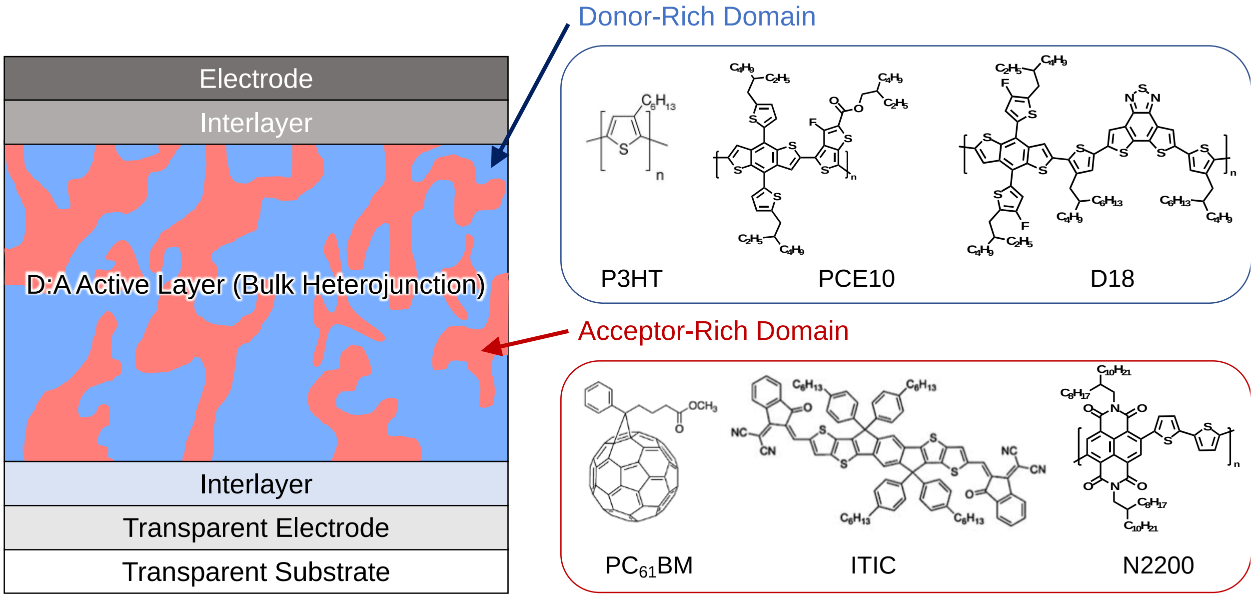

Figure 1.1. Architecture of a typical BHJ organic solar cell (left) and examples of common donor and acceptor materials (right).

Shortly after the conception of BHJs, the synthesis of soluble fullerene derivatives by Wudl and coworkers[33] further accelerated the development of the field, allowing for facile solution-phase deposition of polymer:fullerene BHJs. BHJs were then quickly brought from concept to reality in 1995 by the groups of both Heeger[34] using MEH-PPV:PCBM, and Friend[35] using MEH-PPV:CN-PPV as the D:A system. However, polymer:fullerene systems have some glaring weaknesses, including difficult and limited synthesis,[36,37] high cost,[32] weak absorption in the near-infrared (NIR),[36,37] limited energy level control,[36] and known stability/aggregation issues.[37] The alternatives, small molecule non-fullerene acceptors (NFAs) and n-type polymers, offered tunability, allowing them to alleviate many of these issues. However, interest was limited until high PCEs were demonstrated in 2011 by Loi[38] and Sirringhaus[39] using the n-type polymer acceptor P(NDI2OD-T2) and in 2015 by Zhan[40] using small-molecular NFA ITIC. In addition, the library of donor polymers was growing rapidly, with D-A (donor-acceptor) type copolymer donors showcasing the extreme tunability of polymer semiconductors and paving the way to increasingly high PCEs.[41,42] Since then, great progress has been made in the field, with PCEs for polymer:fullerene, polymer:NFA and polymer:polymer solar cells now exceeding 11%,[43] 19%,[44] and 16%,[44] respectively.

1.2. Current Challenges

The current photovoltaic (PV) market is dominated by inorganic technologies, which boast module power conversion efficiencies (PCE) around 20%,[45] lifespans exceeding 20 years,[46] and module costs approaching \$0.20/W$_p$.[47] The combination of these three metrics – efficiency, stability, and cost – comprise the golden triangle (**Figure 1.2**), a set of properties to gauge the readiness to transition from the laboratory to commercialization.[48,49] Backed by nearly 50 years of research, OPVs boast the highest the overall technology readiness level (TRL) of emerging alternative PV technology at an estimated TRL of 5-6.[50] However, despite the impressive body of OPV research, OPVs still lag behind.

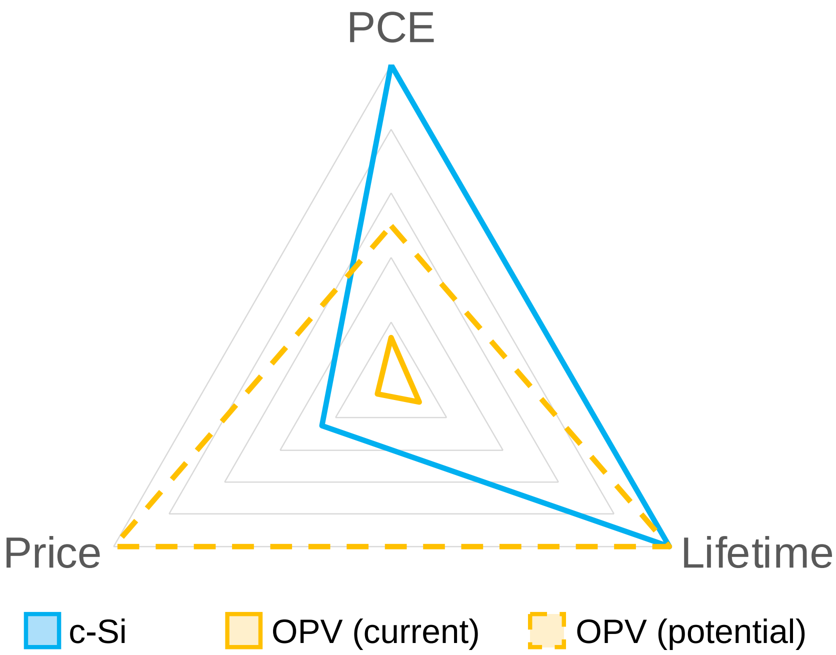

Figure 1.2. The golden triangle and the status of c-Si and OPVs. Currently, OPVs occupy only a small area in the center of the triangle, with current modules having efficiencies below 5% and associated costs more than five times that of c-Si. The dashed area represents the demonstrated potential of OPVs, though such a device has yet to be realized.

Older estimates showed that OPVs would need PCEs of 7% and lifetimes of 5 years to be competitive,[51] though new studies suggest competitive OPVs now require PCEs of 10% with 20 years lifetime at \$0.45/W_p to compete in large-scale power generation due to falling inorganic PV costs.[52] While OPVs have demonstrated module efficiencies exceeding 10%,[53] and projected lifetimes exceeding 30 years,[54] their demonstrated outdoor lifetime does not exceed 3 years.[55] In addition, despite their relatively high champion efficiencies and prevalence in the OPV field, BHJs are not necessarily as cost-effective as most literature would have us believe.[52] Currently, the materials which yield high PCEs are synthetically complex, translating to higher costs.[56] Indeed, the active layer comprises more than 80% of the total estimated manufacturing cost of OPVs, which is already more than twice that of standard commercial Si.[52] There are lower-cost options, such as the polymer donor PTQ10, which can be used in OPVs which exceed 10%.[57,58] This is more than sufficient for niche applications such as wearables and low-light/indoor applications, which require power on the order of a few mW.[17] Furthermore, under artificial indoor lighting, OPVs can perform as well as[59] or even better than[60–62] Si-based PVs. The replacement of incandescent bulbs with compact fluorescent lights (CFLs) and light emitting diodes (LEDs) has allowed OPVs to outperform their Si-based counterparts[60–62] due to superior spectral matching.[61] Indoor OPV performance can also be further improved[60] due to the large library of tunable donor and acceptor materials[62]. Additionally, their flexibility also allows OPVs to be installed where inorganic PVs typically cannot, such as lampshades or curtains.[19,61] However, the final point of the golden triangle, lifetime, remains an issue. Even in niche flexible and rigid applications where OPVs would have the advantage over inorganic PV, lifetimes 5-10 years would still be required.[63] Moreover, flexible and even stretchable applications would also require enhanced mechanical robustness beyond what would be required to withstand roll-to-roll manufacture. Unfortunately, BHJ morphology is exceedingly delicate. This morphology is sensitive to both external and internal stressors including, but not limited to, batch-to-batch variations (such as molecular weight and dispersity), the presence of impurities, interactions between OPV components, mechanical stress, moisture, oxygen, heat, and even light itself.[64,65] Thus, while OPV technology appears to be advancing steadily, the issue of robustness throughout the synthesis, manufacture, and lifetime of the device remains.

1.3. Objectives

The overarching goal of this work is to explore the robustness of OPVs. Enhancing the robustness of OPVs is a multifaceted problem. Although there is a respectable body of work[66–74] dedicated to improving and maintaining kinetically-trapped BHJ morphologies, fewer resources are dedicated to the study of OPV robustness as a whole. An OPV is composed of not only the active layer, but also the interlayers, substrate, and electrodes, making the feat of going from lab to fab a complicated affair. Ideally, a robust OPV device would achieve and maintain the same performance despite variations in processing, materials, and/or operating conditions. This is quite a broad topic, so I will break it down into three primary aims, each with a particular case study:

Aim 1: Reducing Costs by through Increased Material Robustness (Chapter 2). I will demonstrate the robustness of donor polymer PBnDT-FTAZ against variations in MW.

Aim 2: Reduce Cost through Processing Robustness (Chapter 3). In this portion, I probe the tolerance of archetypal system P3HT:PC61BM to solid-state additives and determine the ultimate fate of those additives.

Aim 3: Improve Lifetime through Morphological Robustness (Chapter 4). I will present the remarkable thermal stability of a P3HT-based polymer incorporating thermocleavable side chains.

1.4. Working Mechanism

Before discussing OPVs in further detail, it will be useful to briefly review how an OPV device works. Typically, the active layer comprises an electron-donating material (*p*-type semiconductor, or donor) and an electron-accepting material (*n*-type semiconductor, or acceptor). The energy offset between the donor highest occupied molecular orbital (HOMO) and acceptor lowest unoccupied molecular orbital (LUMO) is the interfacial energy gap, E_{I}.[37] The photoexcitation of an electron in the donor HOMO results in a tightly-bound electron-hole pair,[37] or exciton. With binding energies of ~0.3 to 1.0 eV,[32] thermal fluctuations ($k_B T = 0.025$ eV at room temperature) are insufficient to separate these excitons into free charge carriers.[75] These excitons must diffuse to the donor-acceptor (D:A) interface, where the electron transfers to the acceptor while the hole remains the donor, forming the charge transfer state (CT).[76,77] If exciton binding energy can be overcome at the interface, the CT state would become charge separated (CS) states and the generated free charge carrier can then travel through the acceptor and donor domains for collection at the electrodes.[37]

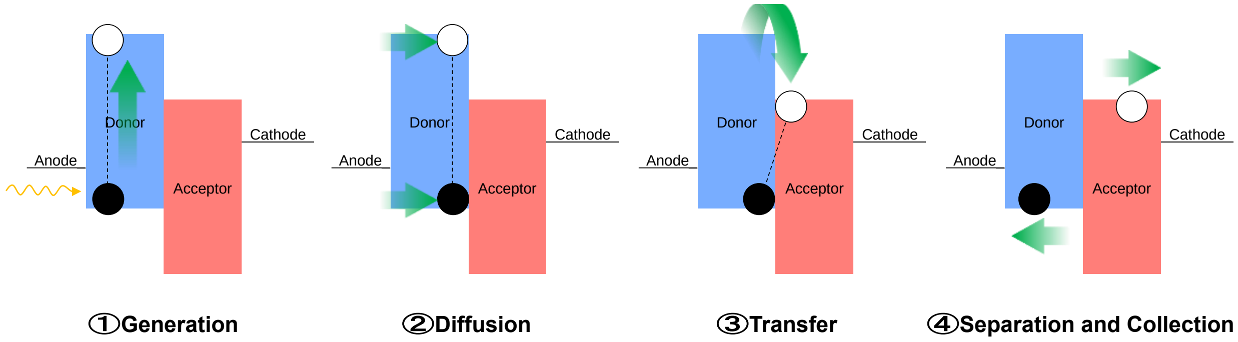

Figure 1.3. The pathway from initial excitation to ultimate charge collection. The black and white circles represent holes and electrons, respectively. The dashed line indicates that the two are still coloumbically bound as an exciton.

1.5. Photovoltaic Properties

The PCE of a solar cell is derived through three additional FoM. These FoM are open circuit voltage (V_{OC}), short-circuit current (J_{SC}), and fill factor (FF), from which power conversion efficiency (PCE) can be extracted via **Equation (1.1)** . V_{OC} is the voltage at the open-circuit condition, when current is zero. This value is primarily influenced by the energy difference between the donor HOMO and acceptor LUMO[78], but is also affected by other factors, such as the aforementioned CT state, morphology,[79] and metal contact selection.[80] J_{SC} is the current density at short-circuit condition, when voltage is zero. J_{SC} is governed by the photoelectric conversion process,[79] which includes absorption, exciton generation and diffusion, and charge generation, transport, and extraction.[78,79] FF is the ratio of the maximum power from the solar cell to the product of J_{SC} and V_{OC} and encompasses resistive losses and diode characteristics.[78,79] PCE is derived from these as

$$PCE = \frac{P_{out}}{P_{in}} = \frac{J_{SC}V_{OC}FF}{P_{in}}, \tag{1.1}$$

or the fraction of the electrical power (P_{out}) converted from the incident power (P_{in}). These FoM can be determined from the current density vs. voltage (J-V) curves obtained by plotting the photocurrent as a function of applied bias (**Figure 1.4**). Further insight can also be obtained from probing active layer morphology.

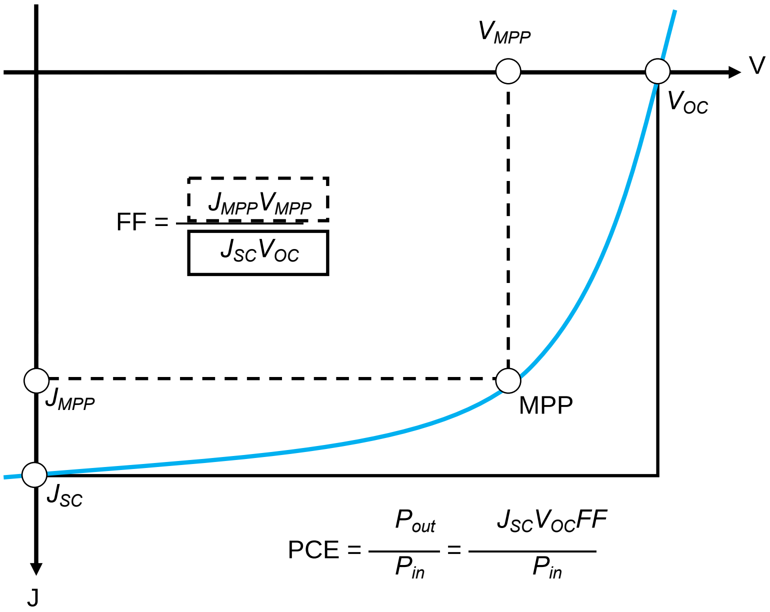

Figure 1.4. Model J-V curve. J_{MPP} and V_{MPP} correspond to the current and voltage at the point where power is maximized, the maximum power point (MPP). P_{in} and P_{out} are the power in and out, respectively.

A large variety of tools can be used to probe the morphology of BHJ active layers films. Large-scale features can be analyzed with optical microscopy. Nanoscale features are commonly probed by atomic force microscopy (AFM),[81] scanning electron microscopy (SEM),[81] transmission electron microscopy (TEM),[82] scanning transmission electron microscopy (STEM), and scanning transmission x-ray microscopy (STXM).[82] AFM and SEM provide local surface information[83] while TEM, STEM, and STXM provide local 2D projections of the 3D film morphology.[84] However, neither the surface nor projected morphology are necessarily an accurate representation of the overall inner film morphology.[81,84] Note that it is also difficult to obtain contrast between active layer components, particularly in all-polymer systems,[84] using AFM[85] or electron microscopy (SEM, STEM, TEM)[86]. These real-space measurements techniques, which provide visualization of *localized* surfaces or projected areas, are usually supplemented by measurements of the *averaged* BHJ morphology. Most commonly, x-ray scattering techniques are used to obtain statistically-relevant morphological information regarding crystallinity, long period, and relative domain purity.[86–88] Due to the prevalence of X-ray scattering techniques in general OPV literature, they will be discussed here in further detail.

1.6. Morphological Characterization

As active layers are typically composed of light elements such as C, N, and O, the typical X-ray energy used is far above the absorption edges of constituent atoms.[89] Thus, absorption probability is low and contrast is primarily derived from changes in dispersion δ related to differences in electron density. While this may provide sufficient signal for bulk samples in the commonly-used small-angle x-ray scattering (SAXS) and wide-angle X-ray scattering (WAXS), thin films in transmission geometry have very little interaction volume for scattering.[85] Unfortunately, this is compounded in OPVs, where active layers typically have a thickness of 100 to 200 nm. To remedy this, grazing incidence wide-angle X-ray scattering (GIWAXS) utilizes a grazing incidence and reflection geometry to increase scattering volume[85] while resonant soft X-ray scattering (RSoXS) utilizes resonant frequencies near absorption edges to elicit significant absorption β with concomitant increases in signal intensity and contrast.[40] In both techniques, contrast arises from differences in the energy-dependent complex refractive index, $n = 1 - \delta(\lambda) + i\beta(\lambda)$, where δ and β relate to dispersion and absorption, respectively. Furthermore, the small angle (used in GIWAXS) and long-wavelength (used in RsoXS) limits result in mathematically identical descriptions of scattering, allowing for the real-space distance r to be related to scattering vector $\mathbf{q}$ as $r = 2\pi/q$.[82]

GIWAXS is typically used to extract molecular-scale morphological information regarding crystalline domains both in and out of the sample plane.[81,85] This information is particularly useful when investigating variations in J_{SC}. With grazing incidence and reflection geometry, a hard X-ray beam can travel a sufficiently long path through the footprint effect.[83,85] The depth probed depends on incidence angle α_i and its value relative to the critical angle for total external reflection of the film and substrate (< 1° for hard X-rays[85]), $\alpha_{c,film}$ and $\alpha_{c,substrate}$. Incidence angles $\alpha_i < \alpha_{c,film}$ (~0.1° for conjugated polymers) probe the top ~10 nm surface of the film,[90] $\alpha_{c,film} < \alpha_i < \alpha_{c,substrate}$ probes structures within the entire depth of the film,[83] and $\alpha_{c,substrate} < \alpha_i$ will probe both the film and substrate.[83] The scattering collected by the detector can provide information such as the π-π stacking distance, lamellar spacing, film texture, and crystallinity.[81] For example, the film texture (edge-on vs. face-on) can be determined by the location and sharpness of the π-π stacking peak.[81] Crystalline, highly-oriented films show sharp Bragg peaks, while films with more disordered crystallites may have smeared peaks or even Debye-Sherrer-like rings.[81]

RsoXS can be used to probe mesoscale morphological information in the sample plane.[82] Tuning the x-ray energy to the resonant frequency at the absorption edge of one of the elemental constituents (~100 eV for light elements) allows for core electrons to be readily excited into unoccupied molecular orbitals.[89,91] Near these absorption edges, there are rapid, chemically-sensitive changes in both δ and β[92] which can be exploited to maximize scattering contrast.[92,93] The long period, or center-to-center domain spacing, can be extracted from peak(s) in the azimuthally-integrated intensity $I(\mathbf{q})\cdot\mathbf{q}^2$ vs. $\mathbf{q}$ plots.[82,94] Additionally, the nature of the domain interfaces can be probed by power-law fitting the high-$\mathbf{q}$ limit according to Porod's law.[82,94] Intensity falls off as $\mathbf{q}^{-4}$ for sharp, smooth interfaces, but falls off more slowly for fractal interfaces and more quickly for diffuse interfaces.[94] Furthermore, the relative domain purity for a two-phase system can be extracted from the total scattering intensity, $TSI = \int_0^\infty I(q)q^2 dq$, which is invariant with morphology but sensitive to domain contrast.[94] More mixed domains will have lower contrast, and thus lower TSI.[94] Information gleaned from RSoXS can give insight into variations in J_{SC}, V_{OC}, and *FF*.

1.7. Lifetime

The lifetime of PV technologies is quantified using the photodegradation curve.[64] (**Figure 1.5**) Contrary to what the name suggests, light is not the only cause of solar cell degradation. Degradation first occurs in a rapid, exponential decay called burn-in, which is primarily intrinsic in nature and triggered by light and heat.[64] During this initial decay called "burn-in," phase separation, interlayer degradation, trap state formation, and di-/oligomerization may all occur.[64] After decays stabilizes, the solar cell experiences long-term, linear decay, which is primarily extrinsic, triggered by heat, oxygen, and water.[64,65] Now, in addition to ongoing phase separation and interlayer degradation, photo-oxidation and electrode degradation may occur. This is ultimately followed by catastrophic failure of the device. From this photodegradation curve, we can extract two primary FoM: T_{80} and T_{S80}.

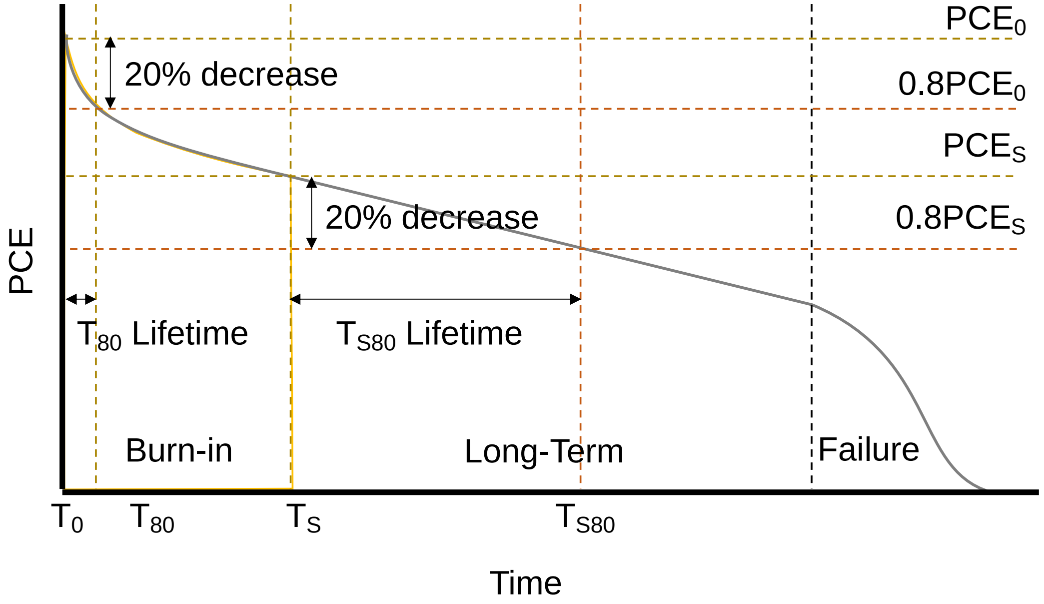

Figure 1.5. Representation of a typical photodegradation curve, featuring an exponential burn-in loss followed by long-term linear degradation until ultimate failure.

T_{80} is defined as the amount of time it takes for a solar cell to decay to 80% of its initial PCE, while T_{S80} is the amount of time it takes to decay another 20% following initial exponential burn-in.[64] Though T_{S80} will typically be longer than T_{80}, it is more straightforward to extract T_{80}. Using T_{80} to represent lifetime and synthetic complexity (SC) to represent cost, Brabec and co-workers proposed an industrial figure of merit, or iFoM,[95] designated here as Γ,

$$\Gamma = \frac{PCE \times lifetime}{cost} = \frac{PCE \times T_{80}}{SC}, \tag{1.2}$$

to evaluate the commercial viability of cells using the familiar golden triangle. SC can be quantified as proposed by Po and coworkers,[56]

$$SC \ = \ 35NSS \ + 25\log(RY) \ + \ 15NUO \ + \ 15NCC \ + \ 10NHC \tag{1.3}$$

where NSS is the number of synthetic steps, RY is the yield ratio, NUO is the number of monomer isolation steps, NCC is the number of chromatographic column steps, and NHC is the number of hazardous chemicals involved. These values are often normalized, taking chamption literature values as references. If testing does not continue long enough to reach 20% PCE decay, T_{80} can be extrapolated by fitting PCE(t) to a stretched exponential,

$$PCE(t) = PCE(0)\exp\left[-\left(\frac{t}{\tau_{deg}}\right)^{\beta}\right] \tag{1.4}$$

where t is the time, τ_{deg} is a characteristic time, and β is a fitting parameter describing the shape of the curve.[96,97] While standardized testing has been proposed,[98] such testing has not been widely adopted, leading to wildly varying methods of testing and thus varying T_{80}. Though most extrapolated T_{80} fall around 1,000 – 10,000 hours, T_{80} up to 27,000 years has been reported.[99] To further complicate matters, time constraints force testing to be accelerated by increasing temperature and/or light intensity. Temperature-dependent degradation follows an Arrhenius relation,[100,101]

$$k_{deg} = \frac{1}{\tau} = \frac{1}{T_{80}} = k_{0,T} \exp\left(-\frac{E_a}{k_B T}\right), \tag{1.5}$$

where k_{deg} is the degradation constant, τ is the characteristic lifetime (taken to be T_{80}), k_0 is a constant, E_a is the activation energy for temperature-dependent degradation, k_B is the Boltzmann constant, and T is the temperature. Degradation due to light can be expressed as a function of incident light intensity I_{test} relative to a reference intensity I_{ref} (usually 1 sun),[96,102]

$$k_{deg} = k_{ref} \left(\frac{I_{test}}{I_{ref}}\right)^{\xi}. \tag{1.6}$$

If we assume these are independent of one another, we can define an overall acceleration factor,

$$\frac{k_{deg}}{k_{ref}} = \gamma = \left(\frac{I_{test}}{I_{ref}}\right)^{\xi} \exp\left(\frac{E_a}{k_B}\left[\frac{1}{T_{ref}} - \frac{1}{T_{test}}\right]\right), \tag{1.7}$$

which can be used to relate data from accelerated trials to real time. While important data can be extracted from these accelerated tests, it is important to remember these models and assumptions may not necessarily capture all degradation factors.

CHAPTER 2: REDUCING COSTS BY THROUGH INCREASED MATERIAL ROBUSTNESS

CASE STUDY: PBNDT-FTAZ: AN MW-INSENSITIVE DONOR[1]

2.1. Synopsis

Donor polymer number average molar mass (M_n) has long been known to influence organic photovoltaic (OPV) performance via changes in the both the polymer properties and the resulting bulk heterojunction morphology. The exact nature of these M_n effects varies from system to system, though there is generally some intermediate M_n that results in optimal performance. Interestingly, our earlier work with FTAZ donor polymer, paired with either N2200 (polymer acceptor) or $PC_{61}BM$ (fullerene acceptor), demonstrated < 10% variation in power conversion efficiency (PCE) and consistent morphology over a large span of M_n (30 kg/mol to over 100 kg/mol). Would such insensitivity to polymer M_n still hold true when prevailing small molecular acceptors were used with FTAZ? To answer this question, we explored the impact of FTAZ M_n on OPVs with ITIC, a high-performance small molecule fused ring electron acceptor (FREA). By probing the photovoltaic characteristics of the resulting OPVs, we show that a similar FTAZ M_n insensitivity is also found in the FTAZ:ITIC system. This study highlights a single donor polymer which, when paired with archetypical fullerene, polymer, and FREA, results in systems that are largely insensitive to donor M_n. Our results may have implications in polymer batch-to-batch reproducibility, in particular, relaxing the need for tight M_n control during synthesis.

---

[1] Reproduced with permission from Samson, S., Rech, J., Perdigón-Toro, L., Peng, Z., Shoaee, S., Ade, H., Neher, D., Stolterfoht, M., & You, W. (2020). Organic Solar Cells with Large Insensitivity to Donor Polymer Molar Mass across All Acceptor Classes. *ACS Applied Polymer Materials*, *2*(11), 5300–5308.

2.2. Introduction

The molecular weight of polymers is perhaps the most important property of a given polymer, which separates polymers from small molecules. Typically, a high molecular weight is required to impart polymers with desirable physical properties, such as thermal stability and mechanical strength.[103,104] Conjugated polymers for bulk heterojunction (BHJ) solar cells are no exception. It has long been recognized that the molecular weight (e.g., number average molar mass, M_n) of conjugated polymers in BHJ blends has a strong influence in the device performance of such solar cells.[105–108] The M_n of donor polymers affects both the donor properties (e.g., mobility,[109] absorbance,[110] and glass transition tempearture[111]) and BHJ morphology[112] (e.g., domain size and composition,[109,113–115] structure,[116] and surface texture[117,118]). Moreover, the nature and severity of the effects of M_n of a given donor polymer on the performance of BHJ devices can vary from one system to the other when the nature of paring acceptor (as required by BHJ) is changed from fullerene derivatives, to non-fullerene based acceptors (including fused ring electron acceptors (FREAs), other small molecular acceptors, and polymer acceptors).[119,120]

These studies, regardless of the acceptor type, often found that there is some intermediate M_n range for the donor polymer which affords optimal photovoltaic properties, with performance falling off as a consequence of suboptimal morphology.[107,109,114,121–124] In addition, this optimal M_n range is dependent not only on the chemical nature of the donor polymer, but also on the acceptor that is paired with the specific donor in a BHJ blend. For example, consider BHJ organic photovoltaics (OPVs) utilizing the prototypical donor polymer, poly(3-hexylthiophene) (i.e., P3HT). When $PC_{61}BM$ (a fullerene derivative) was used, the maximum power conversion efficiency (PCE) of such BHJ devices was found at a M_n of ~30 kg/mol for P3HT.[107,121–123] In cases where a FREA acceptor was used, the trend between the M_n of P3HT and PCE can be similar, as with O-IDTBR, or very different, as with EH-IDTBR.[119] Furthermore, despite P3HT's ubiquity, there is no reported study on the effects of the M_n of P3HT on the BHJ system where P3HT was paired with a polymer acceptor, though such system had been reported as early as 2007.[125] In fact, to our knowledge, no studies have been done comparing the effects of M_n of the same donor polymer on BHJ solar cells across the three different types of acceptors from fullerene derivatives, to FREAs, to polymer acceptors. Such studies would disclose the differences and similarities of the impact of donor M_n across the three acceptor classes, and provide further insights on the fundamental reason why such differences and similarities would occur.

We chose PBnDT-FTAZ (i.e., FTAZ going forward) as the donor polymer for this study, since we have done extensive works with this particular polymer since its inception in 2011.[126] With collaborators, we had investigated the influence of M_n (FTAZ) on the performance of BHJ OPVs when $PC_{61}BM$ was used as the acceptor, and more recently, with N2200 as the polymer acceptor.[110,113] Thus, to complement the previous work, we set our goal to investigate the impact of M_n (FTAZ) with the remaining acceptor type – FREAs. With this study, we aim to complete our overarching goal of studying the impact of the M_n of a single donor across all three acceptor classes. Specifically, we chose the archetypal FREA, ITIC, in this study. We have measured photovoltaic and morphological properties of FTAZ:ITIC based BHJ OPVs utilizing FTAZ of M_n 10, 30, 40, 60, 100, and 120 kg/mol (hereafter referred to as 10K, 30K, 40K, 60K, 100K, and 120K FTAZ). We found an increase in PCE between 10 and 30 kg/mol (M_n of FTAZ) was accompanied by a shift in morphology of the FTAZ:ITIC blends. However, beyond 30 kg/mol, the PCE and morphology of the FTAZ:ITIC blends were rather insensitive to further increases in the M_n of FTAZ donor polymer, similar to what has been observed with FTAZ:N2200 and FTAZ:PC$_{61}$BM systems.

2.3. Results and Discussion

2.3.1. Polymer Synthesis

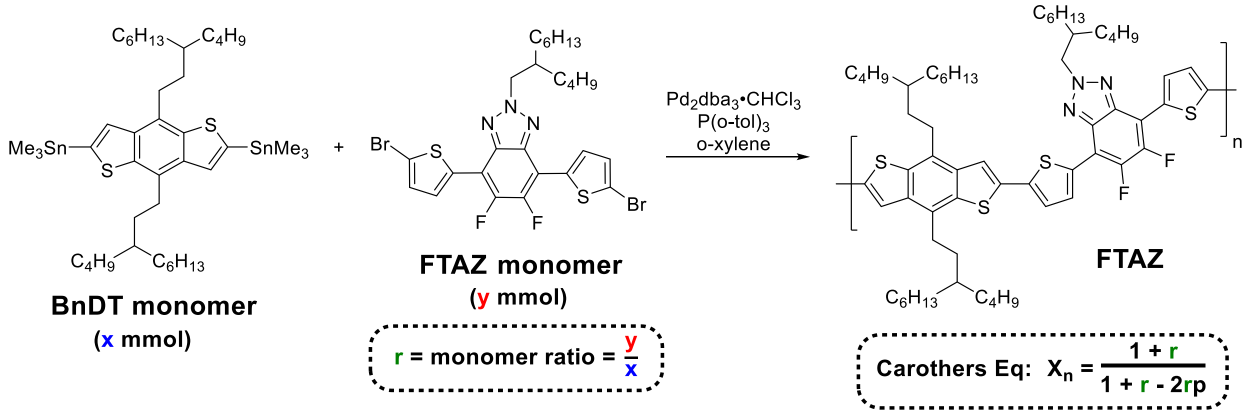

Scheme 2.1. The polymerization reaction (Stille polycondensation) between the BnDT moiety and FTAZ moiety to form the donor FTAZ polymer. The molar mass is controlled via the Carothers equation, which depends on the ratios of the two monomers (r) and the extent of reaction (p), with the latter assumed to be near unity (p=0.993) in our case.

The polymerization of FTAZ (**Scheme 2.1**), along with other donor-acceptor copolymers, is a common step-growth polymerization which can be described by the Carothers equation. In order for the Carothers equation to effectively describe the polymerization, and thus predict the molar mass, both the monomers and palladium catalyst must have very high purity and are recrystallized multiple times prior to use, as we described in detail in our earlier work.[113] As there are two monomers, the Carothers equation can control the molar mass by changing the monomer ratio (r; $0 < r \leq 1$); the extent of the reaction (p) is assumed to be near completion ($p = 0.993$) based on our previous experiences. Pleasingly, the measured M_n from high temperature gel permeation chromatography (HT-GPC) is close to the theoretical molar mass (**Table 2.1**). This observation not only verifies the validity and success of using the Carothers equation in our case, more importantly, the obtained series of FTAZ polymers with different yet controlled M_n

offer an excellent system for our study. Further polymerization details can be found in the supporting information. All FTAZ polymers in this molar mass range are soluble in common processing solvents of chloroform, chlorobenzene, and toluene (with the assistance of heat).

Table 2.1. Measured FTAZ number-average molar mass and dispersity.

FTAZ	M_n (kg/mol)	$Đ$
10K	7.5	2.02
30K	28.5	1.82
40K	40.9	1.96
60K	60.1	1.89
100K	105.2	1.94
120K	116.9	1.91

2.3.2. Device Performance

In order to determine the effect of donor M_n on the efficiency of our model polymer:FREA system, FTAZ:ITIC (1:1 w/w) BHJ devices were fabricated with the inverted architecture of indium tin oxide (ITO)/ZnO/FTAZ:ITIC/MoO_3/Al and an active layer thickness of ~ 90 nm. The resulting photovoltaic characteristics under one-sun conditions are visualized and tabulated in **Figure 2.1** and **Table 2.2**, respectively. Overall, the PCE, short-circuit current density (J_{SC}), open-circuit voltage (V_{OC}), and fill factor (*FF*) of devices are *insensitive* to changes in the M_n of FTAZ between ~30 – 100 kg/mol (**Scheme 2.1**, **Table 2.2**). However, at very low M_n, PCE, J_{SC}, and (to some extent) *FF* increase between 10 kg/mol and 30 kg/mol; in contrast, V_{OC} decreases in this range. At very high M_n (e.g., 120 kg/mol), slight decreases in PCE, V_{OC}, and *FF* are observed. To understand the origin of the performance difference, we further investigated the device results of these blends.

To begin with, J_{SC} (**Figure 2.1c**) increases more than 30% between 10K and 30K FTAZ then plateaus, with representative *J-V* characteristic curves (**Figure 2.1a**) largely overlapping beyond that point. In fact, the rather dramatic increase of J_{SC} from 10K to 30K is the primary cause for the noticeably increased PCE from 10K to 30K. It is worth noting that this trend is also observed in FTAZ:$PC_{61}BM$[113] and FTAZ:N2200[110] systems. Absorption trends of the blend films can be found in **Figure S2.1**, where all systems show similar and high attenuation coefficients. Previous measurements of neat FTAZ films reveal slight increases in attenuation coefficient with increasing M_n; however, these differences are not enough to account for the drastic change in J_{SC} beyond 30 kg/mol.[110] Furthermore, external quantum efficiency (EQE) (**Figure 2.1b**) measurements show similar response profiles for all M_n; however, the maximum response for the 10K polymer based BHJ device is only ~ 50% as opposed to ~ 70% for higher M_n polymers, which is consistent with the observed J_{SC} trend with the M_n.

Next, the *FF* (**Figure 2.1e**) also increases over the probed M_n range. Again, an increase is seen between 10K and 30K. Minor increases in *FF* are seen thereafter, with a slight decrease at very high M_n. We note that this increase in *FF* between 10K and 30K, also seen in previous studies on FTAZ,[110,113] cannot be strongly attributed to differences in mobility with M_n, because resistance dependent photovoltage (RPV)[127] (**Figure S2.2**) shows that mobility is only modestly affected by M_n (1.9×10^{-4} $cm^2/V{\cdot}s$ for 10K vs. 2.8×10^{-4} $cm^2/V{\cdot}s$ for 100K). This is consistent with previous studies.[110,113] Furthermore, the entanglement M_n as determined through elastic modulus measurements lies slightly below 30 kg/mol.[110] Though entanglement can hinder polymer crystallization,[122] it also increases the incidence of tie chains between crystalline domains.[105] These connections ensure charge transport between crystalline domains,[128] in line with our observed trends in mobility in this and in previous studies.[113] However, the increase in mobility between low and high M_n FTAZ alone is not enough to explain such a marked increase in J_{SC} and FF after 10K.

Unlike J_{SC} and *FF*, V_{OC} (**Figure 2.1d**) appears to decrease with increasing M_n, with the most dramatic changes seen at low M_n. At intermediate M_n, V_{OC} plateaus, followed by a slight drop at very high M_n. V_{OC} is primarily dependent on the energy offset between the donor's highest-occupied molecular orbital ($\mathrm{HOMO_D}$) and the acceptor's lowest unoccupied molecular orbital ($\mathrm{LUMO_A}$), but it is also affected by recombination dynamics.[78,129] The bandgap of FTAZ is not affected by M_n as previously demonstrated by Li et al.[113] and confirmed here with cyclic voltammetry (CV) measurements (**Figure S2.3a**). Moreover, the bandgap of the BHJ blend obtained by $\mathrm{EQE_{PV}}$ differentiation (dEQE/dE) does not apparently depend on the M_n of FTAZ (**Figure S2.3b**). Ultimately, PCE noticeably increases between 10 kg/mol and 30 kg/mol, plateaus between 30 kg/mol and 100 kg/mol, then decreases slightly at 120 kg/mol, with a champion performance of 11%. Though the trend of PCE with M_n largely tracks the trend of J_SC with M_n, further investigation of the BHJ morphology and device physics is necessary in order to understand the origin of the J_{SC}, V_{OC}, FF, and PCE trends.

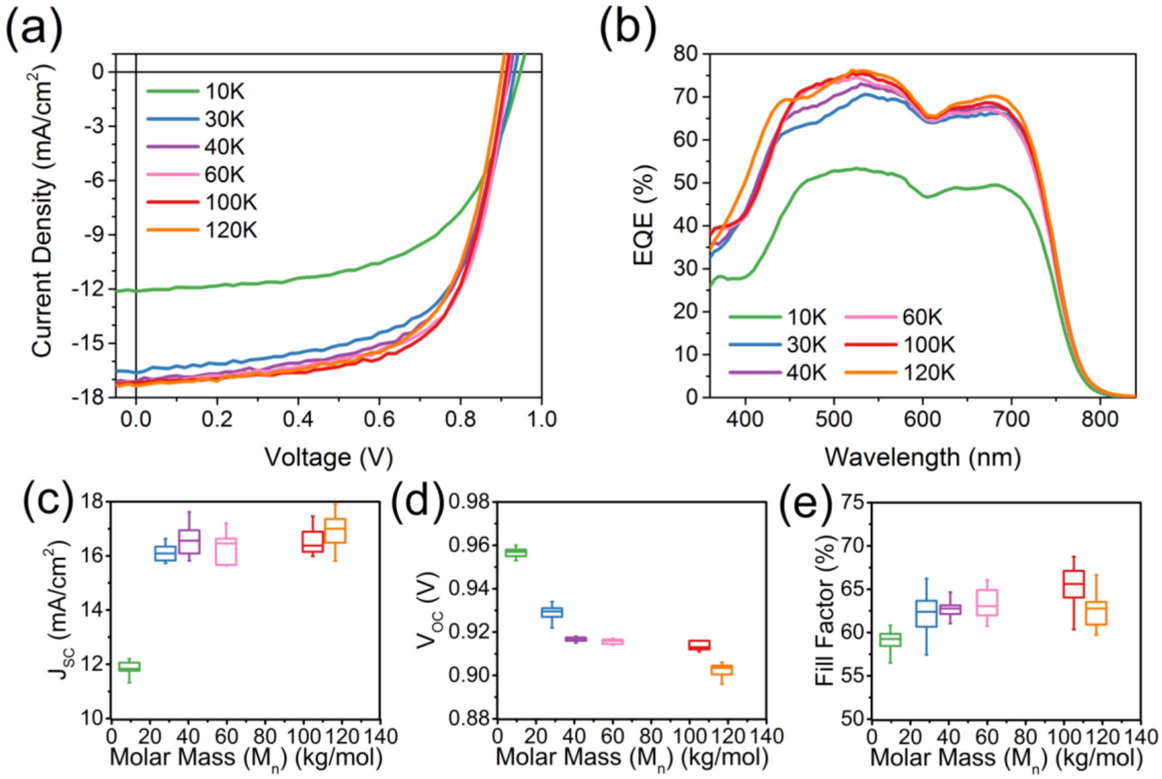

Figure 2.1. **(a)** *J-V* characteristics and **(b)** EQE of the blends of varying FTAZ M_n with ITIC. Box-and-whisker plots of OPV figures of merit, **(c)** J_{SC}, **(d)** V_{OC}, and **(e)** FF.

Table 2.2. Photovoltaic characteristics of FTAZ:ITIC solar cells.

FTAZ	J_{SC} (mA/cm^2)	V_{OC} (V)	FF (%)	PCE (%)	PCE$_{best}$ (%)	$J_{SC,calc}$ (mA/cm^2)
10K	11.88 ± 0.42	0.956 ± 0.003	58.3 ± 3.4	6.63 ± 0.52	**7.4**	11.23
30K	16.10 ± 0.28	0.929 ± 0.003	62.1 ± 2.5	9.29 ± 0.45	**9.9**	15.09
40K	16.53 ± 0.51	0.916 ± 0.002	62.7 ± 1.0	9.50 ± 0.37	**10.3**	15.49
60K	16.30 ± 0.58	0.916 ± 0.001	63.3 ± 1.8	9.46 ± 0.55	**10.2**	15.48
100K	16.57 ± 0.49	0.914 ± 0.002	65.4 ± 2.1	9.90 ± 0.48	**11.0**	15.79
120K	16.90 ± 0.57	0.903 ± 0.003	62.7 ± 1.9	9.56 ± 0.51	**10.5**	16.12

2.3.3. Morphology

As the OPV characteristics are heavily dependent on morphology,[130] we explored the bulk molecular packing and texture of the active layer using synchrotron radiation-based grazing incidence wide angle X-ray scattering (GIWAXS) and resonant soft X-ray scattering (RSoXS).

GIWAXS was used to extract molecular-scale morphological information both in and out of the sample plane,[85,131] and the collected scattering provides information such as π-π stacking distance, lamellar spacing, film texture, and crystallinity.[131] 2D GIWAXS patterns of neat FTAZ films (**Figure S2.4**) revealed relatively low crystallinity with a lamellar stacking peak at $q = 0.3$ Å^{-1} in-plane (corresponding to a spacing distance of 20.9 Å) and π-π stacking peaks at $q \sim 1.7$ Å^{-1} out-of-plane (corresponding to a spacing distance of 3.7 Å). Though morphology was largely similar between the higher M_n FTAZ, the neat 10K FTAZ film is markedly less ordered, indicative of less preferential packing. Moreover, the in-plane stacking peaks are stronger for higher M_ns, suggesting an enhanced preference for the face-on orientation. This is similar to what has been previously observed in our past studies with FTAZ.[110,113] 2D GIWAXS patterns of blend films (**Figure 2.2**) demonstrated similar peaks and spacings as the neat films, with a preferential face-on orientation for FTAZ having M_n over 10 kg/mol. Notably, the 10K FTAZ blend showed little to no preference in lamellar stacking orientation.

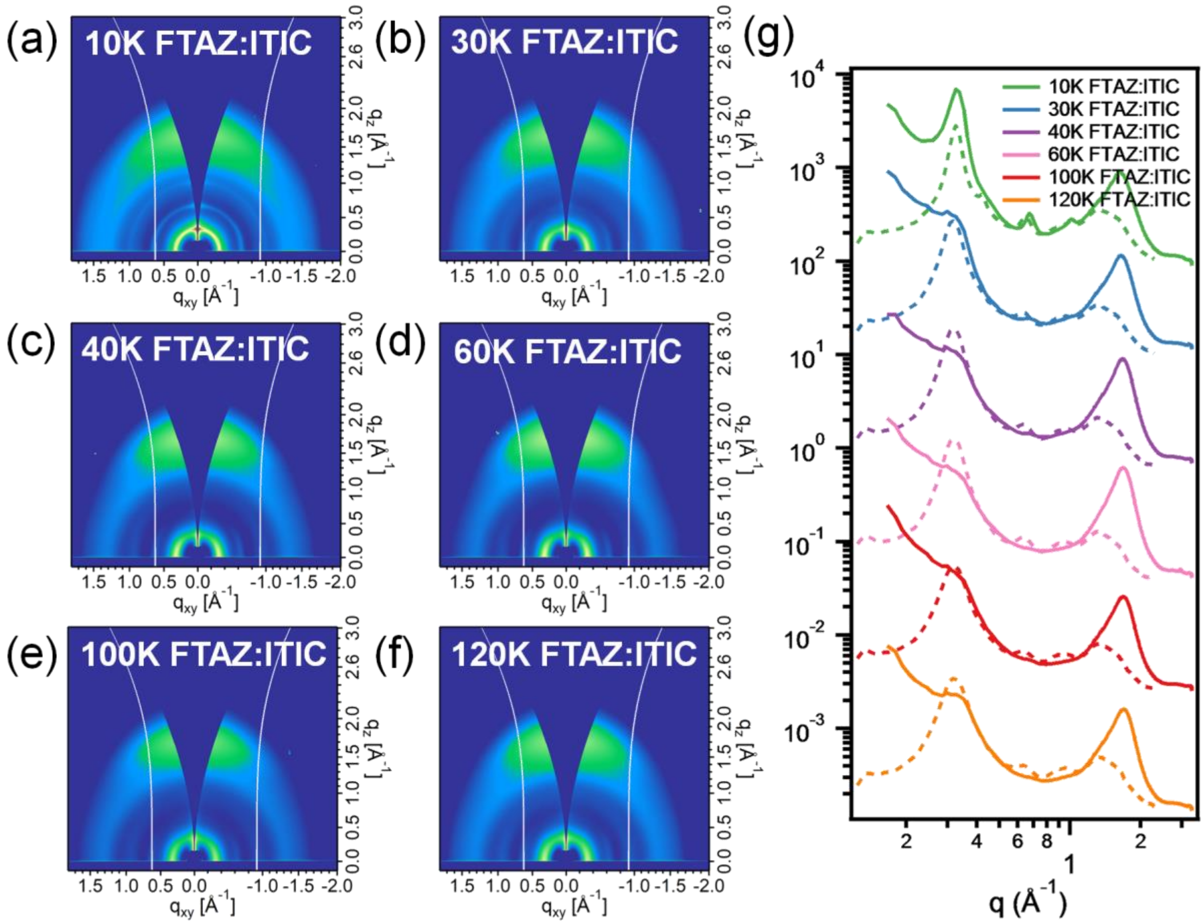

Figure 2.2. (a) - (f) 2D GIWAXS patterns and **(g)** line-cuts out-of-plane (solid) and in-plane (dashed) for FTAZ:ITIC blend films with donor M_n of **(a)** 10, **(b)** 30, **(c)** 40, **(d)** 60, **(e)** 100, and **(f)** 120 kg/mol.

As GIWAXS primarily probes molecular-scale contrast variations (particularly, molecular packing), RSoXS was used to probe mesoscale morphological information in the sample plane regarding overall domain characteristics.[82] Here, we extract the long period, or center-to-center domain spacing, and the relative composition variations of the active layer (formerly called domain purity). By RSoXS, each different M_n FTAZ:ITIC blend demonstrated a single size distribution (**Figure 2.3a**). In addition, long period and relative composition variations (**Figure 2.3b**) decreased with increasing M_n. The 10K polymer blend had the largest domain spacing at ~ 60 nm, while larger M_n polymers had domain spacings around ~ 20 nm. As exciton diffusion length is ~ 10 nm,[26] the large spacing in the 10K FTAZ batch hinders charge separation. Furthermore, the relative composition variations show that the 10K blend has the purest domains. Because the 10K blend has both the largest and purest domains, this can result in reduced exciton splitting and will result in a large J_{SC} loss. In addition, domain purity is typically reflected in *FF*,[132] where excessively impure domains can lead to increased bimolecular recombination[70,133–135] and excessively pure domains can lead to isolated charge traps.[135] On the other hand, more mixed domains provide increased interfacial area and percolation pathways beneficial for charge separation and transport, affecting both J_{SC} and *FF*. The J_{SC} and *FF* of the 10K polymer is significantly lower than those of higher M_n polymers despite the high relative domain purity of 10K FTAZ blends. This suggests that the 10K blend's domains may be excessively pure, potentially limiting exciton separation into free carriers. The ultimate effect of the 10K blend's overly-large and pure domains is a reduced exciton dissociation efficiency, lowering J_{SC}. On the other hand, domain purity and spacing were remarkably similar for the intermediate M_n polymers, though domain purity decreased slightly for the largest M_n polymers. This may have contributed to the slight decrease in *FF* seen at very high M_n. The relatively strong phase segregation in very low M_n FTAZ blends was also observed in the FTAZ:$PC_{61}BM$ system but not in the FTAZ:N2200 system. We speculate that low M_n, particularly when the M_n below the entanglement M_n, could facilitate aggregation of the small molecular acceptors. In contrast, the use of a polymer acceptor may hinder the aggregation of the donor due to the chain entanglements of the acceptor. Despite differences at very low donor M_n, morphology for all three systems was reasonably invariant for a large range of moderate FTAZ M_n.

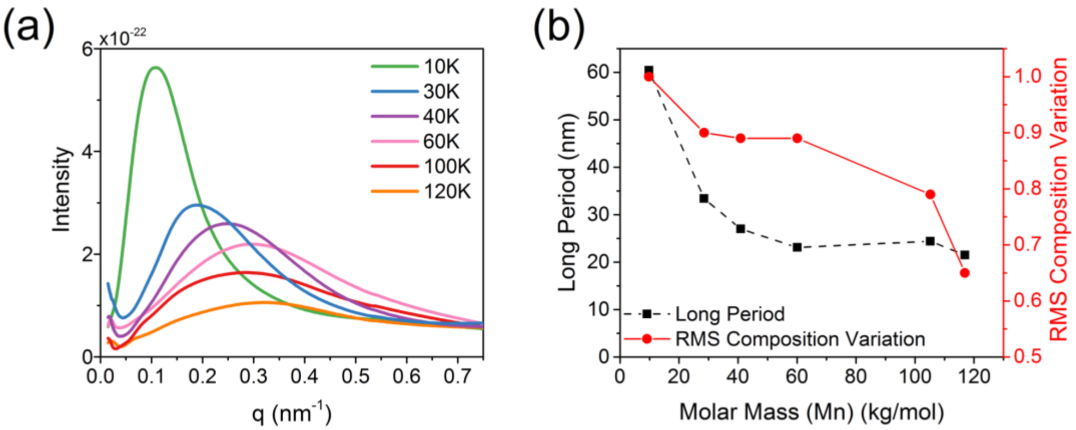

Figure 2.3. (a) Thickness-normalized RSoXS profiles extracted at 283.4 eV and **(b)** long period (domain spacing) and RMS composition variation (domain purity) for FTAZ:ITIC blends with varying donor M_n.

In summary, morphological studies reveal that the excessively large and pure domains present in 10K FTAZ blend devices contributed to the markedly low J_{SC} at low M_n. As M_n is increased to intermediate values between 30 kg/mol and 100 kg/mol, 2D GIWAXS patterns, long period and relative composition variations become relatively constant. While morphological studies have provided insight into our observed J_{SC} and FF trends, the V_{OC} remains unexplained. A hint from the morphology measurements lies in the relative composition variations, as the domain purity affects recombination and thus V_{OC}. To clarify the V_{OC} trend, we turn to device physics measurements.

2.3.4. Device Physics

Though analysis of GIWAXS and RSoXS data elucidated trends in J_{SC} and *FF*, the origin of the observed decrease of V_{OC} from low to very high M_n remains unclear. In order to further investigate this V_{OC} loss, we probed recombination mechanisms of the devices, since the recombination losses typically account for the main loss of V_{OC}.[136]

Recombination can be probed by measuring the dependence of *J*-*V* characteristics on light intensity. The J_{SC} may have a power law scaling with light intensity (I), $J_{SC} \propto I^{\alpha}$. For relatively low light intensities,[137,138] such as the one sun condition, α is typically between 0.9 and 1.[139] Ideally, $\alpha = 1$, signifying that carriers are swept out before recombination at short-circuit,[140] although this does not allow to exclude first-order recombination losses.[141] Nevertheless, $\alpha \sim 1$ means that recombination losses scaling with the second-order of the light intensity are absent.[137,138]

On the other hand, V_{oc} can be described by the following equation:

$$V_{OC} = \frac{nkT}{q} \ln\left(\frac{J_{SC}}{J_0} + 1\right) \tag{2.1}$$

where kT is the thermal energy, q is the electric charge and J_0 is the dark saturation current density. Here, the ideality factor n accounts for the deviation from the ideal bimolecular recombination. Experimentally,[140] the slope of V_{OC} vs. $\ln(I)$ can be used to determine n, where I is the light intensity. A slope of unity (i.e., $n = 1$) typically indicates that the bimolecular recombination is dominant. Deviations from $n = 1$ indicate the presence of a competing recombination processes of different order. For example, $n \leq 1$ suggests the presence of surface recombination and that the V_{OC} saturates to the built-in voltage, $1 \leq n \leq 2$ implies a combination of bimolecular and trap-assisted recombination, and $n = 2$ indicates that trap-assisted recombination is dominant.[142,143]

In our system, from the log-log plot of J_{SC} vs. I (**Figure 2.4a**) and semi-log plot of V_{OC} vs. I (**Figure 2.4b**), α and n were found to be ~ 1 for all values of M_n, except for a slight increase in n for 120K FTAZ. This increase in n may have contributed to the slight decrease in FF observed for very high M_n and is also in line with the observed decrease in domain purity. Overall, the light intensity dependence of J_{SC} and V_{OC} indicates that bimolecular recombination is the dominant mechanism for all M_n blends, but it is relatively weak at short-circuit conditions.

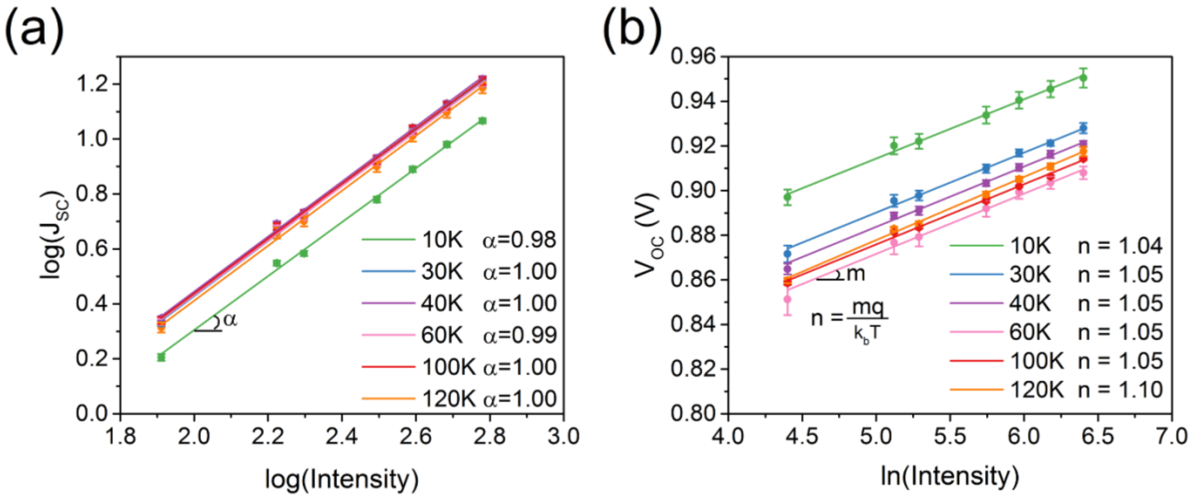

Figure 2.4. Light intensity measurements for investigating recombination in FTAZ:ITIC blend films. **(a)** Log-log fitting of J_{SC} vs light intensity (W/m^2) to probe for deviations from weak bimolecular recombination. **(b)** Semi-log fitting of V_{OC} vs. light intensity (W/m^2) to determine recombination order.

To further classify these V_{OC} losses (ΔV_{OC}) from recombination, we can divide ΔV_{OC} into unavoidable radiative ($\Delta V_{OC,rad}$) and avoidable non-radiative ($\Delta V_{OC,nr}$) losses. For this study, the ΔV_{OC}s of 10K and 100K FTAZ (i.e., the M_ns resulting in the lowest and highest PCEs, respectively) were explored. $\Delta V_{OC,nr}$ can be determined experimentally through EQE_{EL} (**Figure 2.5**) using

$$\Delta V_{OC,nr} = -\frac{kT}{q} ln(EQE_{EL}). \tag{2.2}$$

EQE_{EL} is taken at an injected current such that $J_{inj}(V_{OC}) = J_{SC}$ as $\Delta V_{OC,nr}$ should be evaluated under conditions similar to open-circuit under illumination.[144] Furthermore, the V_{OC} can be calculated by first determining its value in the limit of only radiative recombination ($V_{OC,rad}$),

$$V_{OC,rad} = \frac{kT}{q} ln\left(\frac{J_{SC}}{J_{0,rad}} + 1\right), \tag{2.3}$$

then subtracting the calculated $\Delta V_{OC,nr}$,

$$V_{OC} = V_{OC,rad} - \Delta V_{OC,nr} = \frac{E_{CT}}{q} + \frac{kT}{q}\ln\left(\frac{J_{SC}h^3c^2}{fq2\pi(E_{CT} - \lambda)}\right) + \frac{kT}{q}\ln(EQE), \qquad (2.4)$$

where the first two terms in the rightmost expression comprise $V_{OC,rad}$.[145] $J_{0,rad}$ is the radiative current density in the dark due to the blackbody radiation and can be determined by extending the EQE_{PV} using the EL spectra (**Figure S2.5**).[146,147] Differences in the non-radiative losses account for the majority of the V_{OC} difference between the 10K and 100K FTAZ blends. **Table 2.3** shows that the 10K FTAZ blend has a lower $J_{0,rad}$ and higher EQE_{EL} than the 100K FTAZ blend, meaning that relatively high V_{OC} of the 10K FTAZ blend can thus be attributed to the reduced non-radiative losses using **Equation (2.4)**. Morphologically, the difference in V_{OC} losses may potentially stem from the large and relatively pure domains of the 10K FTAZ blends, where the decreased D:A interfacial area results in decreased radiative[148] and non-radiative[149] recombination. Voltage losses can also be related to the charge transfer state energy (E_{CT}) through **Equation (2.4)**.[150] However, E_{CT} is difficult to determine due to overlap of the EQE_{PV} with what we ascribe as the singlet emission from the FREA, ITIC at ~1.6 eV[151] (**Figure S2.5**). The appearance of a contribution from the singlet excitons in the electroluminescence spectra of both blends points to a significant hybridization between charge transfer states and the first excited singlet, which has been shown for a number of organic blends.[152] Hybridization results in increased luminescence of the CT state and thereby a decrease in the non-radiative recombination losses.[152] In the case of the 10K and 100K FTAZ blends, the evidence of a stronger singlet "shoulder" in the EL (**Figure 2.5**) suggests a larger coupling to singlet excitons in the 10K FTAZ device, which according to the work of Eisner *et al.*,[152] explains the higher EQE_{EL} values obtained. As for the $J_{0,rad}$, **Figure S2.5** still suggests that E_{CT} could be at slightly higher energies in the 10K FTAZ blend, which could explain the lower $J_{0,rad}$ value and hence the slightly smaller radiative recombination losses.

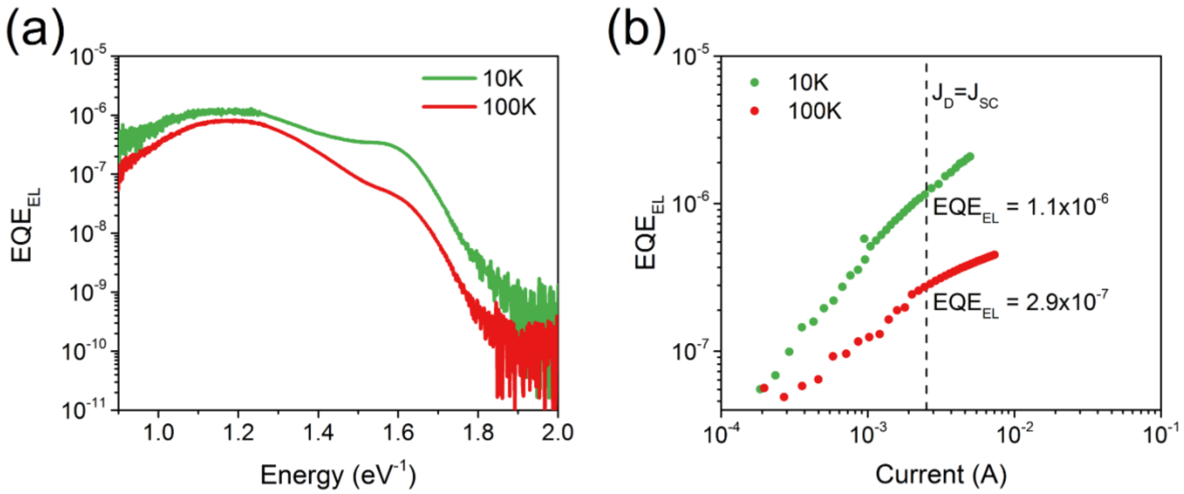

Figure 2.5. Electroluminescence spectra of 10K and 100K FTAZ polymer blends **(a)** against photon energy and **(b)** against injection current. The EQE_{EL} for energy loss calculations is taken at an injected current equivalent to the J_{SC} relevant to open-circuit conditions. The graph shows that the EQE_{EL} is approximately ~3.8 smaller in the 100K FTAZ organic solar cell blend.

Table 2.3. Parameters used for the calculation of energy losses based on measured EQE_{EL}.

FTAZ	J_{SC} (A/m²)	$J_{0,rad}$ (A/m²)	EQE_{EL}	$V_{OC,rad}$ (V)	$\Delta V_{OC,nr}$ (V)	V_{OC} (V)	
						meas.	**calc.**
10K	140	3.3×10^{-20}	1.1×10^{-6}	1.29	0.36	0.92	0.93
100K	170	1.5×10^{-19}	2.9×10^{-7}	1.26	0.39	0.90	0.87

2.4. Conclusions

We have discovered that the photovoltaic characteristics of FTAZ:ITIC blends are insensitive to M_n within the probed range beyond 30 kg/mol with variations < 10%. This trend is not only unusual over such a large M_n range, but it also consistent with trends seen in FTAZ:PC_{61}BM and FTAZ:N2200 systems. Thus, this study utilizing FREA ITIC as the acceptor completes our overarching study on the impact of donor FTAZ M_n with three representative acceptors (**Figure 2.6**). Our results from the FTAZ:ITIC system show that increases in *FF* and J_{SC} from 10K to 30K are primarily attributed to improved morphology. This morphology is consistent for blend films utilizing 30K or greater FTAZ. A modest increase in mobility is observed despite reduced phase purity, while a smaller long period and more oriented morphology allows for more efficient exciton dissociation and charge transport. Low M_n blends demonstrate higher V_{OC}, which plateaus at intermediate M_n then continues to decrease. Given the identical band gaps of the neat FTAZ polymers, the increasing energy loss from 10K to 100K is ascribed to lower radiative and non-radiative energy losses in the case of the lower M_n. In summary, together with our earlier works,[110,113] this study demonstrates a single donor polymer which, when blended with prototypical fullerene ($PC_{61}BM$), polymer (N2200), or FREA (ITIC) acceptors, demonstrates reduced sensitivity of photovoltaic and morphological characteristics over a remarkably wide range of M_n. Though the effects of donor FTAZ M_n observed in this study may not be universal across all possible acceptors, these results suggest it is possible to achieve efficient and reproducible OPVs with varying acceptor types without the need for stringent M_n control during synthesis, as long as the donor polymer has a sufficiently high M_n. However, the origin of this broad M_n insensitivity is not yet known. The results of the overarching study can serve as a stepping stone for future work to correlate chemical structure to the observed behavior.

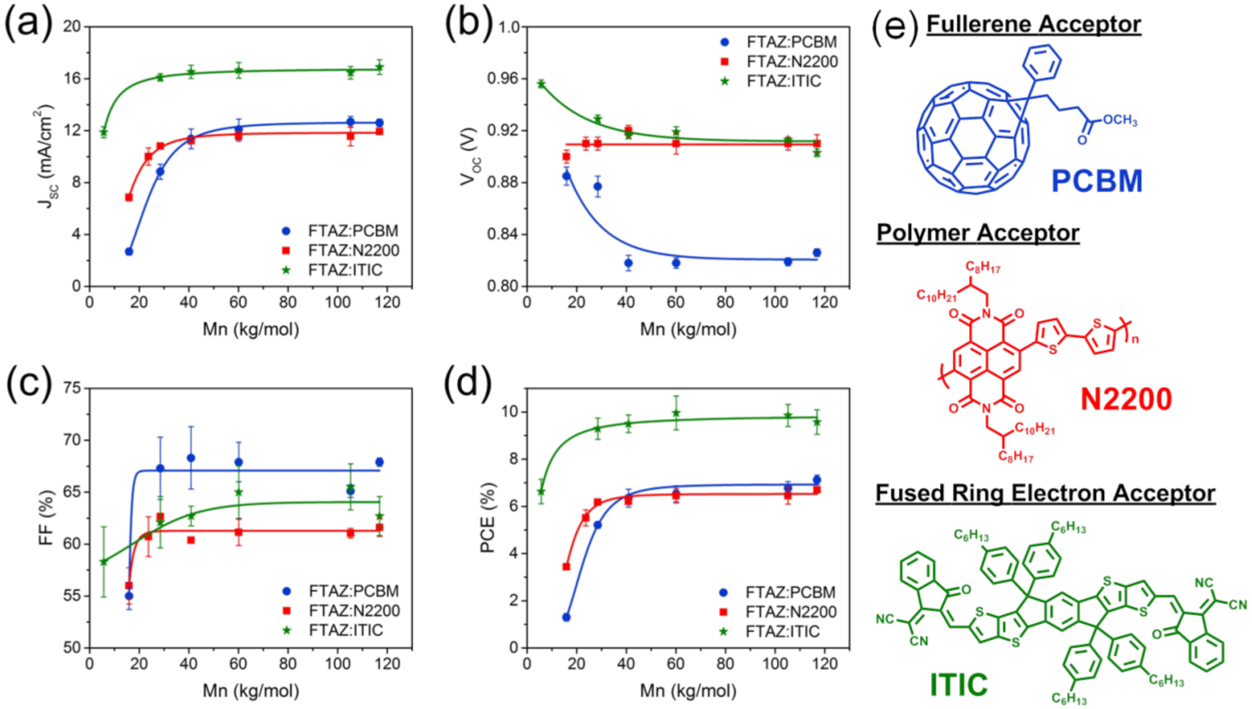

Figure 2.6. Trends in photovoltaic figures of merit with increasing M_n for FTAZ:$PC6_{1B}M$, FTAZ:N2200, and FTAZ:ITIC systems: **(a)** J_{SC}, **(b)** V_{OC}, **(c)** FF, and **(d)** PCE. The chemical structure for each electron acceptor is shown in **(e)**. The exact same polymer batches of FTAZ were used for all three systems from 30K – 120K. The solid lines are guides to the eyes.

CHAPTER 3: REDUCING COST THROUGH PROCESSING ROBUSTNESS THE EFFECT AND ULTIMATE FATE OF SOLID-STATE ADDITIVES IN P3HT:PCBM

3.1. Synopsis

While the impurity tolerance of OPVs in unknown and likely material- and architecture-dependent, it is widely believed that impurities are detrimental to organic photovoltaics (OPVs). These impurities may cause suboptimal morphologies, trap states, and decreased morphological and/or chemical stability. Because of this, great care is taken in material synthesis, purification, and processing, resulting in overall increased costs. Indeed, the overall cost of manufacturing OPVs is largely that of the active layer material.[52,153,154] Using P3HT:PCBM, the archetypal low-cost donor:acceptor system, we introduced acidic, basic, neutral, and ionic small molecule solid additives with potentially reactive moieties. While it was expected that power conversion efficiency (PCE) would fall with increasing additive content, this was not broadly the case. Indeed, some of these additives were well-tolerated or even beneficial. Furthermore, analysis of processed films revealed that the solid impurities were largely removed during device fabrication despite their relatively high boiling points and low vapor pressures. This suggests that OPV systems are not as sensitive as generally believed and that material purification and processing need not be as stringent and costly.

3.2. Introduction

Major progress in the field of organic photovoltaics (OPVs) began with the conception of the bulk heterojunction (BHJ), a morphology comprising bi-continuous, interpenetrating donor and acceptor domains. BHJ OPVs provided a solution for the antagonistic small diffusion length

(~ 10 nm) and large optical absorption length (~ 100 nm) encountered in OPV materials.[27–29] The BHJ morphology, however, is a double-edged sword. The photovoltaic (PV) properties of the OPV devices depend heavily on that morphology, which is not only sensitive to stressors such as light, heat, oxygen, and moisture, but is also often thermodynamically unstable.[64,65] Without modifying the OPV materials (active layer and interlayers, specifically), these kinetically-trapped morphologies must often be driven to a more favorable—but still kinetically trapped—state. This is commonly done by manipulating film formation using liquid and/or solid additives and/or adjusting as-cast morphologies via post-deposition processing such as thermal or solvent annealing. The use of additives is particularly popular due its speed and ease-of-use.[155,156] Furthermore, some allow the manipulation of morphology without requiring additional time or processing steps, avoiding unnecessary stressors such as heat.[155]

In particular, liquid-phase solvent additives have been widely employed to modulate BHJ morphology during film formation.[157–159] These are usually high-boiling point solvents with selective solubility, with non-conjugated molecules typically enhancing crystallinity and aromatic molecules typically increasing miscibility.[156] It should be noted that though solvent additives comprise ~ 0.1 - 1 vol% of the solution, they are added in amounts comparable to the active layer materials themselves. These liquid additives are usually assumed to be volatilized during the course of processing, which often involves mild heating and high vacuum conditions. However, this has been shown to not necessarily be the case, such as with higher-vapor pressure additives like 1,8-diiodooctane and octanedithiol, and is known to be detrimental to long-term OPV stability.[158,160,161] This leads to the need for additional processing steps (and thus cost) to ensure no solvent additive remains.

Solid-state additives often take the form of aromatic small molecules or polymers, potentially with some features to modulate intermolecular interactions, which may be volatilized or remain in the film in some amount.[156] In contrast to solvent additives, solid-state guest molecules may be used to enhance OPV stability (should they remain in the film)[160,162–164] and—assuming sufficiently low diffusion—may even enable thick-film OPVs.[163] Solid-state additives typically enhance crystallinity through π-π or other intermolecular interactions[163] or prevent over-crystallization by disrupting aggregation.[164] Furthermore, if a solid-state additive/impurity is not detrimental to morphology or morphological stability, there is no need for additional processing steps to ensure removal. Unfortunately, though solid-state additives could potentially be more versatile than their liquid counterparts, they are not nearly as well-studied. Furthermore, the ultimate fate of these additives is not often discussed so their impact on long-term stability is not well-known. Herein, we aim to evaluate the robustness of OPVs to high concentrations of solid impurities and to what extent these impurities remain in the film after device processing. Because it has been demonstrated that conjugated small molecules, such as hexylthiophene, can be used as solvent additives to enhance crystallinity, increase domain size, and reduce π-π spacing,[165] we utilize similar solid-state small molecules in this study. These small molecules are similar monomer units or other materials used in polymer or small molecules synthesis. Typically, potentially reactive functionalities are avoided due to concerns such as material degradation and charge trapping. However, because we want to assess tolerance, we purposely introduce active functionalities. To this end, we introduce acidic, basic, and ionic aromatic small molecules to the low-cost, archetypal system P3HT:$PC_{61}BM$, whose structures are shown in **Figure 3.1**. In addition, we varied processing solvent and interlayers (which have both been demonstrated to affect active layer morphology)[166–169] to further probe the effects of these impurities.

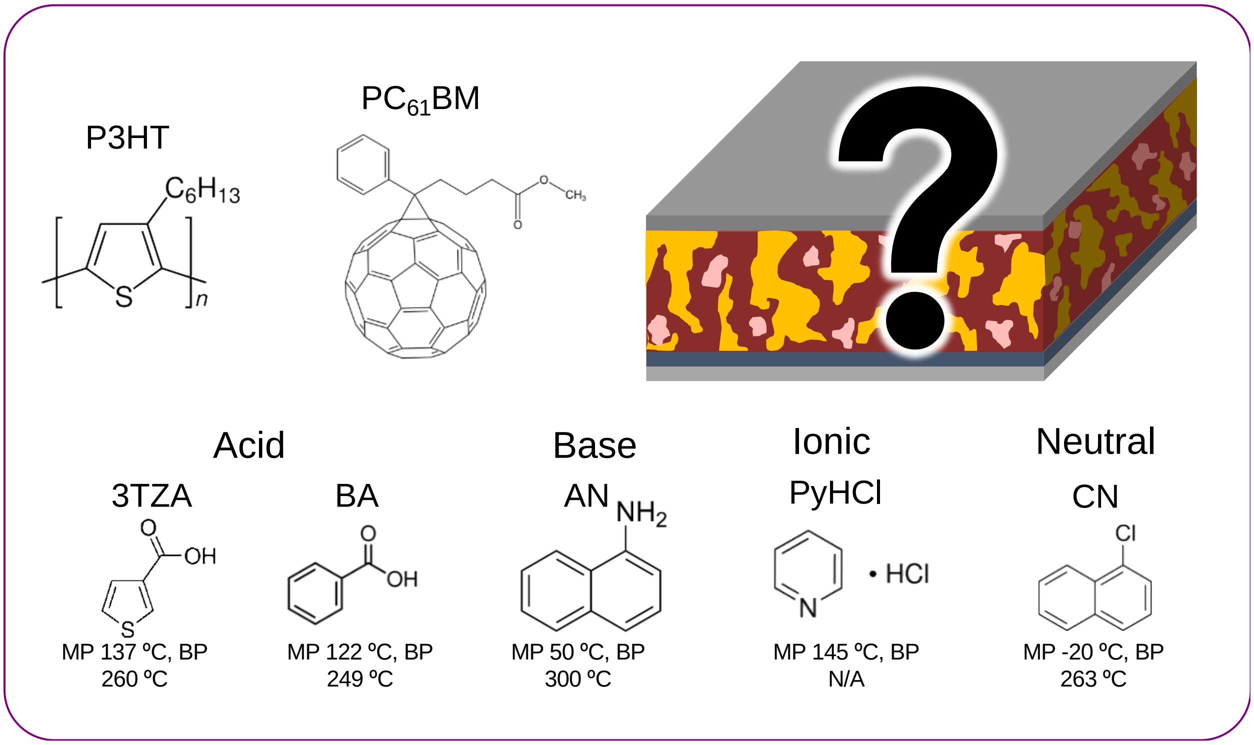

Figure 3.1. Active layer materials and solid additives discussed in this work.

3.3. Results and Discussion

3.3.1. Acidic Molecules

A small molecule, 3-thiophene carboxylic acid (3TZA), was used as a model acid. It is an aromatic solid somewhat similar in structure to P3HT monomer and is a starting material in some polythiophene syntheses. However, unlike P3HT or hexylthiophene, 3TZA contains a carboxylic acid group which may participate in intermolecular interactions such as hydrogen bonding (should it remain in the film) or even form covalent bonds with metal oxides. Furthermore, 3TZA has a melting temperature above processing temperature, boiling point exceeding 200 °C, and relatively low vapor pressure compared to aromatic solvent additives, such as 1-chloronapthalene (CN). 3TZA was incorporated into conventional P3HT:$PC_{61}BM$ (cast from chloroform) devices using poly(3,4-ethylenedioxythiophene) polystyrene sulfonate (PEDOT:PSS) as the hole-transporting layer (HTL). Remarkably, 3TZA was well-tolerated, losing < 20% PCE at a 1:4 P3HT:3TZA weight ratio (**Figure 3.2a**). What is even more surprising, however, is that 3TZA was beneficial to PV performance in inverted devices using zinc oxide (ZnO) as the electron-transporting layer (ETL) (**Figure 3.2b**). Improvements scaled with increasing 3TZA concentration and were primarily seen in J_{SC} and FF, with V_{OC} remaining largely unchanged. To ascertain the source of the improvements seen in the inverted devices, we first investigated potential effects of the 3TZA molecule itself, both in the bulk and at the buried interface.

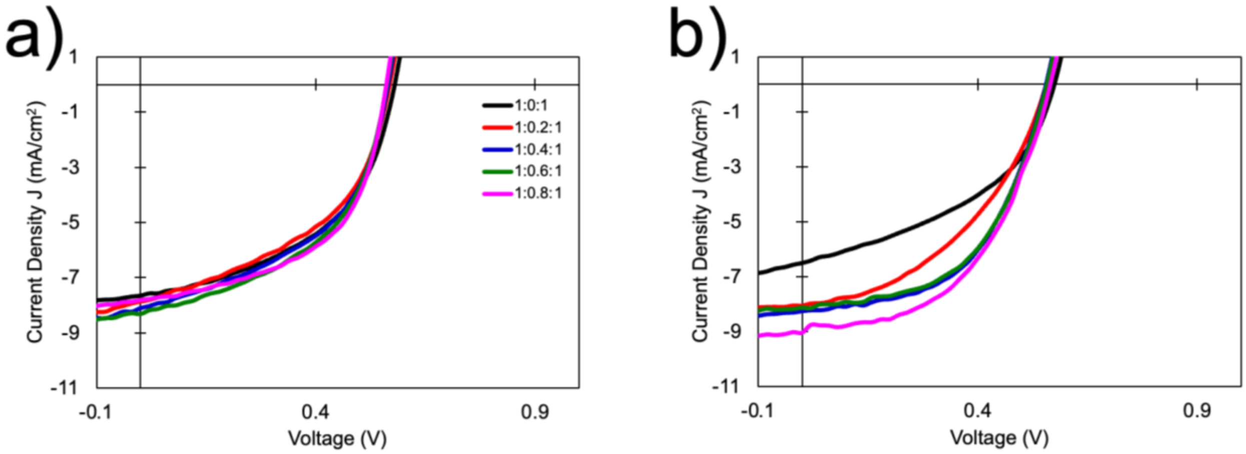

Figure 3.2. Current density vs. Voltage (J-V) curves of P3HT:3TZA:PCBM devices. **a)** J-V curves for conventional devices with the architecture ITO/PEDOT:PSS/P3HT:3TZA:PCBM/ Ca/Al. **b)** J-V curves for inverted devices with the architecture ITO/ZnO/P3HT:3TZA:PCBM/ MoOx/Al

To probe for the presence of 3TZA in the bulk film, we prepared 1:0.8:1 P3HT:3TZA:PCBM films, retaining some at each step major step of processing. NMR on the redissolved films revealed 90% of the 3TZA was lost during the thermal annealing step, with the remaining 10% leaving the bulk likely due to the high-vacuum conditions during electrode deposition (**Figure 3.3**). 3TZA's absence in the bulk suggests that it must remain at the interface, if at all. However, because the interfacial layer (PEDOT:PSS or ZnO) is buried in orthogonally soluble to the active layer materials, we constructed a model interface to observe the interaction with 3TZA and ZnO directly. To this end, deposited 3TZA solution directly onto ZnO, then washed the surface with chloroform to loosen any weakly-adsorbed molecules. Previous literature has shown that ZnO can not only seed active layer morphology on its own, but also can be used to host a “seed layer” or self-assembled monolayer (SAM) comprising small aromatic molecules bound via a carboxylic acid, phosphoric acid, thiol, or silane anchor.[170–172] X-ray photoelectron spectroscopy (XPS) on washed 3TZA films revealed the presence of sulfur, though the atomic S:Zn ratio had been greatly reduced (**Figure S3.1**). Furthermore, this film of 3TZA has minimal impact on ITO/ZnO work function (Φ) as shown by ultraviolet photoelectron spectroscopy (UPS) (**Figure S3.2a**). Though literature suggests carboxylic acid will bind chemically to ZnO,[169,170,172] it is unclear whether or not 3TZA is adsorbed or chemically bound based on its O 1s XPS spectra (**Figure S3.1**), as it is difficult to discern carboxylic acids from esters. Regardless, 3TZA appears to act as a passivation layer, helping prevent potential surface recombination sites and improving charge transport and extraction, thereby improving both J_{SC} and *FF* in line with our observations.[170]

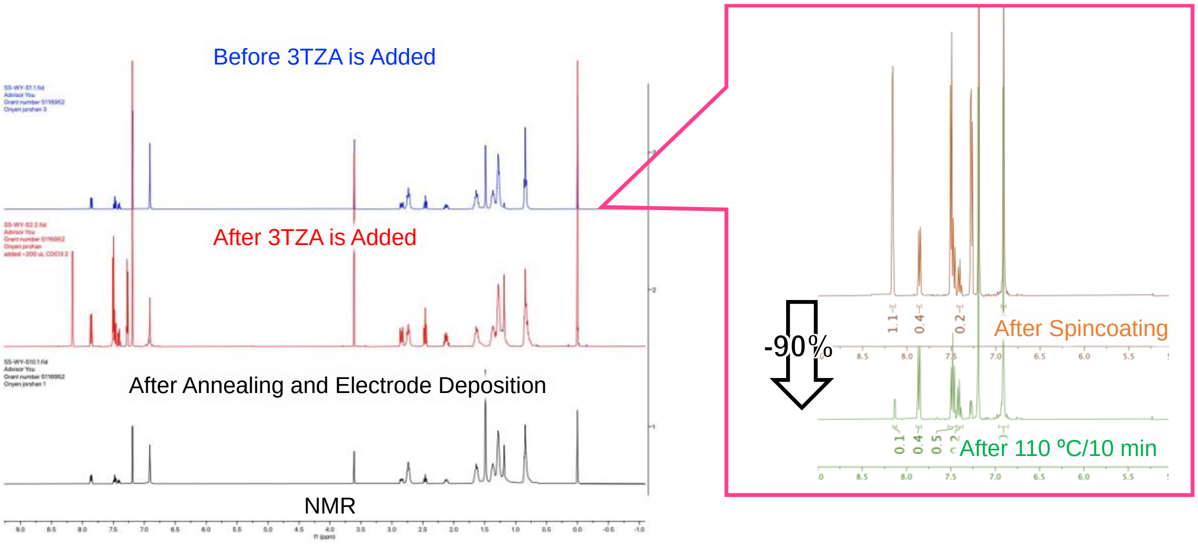

Figure 3.3. NMR Spectra of re-dissolved P3HT:3TZA:PCBM films cast onto glass with no HTL or ETL.

To probe the effect of a 3TZA passivation layer independently from 3TZA's potential morphological effects, a solution of 3TZA was cast onto ZnO directly or ZnO coated with a known SAM, 4-[(1,3-dioxoinden-2-ylidene)methyl] benzoic acid (referred to as IC-SAM going forward). If the J_{SC} and *FF* improvements are due primarily due to a passivation layer, then adding a thin film of 3TZA on top of IC-SAM should have little effect on PV FoM of binary P3HT:PCBM films, assuming IC-SAM coverage is complete. Indeed, as seen in **Figure 3.4a**, the introduction of 3TZA thin films results in enhanced *FF* and J_{SC}, though J_{SC} may be reduced at higher 3TZA concentrations. Furthermore, passivation of the ZnO surface (**Figure 3.4b**) in advance using IC-SAM results in a loss of the concentration-dependent behavior shown **Figure 3.4a**. These results suggest at least a portion of the improvements observed on inverted devices can be ascribed to the formation of a 3TZA passivation layer on the ZnO ETL.

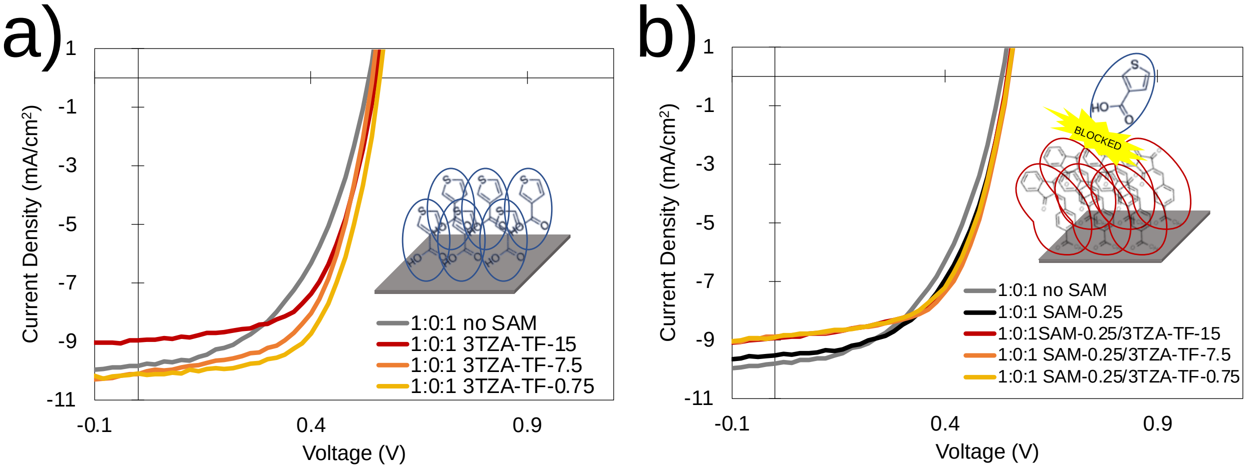

Figure 3.4. J-V curves of devices with architecture ITO/ZnO/x/3TZA/P3HT:PCBM/MoOx/Al, where x is **a)** absent, **b)** SAM1, or **c)** 15 mg/mL 3TZA. The 3TZA layer following layer x is spin cast at 15, 7.5, and 0.75 mg/mL.

Building upon this, we posited that if the ZnO has been passivated before active layer deposition, then changes in PV FoM in blend P3HT:3TZA:$PC_{61}BM$ films can be largely attributed to morphological changes. In devices where the blend is cast onto IC-SAM-treated ZnO, there is a small drop in PCE between 20 wt% and 80 wt% 3TZA devices resulting from a loss of J_{SC}, which is somewhat offset by improved FF (**Figure S3.3a**). Furthermore, the addition of 3TZA does not appear to be able to improve PV properties much beyond that of the initial IC-SAM treated substrate, regardless of the SAM quality (**Figure S3.3a, c**). These findings suggest that there are both beneficial ZnO passivation and detrimental morphological effects in play contributing to the net improvement of PCE in inverted devices, prompting us to investigate morphology using grazing incidence wide angle x-ray spectroscopy (GIWAXS) and resonant soft x-ray spectroscopy (RSoXS). Surprisingly, GIWAXS (**Figure 4.5**,

Table S3.1) reveals similar crystalline nanoscale morphologies on both ZnO and PEDOT:PSS. In both cases, the morphology is preferentially edge-on, with a π-π spacing of 3.85 nm, which is consistent with previous literature regarding P3HT:$PC_{61}BM$.[173] Furthermore, there is little change in long period (extracted from RSoXS), or center-to-center domain spacing, between P3HT:PCBM with and without 3TZA (

Table S3.1). While this disappointing, there are still other parameters which may be considered in future studies, such as domain purity and vertical phases separation.

Curiously, the effects of 3TZA also appear to depend on ZnO quality and the active layer thickness, allowing otherwise overly-thick devices on poorer-quality ZnO (or SAMs) to reach similar PCEs as their relatively pristine counterparts (**Figure S3.5**). Moreover, the addition of 3TZA to optimized devices on higher-quality ZnO—while beneficial in small amounts—more quickly becomes detrimental, with losses primarily in J_{SC} (**Figure S3.3c, Figure S3.6b**). It should also be noted that IC-SAM itself may also cause a decrease in J_{SC}, depending on both concentration and initial ZnO quality (**Figure S3.6a**). While these properties interesting and warrant further exploration, their exact cause and nature is out of the scope of this study.

Given 3TZA's noteworthy effects, benzoic acid (BA) was explored, especially since BA derivatives, such as IC-SAM itself, are known SAM-formers.[171] At a glance, P3HT:PC$_{61}$BM devices respond to the introduction of BA and 3TZA similarly, demonstrating improvements in both JSC and FF which increase with additive concentration (**Figure 3.5**). Much like 3TZA, BA is absent from the bulk after processing, but a thin film of BA can improve devices with poor quality ZnO or overly-thick active layers. This suggests BA may also form a passivation layer (**Figure S3.7**), but due to the lack of heteroatoms and the thinness of a potential BA-TF passivation layer, we could not definitively ascertain the presence or absence of BA at the buried interface.

Despite these initial similarities to 3TZA, BA separately has some notable effects. In particularly, BA also increases PCE even in conventional devices (**Figure 3.5a**), suggesting beneficial morphological effects. Interestingly, while GIWAXS (**Figure S3.8**) reveals similar morphologies between 3TZA and BA-based devices, RSoXS shows that BA-based devices have domains with long period ~ 100 nm, while 3TZA-based devices have long periods ~ 34 nm (

Table S3.1). While a larger domain size would typically result in lowered J_{SC}, this is not what is observed. Indeed, introducing IC-SAM or saturated BA to prevent further passivation layer formation does not prevent continued concentration-based improvements in J_{SC} and FF (**Figure S3.3b,d, Figure S3.7**) in BA devices. This suggests there may be a strong morphological component associated with the addition of BA, despite its relatively large long period. Like 3TZA-based devices, future morphological characterization is required to fully understand our findings.

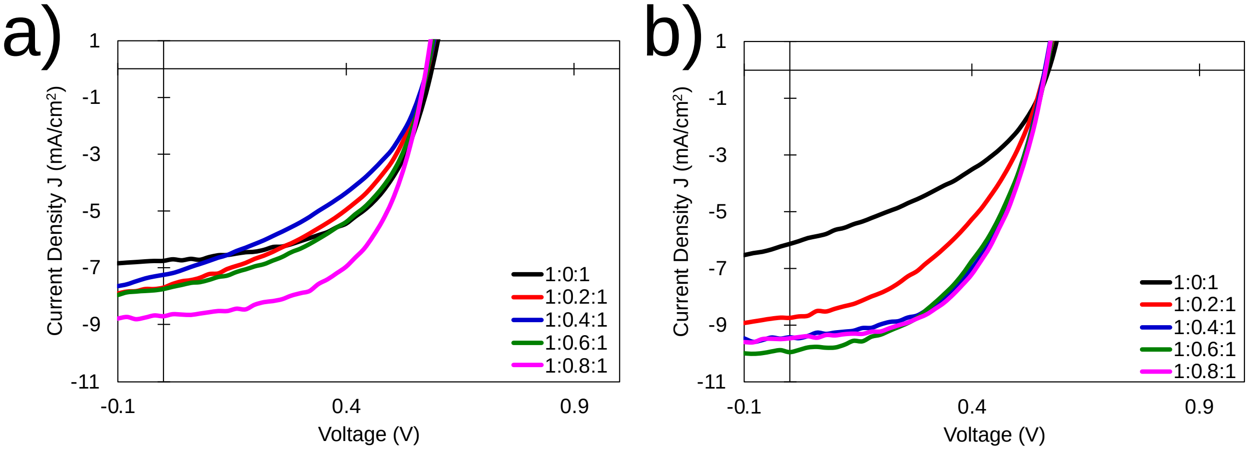

Figure 3.5. J-V curves of P3HT:BA:PCBM devices with the **a)** conventional architecture ITO/PEDOT:PSS/P3HT:BA:PCBM/Ca/Al and **b)** inverted architecture ITO/ZnO/P3HT:BA:PCBM/MoOx/Al

3.3.2. Base: 1-Napthylamine

1-Napthylamine (AN) was chosen as the model base. AN is an aromatic molecule with a structure almost identical to that of common additive CN, the only difference being the substitution of a nitrogen for the chlorine. In addition, AN is a solid at room temperature and has a much lower vapor pressure than CN. It is expected that a reactive group such as a primary amine would be largely detrimental upon addition. Indeed, a pronounced S-curve is seen in AN-based conventional devices upon addition, potentially indicative of a strong charge extraction barrier.[174] This is plausible, as nitrogen-containing compounds have been known to de-dope

PEDOT:PSS, causing a build-up of PSS at the interface.[175] In contrast, inverted AN-based devices actually demonstrated improved PCE due to increased J_{SC} and *FF*, much like the acidic molecules 3TZA and BA (**Figure 3.6**). It is notable that this improvement is present before any thermal annealing, with as-cast AN-based devices appearing visually similar to their thermally annealed additive-free counterparts (**Figure S3.9**). Like with the model acidic molecules, NMR shows that AN is no longer present in the bulk, so it is not actively contributing to bulk PV properties (**Figure S3.10**) again pointing us toward the buried interface to explain the observed behavior.

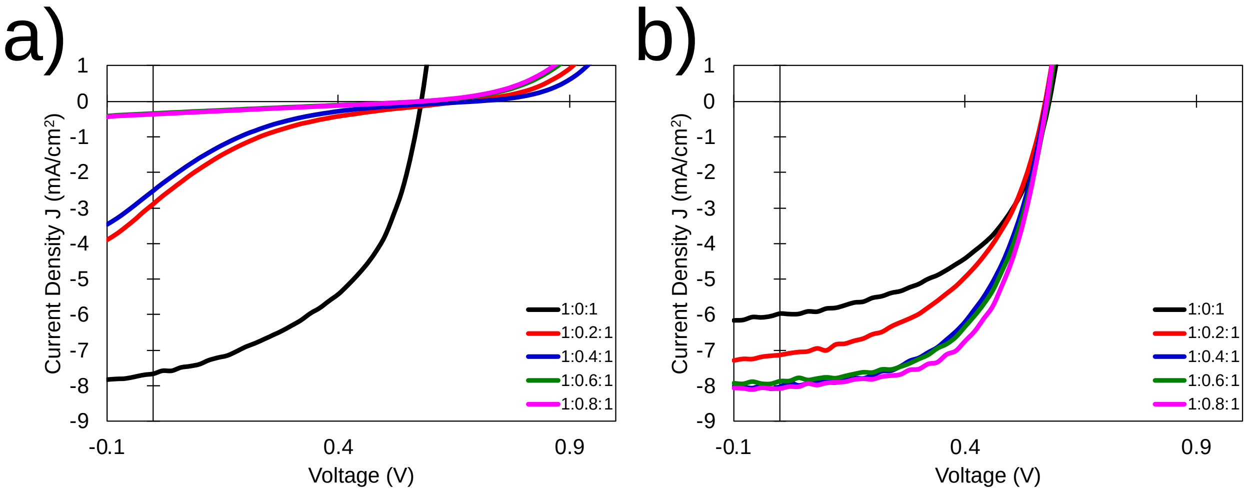

Figure 3.6. J-V curves of P3HT:AN:PCBM devices with the **a)** conventional architecture ITO/PEDOT:PSS/P3HT:AN:PCBM/Ca/Al and **b)** inverted architecture ITO/ZnO/P3HT:AN:PCBM/MoOx/Al

AN solution was deposited directly onto ZnO or PEDOT:PSS-coated substrates then subsequently washed with chloroform. It was immediately evident that the AN solution was unable to wet the ZnO surface. XPS confirmed there was little to no nitrogen present on the ZnO both before and after washing (**Figure 3.7**), indicating that the improvements seen in inverted devices not likely due to surface passivation effects such as what was seen with the acidic molecules. In contrast, AN was not only able to fully to coat the PEDOT:PSS surface, but also remained on the film after washing. More telling results lay with the sulfur peaks. Due to the differing chemical environment of PEDOT and PSS (S-C vs S-Ox), the relative amounts of each can be extracted using XPS. For the PEDOT:PSS formulation used in our case (Al4083), the PEDOT:PSS ratio is ~ 1:6,[175] in line with our neat PEDOT:PSS XPS data. However, when a thin film of AN is deposited, the PEDOT:PSS ratio becomes closer to 1:10 (**Figure 3.7**). Because XPS is a surface-sensitive technique, penetrating only a few nanometers into the sample surface, this reduced ratio is suggestive of surface enrichment of non-conductive PSS. This supports our suspicion that AN is de-doping the PEDOT:PSS, hindering charge extraction. Moreover, the more hydrophilic PSS-enriched surface may negatively impact vertical phase separation, as PCBM is known to aggregate more strongly on hydrophilic surfaces.[169]

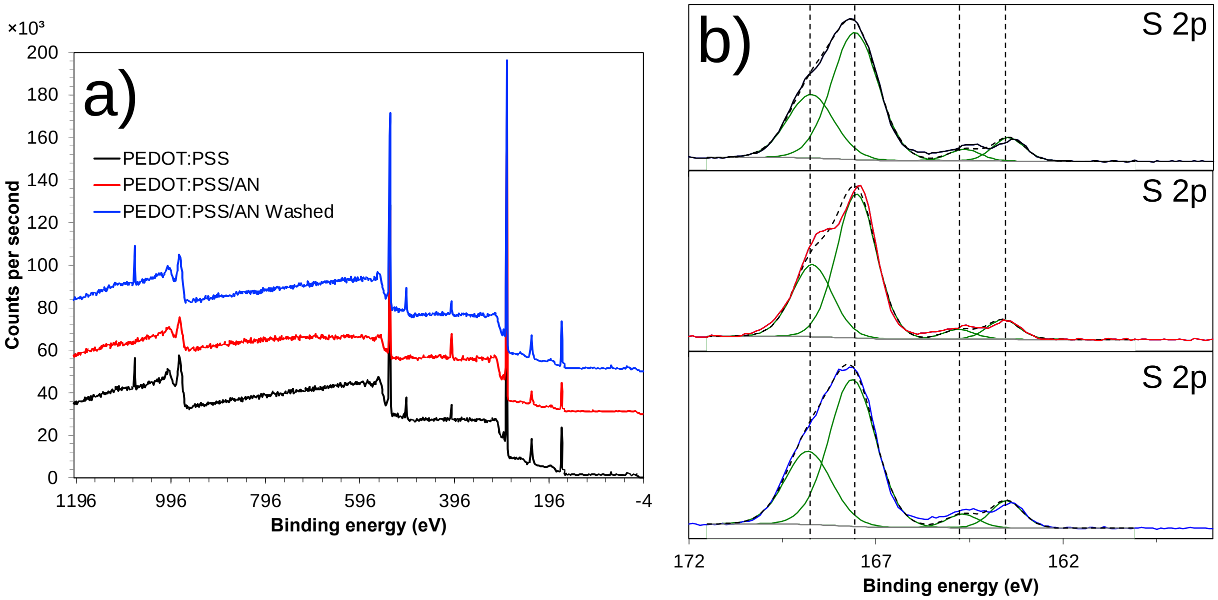

Figure 3.7. XPS **a)** survey scans and **b)** S 2p spectra of PEDOT:PSS and PEDOT:PSS/AN surfaces.

Interestingly, despite the strong interlayer interaction in conventional devices and lack thereof in inverted devices, GIWAXS reveals similar morphology for both (**Figure S3.8**). Furthermore, AN-based devices have somewhat large long periods ~ 70 nm compared to ~ 30 nm for P3HT:PC$_{61}$BM (

Table S3.1). This is potentially combat by the markedly face-on geometry, unlike the edge-on P3HT:PC$_{61}$BM. AN also appears to enhance active layer morphology even without thermal annealing (**Figure S3.9**), which would be beneficial to large-scale processing. Notably, devices which used known solvent additive CN were also edge-on in texture despite its structural similarity to AN (**Figure S3.8**). This makes AN unique among the solid additives in that it not only enhances crystallinity (like CN), but also changes the film to a more favorable texture. This property may warrant future exploration, perhaps also in conjunction with other additives.

3.3.3. Ionic Molecule: Pyridinium Hydrochloride

Ionic molecules are expected to be largely detrimental to OPVs. Not only may they contribute to charge trapping, but their reactive degradation products may interact with the active or interfacial layers. Here, the aromatic solid salt pyridinium hydrochloride (PyHCl) is chosen as the model ionic compound. Unlike all other additive molecules, ~ 25% of the PyHCl in remains in the bulk after processing (**Figure 3.8**). Despite this, it is relatively well-tolerated in conventional devices (**Figure 3.9**), indicating that PyHCl itself does not have severely deleterious effects on PV performance, contrary to what we expected. In inverted devices, however, PyHCl appears to cause catastrophic failure even at 20 wt%. The morphology obtained from GIWAXS does not reveal any drastic differences, though inverted devices appear to have stronger edge-on preference (**Figure S3.8**). This led us to again look to the ZnO interface.

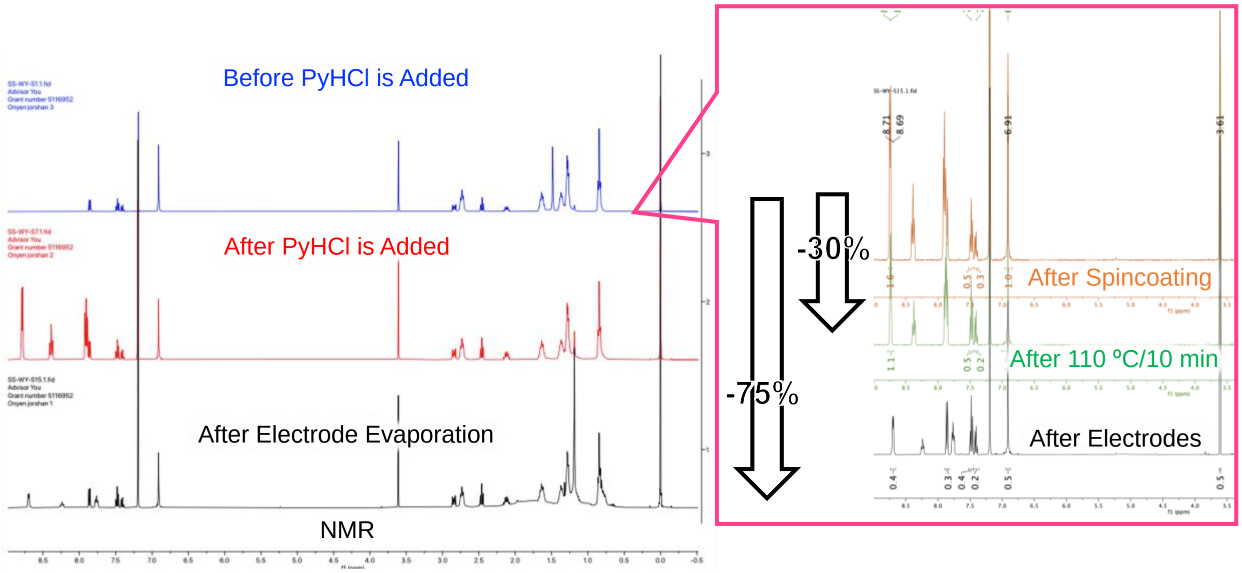

Figure 3.8. ^{1}H NMR spectra of P3HT:PC$_{61}$BM containing 80 wt% PyHCl during different steps of processing. Electrode evaporation is done under vacuum ~ 10^{-6} mbar. Highlighted areas indicate representative PyHCl peaks.

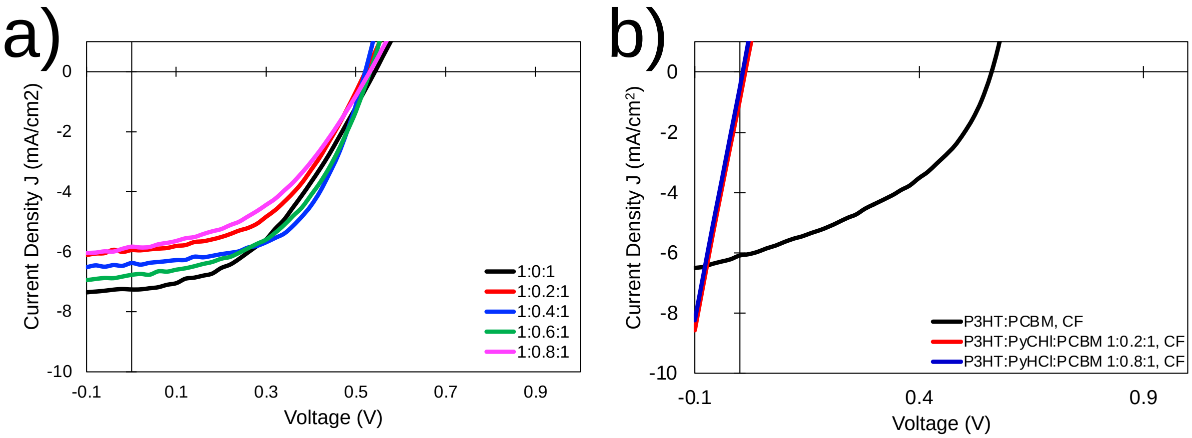

Figure 3.9. J-V curves of P3HT:PyHCl:PCBM devices with the **a)** conventional architecture ITO/PEDOT:PSS/P3HT:PyHCl:PCBM/Ca/Al and **b)** inverted architecture ITO/ZnO/P3HT:PyHCl:PCBM/MoOx/Al

To probe the buried interface, XPS was performed on model interfaces comprising PyHCl cast onto ZnO or PEDOT:PSS. This revealed that nitrogen was largely absent on samples cast on PEDOT:PSS, but was present on ZnO-based samples both before and after washing with chloroform. Moreover, the N:Zn ratio only decreased ~ 20%, indicating N may be fairly tightly bound to the interface, in addition to being present in the bulk (**Figure 3.10**). Interestingly, there appears to be an oxidized nitrogen species (around 403 eV) present on PyHCl-coated ZnO, but it is removed entirely after washing with chloroform. Further or repeated experiments may be needed to determine whether this oxidized nitrogen species originates from PyHCl or contamination.

To probe the effect of this interface independently from morphology, we cast P3HT:$PC_{61}BM$ onto ZnO coated with PyHCl cast from 10, 5, and 0.5 mg/mL solutions (**Figure S3.13**). Even at low concentrations, there is a marked loss in V_{OC}, *FF*, and J_{SC} until the point where the J-V curve begins to resemble shorting behavior. Estimating the shunt and series resistance from the J-V curves at open circuit and short circuit conditions, respectively, we found that R_{sh} decreases dramatically, falling by nearly an order of magnitude. On the other hand, R_s decreases by only a factor of 3. Furthermore, the presence of PyHCl on the surface also strongly influences the work function of ITO/ZnO, increasing ionization energy from 7.34 eV to 9.17, 9.02, and 7.65 eV and work function Φ from 3.52 eV to 4.17, 4.42, and 3.85 eV for PyHCl coated at concentrations of 10, 5, and 0.5 mg/mL, respectively (**Figure S3.2b**). While this change is certainly not negligible, it cannot explain the loss in performance. Indeed, the Φ of the PyHCl-coated ZnO is even closer to $PC_{61}BM$'s energy level then neat ZnO, so it should not result in the marked loss of performance we observed. However, if this change in Φ were caused by doping of the ZnO, then perhaps it is contributing to the shorting behavior. However, resistance measurments taken from PyHCl-coated ZnO (ITO/ZnO/PyHCl/MoOx/Al) show an opposite trend where higher concentrations of PyHCl increase resistance by roughly two-fold (**Table S3.2**). If doping was the cause of the lower Φ, then we should expect a decrease in resistance instead. Thus, the failure behavior of these devices certainly requires further study as it may not be soley attributable to the bulk or interface.

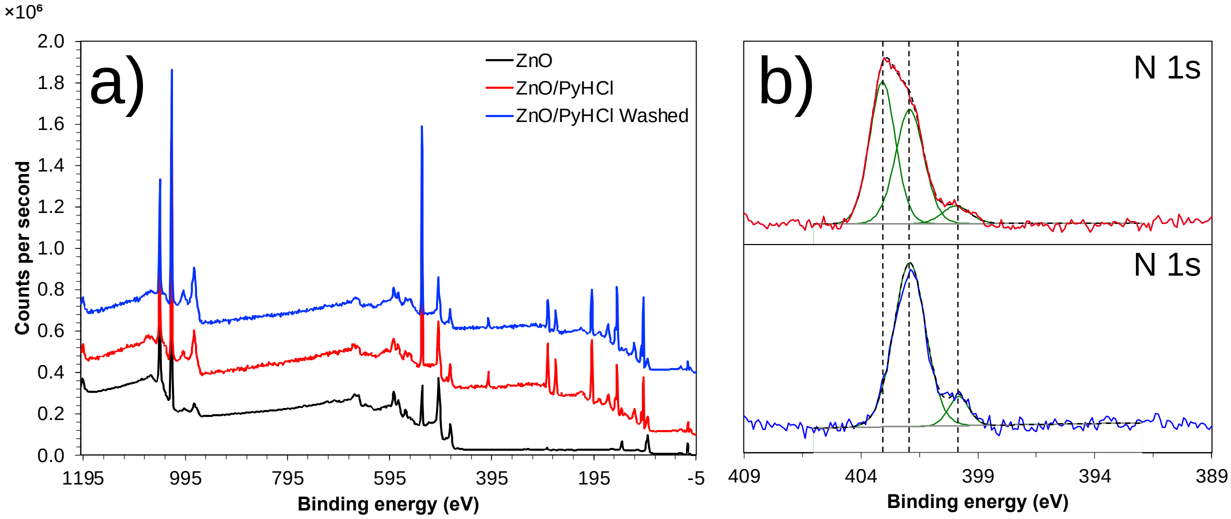

Figure 3.10. XPS **a)** survey scans and **b)** N 1s spectra of ZnO and ZnO/PyHCl surfaces.

3.3.4. Solvent Effects

In addition to chloroform (CF), devices were also cast from chlorobenzene (CB) and ortho-dichlorobenzene (oDCB)—all solvents commonly used for P3HT:$PC_{61}BM$ devices. In most cases, the behavior of devices cast from CF and devices cast from CB had similar concentration-dependent trends with some differences in the magnitude of the effect. On the other hand, oDCB proved to be an unsuitable processing solvent in most cases (**Figure S3.14** - **Figure S3.18**), likely due to its slow drying time. This allows for the additives to aggregate and is exacerbated by the additional solvent annealing step typically used to optimize P3HT:$PC_{61}BM$ OPVs cast from oDCB. The large crystallites of what is most likely additives form regardless of the additive and interlayer, though the severity and threshold concentration varies. 3TZA and BA cast from oDCB onto PEDOT:PSS, for example, experience only minor reductions in J_{SC} until 80 wt%, where notable losses in J_{SC} and FF occur. In contrast, 3TZA and BA cast from oDCB onto ZnO exhibit drastic losses in all PV FoM even at 20 - 40 wt% (**Figure S3.14**, **Figure S3.15**). This difference may be due to differences in surface energy between the substrates, though the exact cause is out of the scope of this study.

3.4. Conclusions

While we hypothesized that power conversion efficiency (PCE) would always be reduced (though to varying degrees), this was not the case. Surprisingly, most of these chemically active, high-boiling point solid additives are no longer detectable in the bulk after processing. Furthermore, the introduced reactive groups had only minor impacts on the OPV morphology, except for AN, which promoted crystallinity and a face-on texture. However, the most surprising result was the additives' interactions with the interlayers. 3TZA and BA, while tolerated in the conventional configuration, were beneficial in the inverted configuration where they essentially introduced a ZnO passivation layer during casting. AN and PyHCl in contrast, were beneficial or tolerated in one configuration, while highly detrimental in the other. Based on these results, solid impurities may not be as detrimental is generally believed, but care must be taken to consider interactions with the interlayers as well.

CHAPTER 4: IMPROVING LIFETIME THROUGH MORPHOLOGICAL ROBUSTNESS[2]

CASE STUDY: THE REMARKABLE STABILITY OF THE RP-TCS SERIES

4.1. Synopsis

For emerging technologies such as organic photovoltaics (OPVs) to be industrially viable, they must demonstrate a combination of high efficiency, long lifetime, and low cost. On the one hand, the power conversion efficiency (PCE) of OPVs is quickly approaching a landmark 20%, on par with commercially available silicon solar cells; on the other hand, due to both the materials used and the delicate – often thermodynamically unstable – morphology, OPVs are still limited by their short lifetimes and high synthetic cost. Moreover, efficiency and stability often run counter to one another. Often, in attempting to stabilize an inherently unstable system, the optimal morphology is disturbed, resulting in a decrease in PCE. Previously, we demonstrated the remarkable thermal stability of a system based on fullerene acceptor and low-cost polythiophene-based donors incorporating thermocleavable side chains (TCS).[176] In this work, we found that despite a largely amorphous morphology in one of the TCS polymers based BHJ solar cells, the favorable domain size still afforded an appreciable efficiency of 1.5%, which only decreased less than 20% after 28 days of accelerated thermal aging beyond the blend materials' glass transition temperatures (T_g). Over this time, the morphology changed surprisingly little. Furthermore, we explored the effect of TCS content on charge carrier mobility, PCE, and OPV stability. Ultimately, we found that TCS content > ~ 70 mol% resulted

---

[2] Some tables and figures adapted from Son, S. Y., Samson, S., Siddika, S., O'Connor, B. T., & You, W. (2021). Thermocleavage of Partial Side Chains in Polythiophenes Offers Appreciable Photovoltaic Efficiency and Significant Morphological Stability. Chemistry of Materials, 33(12), 4745–4756.

in inadequate donor-acceptor mixing, leading to low efficiency, while TCS content < ~ 70 mol% provided neither superior stability nor efficiency.

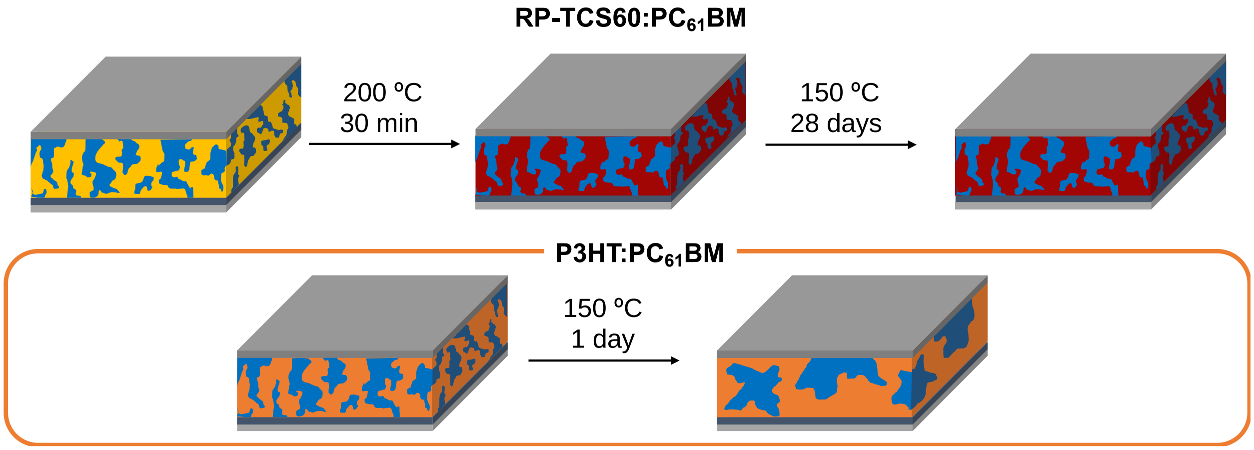

Figure 4.1. Simplified illustration of morphological changes occurring in RP-TCS60:PC$_{61}$BM systems compared to those of typical P3HT:PC$_{61}$BM systems.

4.2. Introduction

Although the efficiency of organic photovoltaics (OPVs) has enjoyed rapid improvement over the past few years, research into OPV lifetime is progressing at a comparatively sluggish pace, with many OPVs unable to retain PCE even during dark storage.[177] The active layer by itself is prone to both intrinsic degradation from light and heat and extrinsic degradation primarily from water and oxygen.[64] While the latter can be largely addressed by device encapsulation, the former requires stability of the individual components and the resulting often kinetically trapped morphology.[74,178] The active layer may further be susceptible to interactions with the interlayers it contacts. To slow the gradual demixing of the BHJ components, it is necessary to limit diffusion in the blend,[71,73,74,179,180] with a target diffusion coefficient around ~ 10^{-20} cm^2/s taken to be sufficient to lock morphology for a useful lifetime.[74]

Approaches to limit diffusion include, but are not limited to, crosslinking (both physical and chemical),[181–186] glass transition temperature (T_g) manipulation,[164,187–189] and ternary blending.[162–164,190–193] Many such techniques have been utilized in previous literature in attempts to vitrify BHJ blends with varying degrees of success. Inevitably, each of methods to enhance lifetime will also incur additional or increased costs. Physical/ternary blends require not only additional components but also additional processing to determine the optimal three-phase morphology. Meanwhile, chemical modification is, by nature, synthetically demanding. However, this added synthetic complexity can be alleviated by re-assessing synthetic methods[58] modifying an inherently low-complexity (thus low cost) system, such as P3HT:$PC_{61}BM$.

Indeed, other groups have attempted to vitrify P3HT:$PC_{61}BM$-based systems by increasing the T_g of the material. However, this is often associated with decreased solubility, leading to poorer film formation.[189] Fortunately, it has been shown that this can be mitigated through the introduction of thermocleavable side chains (TCS).[189,194,195] This approach involves heating the OPV following active layer deposition, reaping the benefits of the solubility afforded by the side chains to enable solution processed film while vitrifying the film to offer the stability after removing the side chain after thermocleavage.[189,194,195] Unfortunately, these systems could only reach a maximum PCE of 0.8%.[195] Building off this, our group synthesized a P3HT-based random copolymer with a different design. Specifically, instead of incorporating TCS onto each thiophene unit in previous studies, our newly designed polymer also included hexylthiophene units.[176] Moreover, instead of full cleavage of all side chains, we only partially cleaving the TCS (i.e., leaving a carboxylic acid group behind), allowing for lower-temperature processing (~ 150 - 200 °C instead of 300 °C, a temperature required to remove carboxylic acid as well). Using this TCS series of molecules, we found that thermally-cleaved RP-TCS60 (60% TCS content), could achieve ~1.5% PCE and withstand 150 °C (a temperature higher than the T_g (~ 120 °C) of even native polythiophene), 24 hour annealing under N_2 and dark conditions. This may be due in part to the remaining carboxylic acid groups on the thermally-cleaved polymer which may participate in hydrogen bonding with other polymers or $PC_{61}BM$ in the blend.[196] However, the long-term behavior and underlying mechanisms behind the enhanced stability of RP-TCS60 was still unknown. Furthermore, it was unclear whether or not systems using the other members of the RP-TCS series would also display enhanced stability. To this end, we explored the electronic and morphological properties of fresh and aged neat and blend films using the RP-TCS series (**Figure 4.2**), as understanding the mechanisms behind this stability could provide insight for future intelligent design of stable donor:acceptor systems.

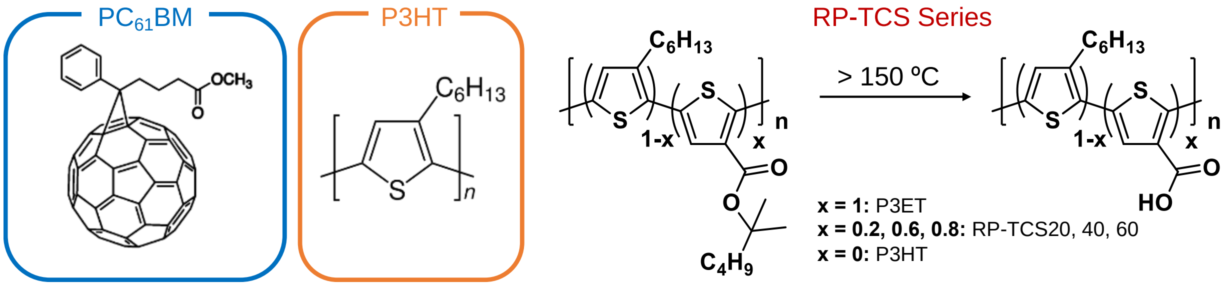

Figure 4.2. Chemical structures of materials used in this study.

4.3. Results and Discussion

4.3.1. Mobility

We first evaluated whether the neat material itself would provide adequate charge transport capability. Using the space charge limited current (SCLC) method, we extracted hole mobilities (μ_h) for the RP-TCS series polymers both before and after thermal cleavage. Following thermal cleavage, a pronounced color change was observed and film thickness decreased significantly. As-cast films had fairly low mobilities on the order of ~10^{-7} – 10^{-5} $cm^2/V{\cdot}s$ which increased to ~ 10^{-4} cm^2/Vs after thermal cleavage (**Figure 4.3**, **Table S4.1**). Interestingly, μ_h following thermal cleavage was largely consistent over the entire TCS series, despite the marked differences in as-cast μ_h. While this is not as high as μ_h of neat P3HT, this is on par with μ_h of other polymer donors used in OPVs.[197,198]

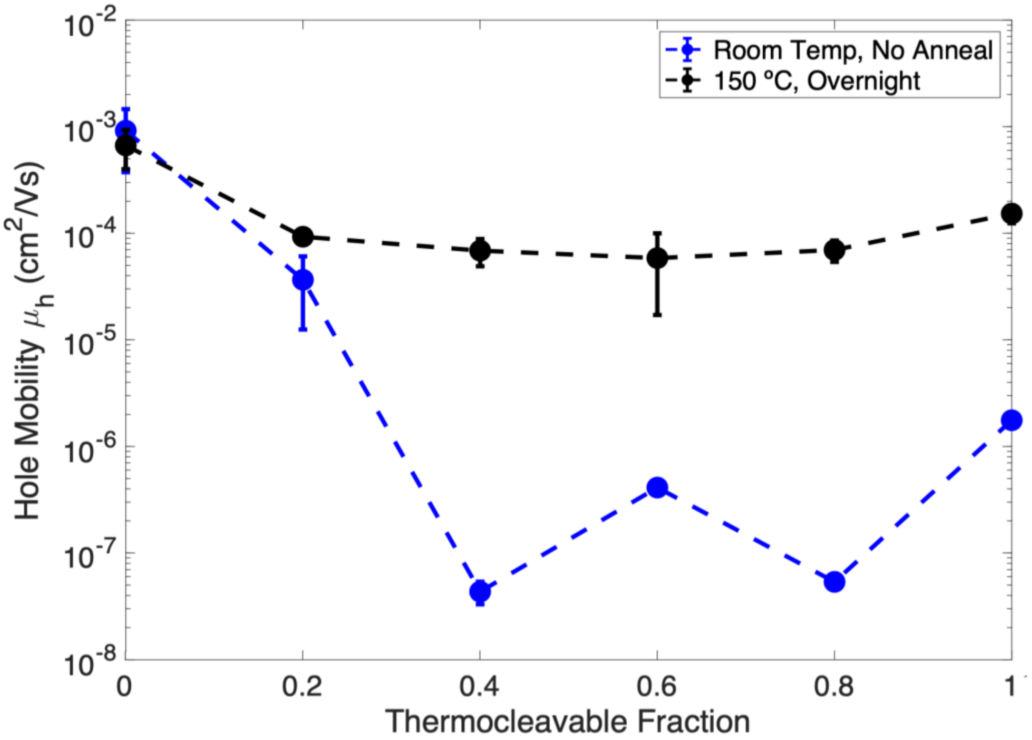

Figure 4.3. SCLC Hole mobility of neat RP-TCS Series polymers before and after thermal cleavage.

4.3.2. Photovoltaic Properties

Given adequate μ_h, we introduced the RP-TCS series polymers into BHJ blends with $PC_{61}BM$ with the architecture ITO/PEDOT:PSS/Donor:$PC_{61}BM$/Ca/Al. Notably, prior to thermal cleavage, even 20% TCS content caused a severe drop in J_{SC} and FF, while V_{OC} increase significantly. Following thermal cleavage, there was a marked increase in J_{SC} while FF remained relatively low. V_{OC} surprisingly remained high, in contrast to existing literature (**Figure 4.4**).[195,196] Surprisingly, PCE did not decrease monotonically with increasing TCS content (i.e., as the donor becomes less P3HT-like). Instead, there is a clear maximum in PCE around 40% - 60% TCS content.

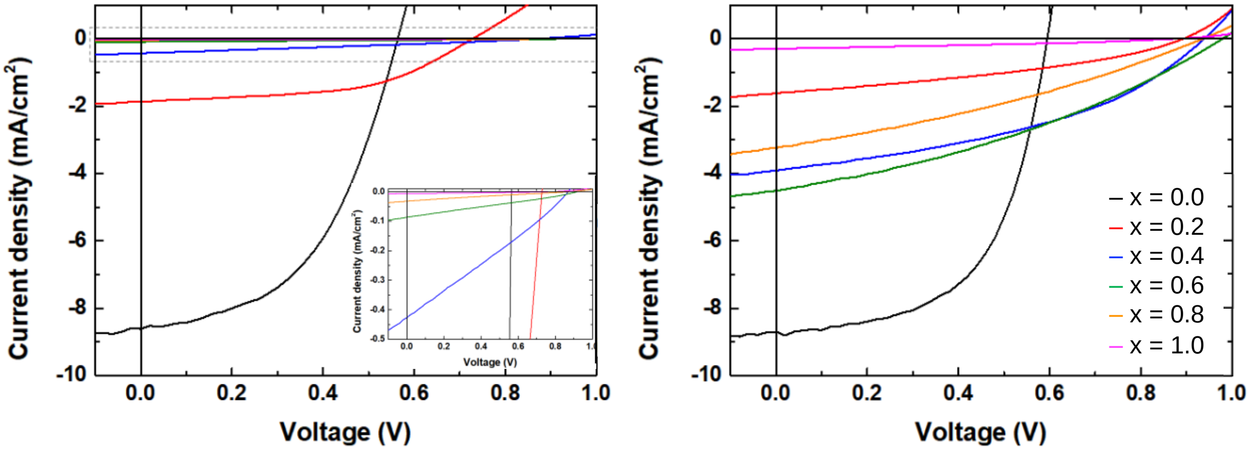

Figure 4.4. J-V curves of RP-TCS:$PC_{61}BM$ devices before (left) and after (right) thermal treatment. All annealing was done under N_2, in the dark. **Left:** Devices were annealed at 110 °C for 10 minutes. The dashed region is shown in the inset. **Right:** Devices were annealed at 200 °C for 30 minutes. Here, x is the fraction of TCS units, where x = 0 is P3HT and x = 1 is P3ET. Reproduced from previous work.[176]

4.3.3. Morphology

To investigate the observed trends in mobility and PCE, we extracted nanoscale crystalline and mesoscale morphology using grazing incidence wide angle x-ray spectroscopy (GIWAXS) and resonant soft x-ray spectroscopy (RSoXS), respectively. We chose to focus on the two extremes, the homopolymers P3HT and P3ET, and the RP-TCS copolymers which yielded the highest PCE in blends, RP-TCS40 and 60. Analysis of the GIWAXS patterns of neat films (**Figure 4.5**) indicates that increased mobility is likely due to beneficial changes in morphology. Prior to thermal annealing, both homopolymers P3HT and P3ET appear to be relatively crystalline with a clear edge-on texture compared to the randomly-oriented copolymers RP-TCS40 and 60. After thermal annealing, P3HT retains its edge-on with little to no change in π-π stacking distance (3.7 Å), consistent with our mobility measurements. In contrast, P3ET transitions from edge-on to face-on, though π-π stacking distance slightly increases from 3.7 Å to 3.8 Å (**Table S4.2**). Despite the slight increase in π-π stacking distance, the conversion to face-on aids in vertical charge transport, resulting in increased SCLC mobility from 10^{-6} to 10^{-4}

cm^2/V·s. As cast RP-TCS40 and 60 appear to have no preferred orientation, with amorphous rings indicating π-π spacings of 4.5 Å and 4.7 Å, respectively. After thermal cleavage, both RP-TCS40 and 60 take on an obvious face-on texture with π-π spacing of 3.7 Å and 3.6 Å, respectively. This is consistent with the respective increases in μ_h from 10^{-8} and 10^{-7} cm^2/V·s to 10^{-4} cm^2/V·s. Notably, this mobility increase in the case of RP-TCS copolymers is larger than that observed for P3ET, likely due to the large initial π-π spacing in the copolymers prior to thermal annealing.

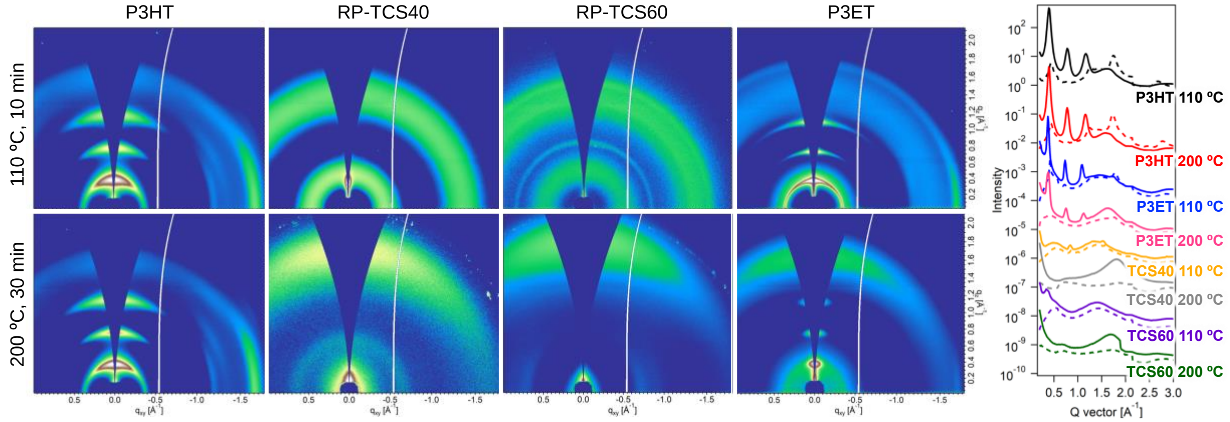

Figure 4.5. GIWAXS patterns and in-plane (dashed) and out-of-plane (solid) line cuts for neat P3HT, RP-TCS40, RP-TCS60, and P3ET thin films.

This trend, however, does not extend to the blend films. GIWAXS reveals P3HT:PC$_{61}$BM has a preferentially face-on texture with discernable π-π and lamellar spacing at 3.7 Å and 15.7 Å, respectively. Little change is seen in the crystalline morphology of P3HT:PC$_{61}$BM blends upon thermal annealing (TA) at 200 °C for 30 min, with RSoXS showing that there is similarly little change in long period. However, relative domain purity has increased noticeably for the annealed device (

Table S4.3, **Table S4.4**). In contrast, RP-TCS40, RP-TCS60, and P3ET films blended with $PC_{61}BM$ (pre-thermal annealing) do not have obvious π-π stacking peaks though there are what appear to be lamellar stacking peaks ~ 16 Å (with visible reflections in the case of RP-TCS40), suggesting the films are quite disordered. Following thermal annealing to remove alkyl chains, the lamellar stacking peaks are no longer observed in RP-TCS60 and P3ET blend films, though they remain visible in the GIWAXS pattern of the RP-TCS40 film. The visible remaining features are typical of $PC_{61}BM$.[199] RSoXS reveals long periods of ~ 42 nm and ~ 18 nm for RP-TCS40 and 60 based BHJ blends, respectively, which are largely unchanged after thermal annealing. However, after thermal annealing, domain purity for RP-TCS40 based blend film is significantly increased while that of RP-TCS60 based one is mostly unaffected. In both cases, despite the lack of crystallinity, it appears that the favorable domain spacing allowed for the devices to achieve ~ 1.5% PCE. Interestingly, the long period of P3ET based BHJ could not be extracted (no features visible in the RSoXS), suggesting that P3ET:$PC_{61}BM$ is completely mixed or that the domain size is too large to measure with this technique.

More distinguishing changes visible after aging at 150 °C for one day. In P3HT:$PC_{61}BM$ blend films, the $PC_{61}BM$ halo ~ 1.4 $Å^{-1}$ now has defined peaks while the orientational previously face-on texture has become more ambiguous (**Figure 4.6**). Furthermore, π-π spacing has increased to ~3.8 Å from ~ 3.7 Å, thought lamellar stacking distance is unchanged. RSoXS reveals aging a thermally annealed film further increases long period to ~ 88 nm while aged pre-thermal annealing films (i.e., films annealed at only 110 °C prior to aging) adopt a multi-length scale morphology afterward, with log-normal peaks fit to ~ 17, 22, and 33 nm (**Table S4.4**). The large loss in J_{SC} can be attributed to this suboptimal domain size and texture, while the loss in V_{OC} may arise the reduction of interfacial surface area (due to large, over-purified domains).[136] In

RP-TCS40 blend films, the lamellar stacking peak present prior to aging is no longer observed, suggesting that the morphology of RP-TCS40 based BHJ blend has continued to evolve after thermal cleavage. RP-TCS60 based BHJ blends, on the other hand, do not appear to have changed significantly based on GIWAXS, though RSoXS shows long period has increased slightly to ~ 20 nm. This is consistent with our previous findings for neat films, wherein enhanced stability is conferred at TCS content ≥ 60%.[176] P3ET, surprising, demonstrated the most extreme change in morphology, with the strong $PC_{61}BM$ peaks and now-discernable π-π and lamellar spacing at 3.8 Å and 15.7 Å, respectively.

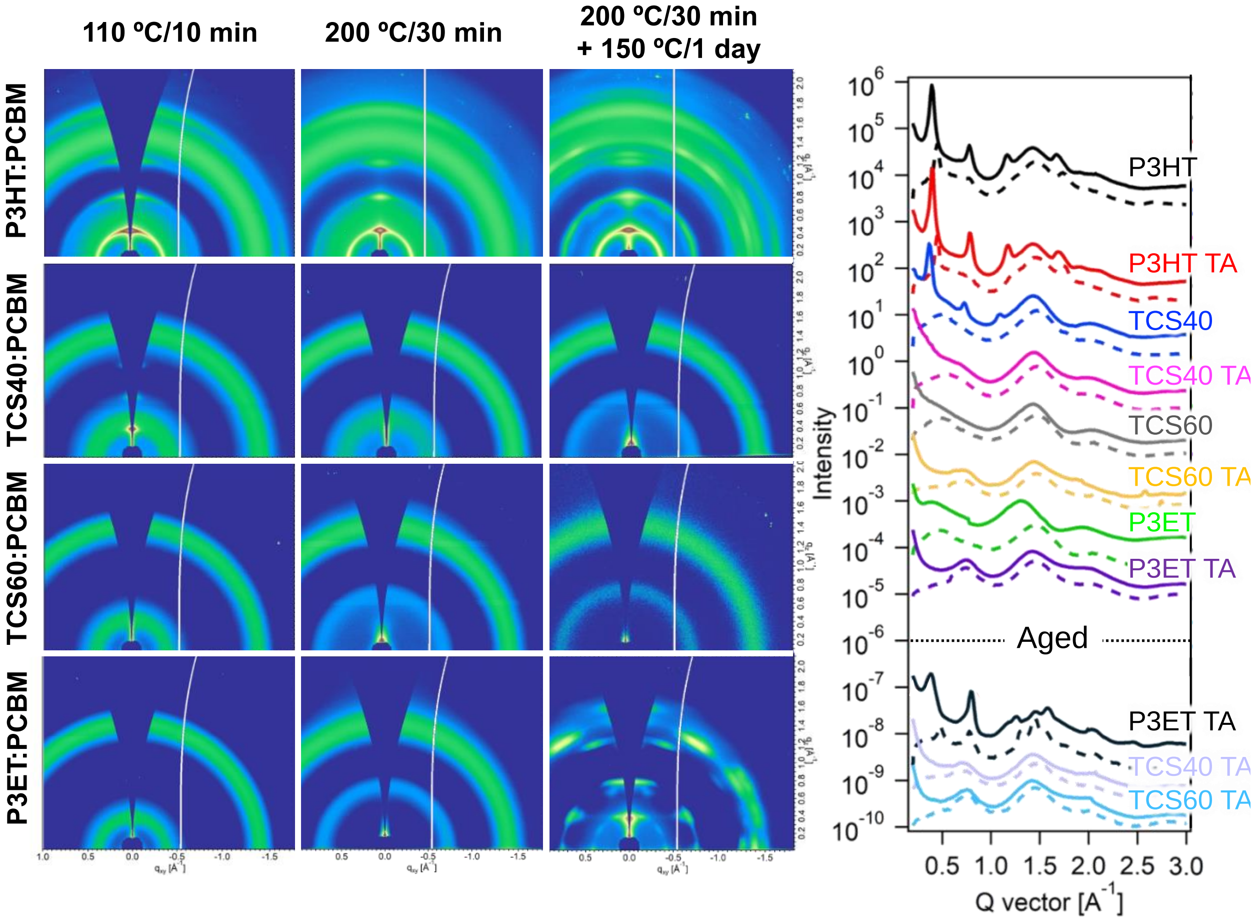

Figure 4.6. GIWAXS patterns and in-plane (dashed) and out-of-plane (solid) line cuts for blends films: P3HT, RP-TCS40, RP-TCS60, or P3ET with $PC_{61}BM$. TA indicates thermal annealing.

Further aging of RP-TCS60 and the homopolymers reveals that the morphology of RP-TCS60 remains relatively consistent even after a week of thermal annealing while both P3HT and P3ET blends still show evidence of enhanced crystallinity (**Figure 4.7**). RP-TCS60 blends remain disordered, with only $PC_{61}BM$-related peaks visible on GIWAXS. RSoXS reveals a small increase in long period from ~ 18 nm to ~ 26 nm, which is still favorable for charge transport. This mostly unchanged morphology is consistent with the observed stability of its PV performance. P3HT blends remain ambiguous in terms of orientational preference, in contrast to the initially face-on texture. π-π spacing has decreased to ~ 3.7 Å, potentially a bit less than pre-thermal annealing blends, while lamellar spacing remains unchanged from previous time points. P3ET based BHJ blend still demonstrates strong crystalline features and a preferentially face-on texture. Notably, the smearing of the discrete peaks into rings suggests that the further aged P3ET blend film has become less ordered. The π-π spacing has increased from 3.8 Å to 4.1 Å, while lamellar spacing has decreased from 15.7 Å to 15.4 Å. Again, no long period could be extracted from RSoXS data. Surprisingly, the morphology of P3ET:$PC_{61}BM$ appears to have evolved more than its P3HT-based counterpart, reaffirming that our P3ET blends are not morphologically stable.

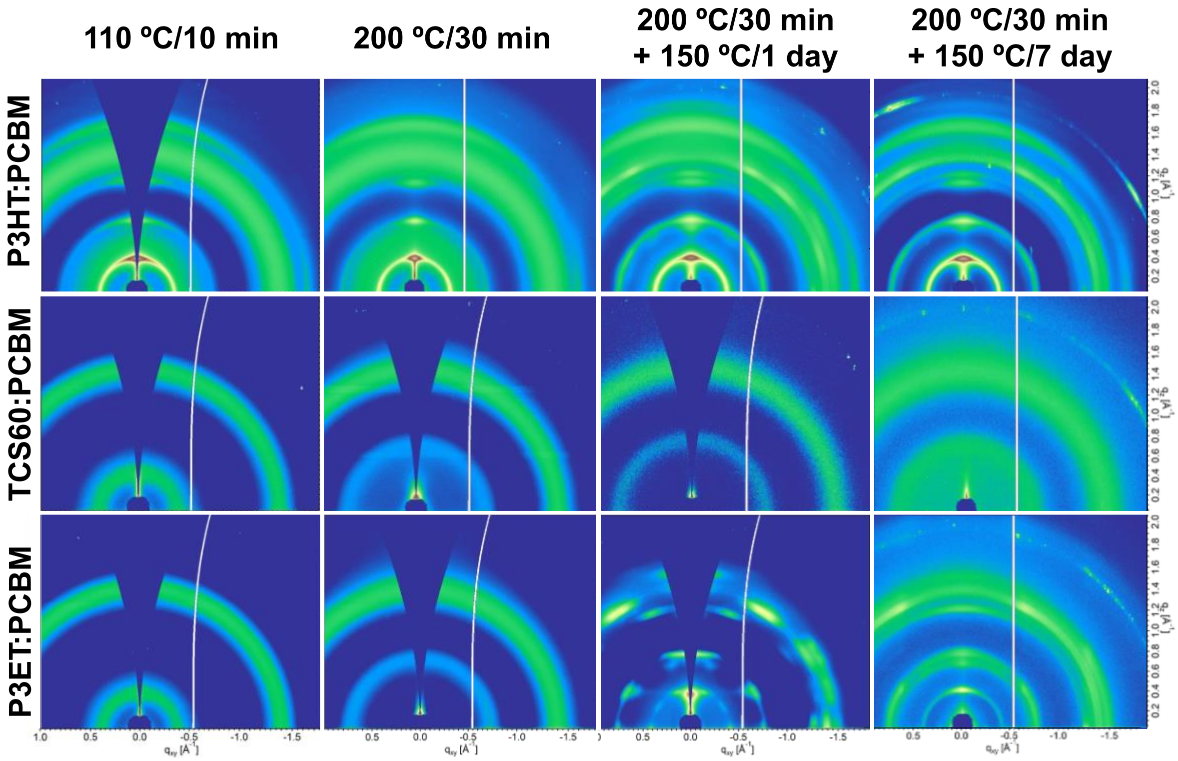

Figure 4.7. GIWAXS patterns of donor:PC$_{61}$BM blend films at various points of the accelerated aging process. All aging was done under N$_2$ in the dark.

On the surface, the evolving morphology of P3ET:PC$_{61}$BM suggests that thermally cleaved P3ET is insufficient in preventing PC$_{61}$BM from aggregating and crystallizing, which would contradict our previous work on neat films. However, it is important to consider the mesoscale morphology inferred from RSoXS. If indeed the domain sizes are excessively large to the point they cannot be measured by scattering techniques, then it is possible that the increased crystallinity is happening within these large, primarily single-component domains. On the other hand, if we could not extract long period from RSoXS due to excessive mixing, then we would expect the long period to increase with thermal stress. Taken to the extreme, if the blend is hyper-miscible, then there would be no driving force to separate the components and morphology would remain stable.[200] Investigating this further would require other techniques to measure domain size. Such techniques include scanning electron microscopy (SEM)[201] and infrared atomic force microscopy (AFM-IR)[202] where contrast arises from density differences and density and chemical composition, respectively. If in fact the domains are large, P3ET is too poorly miscible to prevent detrimental changes in morphology. If instead the blend is found to be highly (or hyper) miscible, then P3ET's enhanced T_g of course cannot confer enhanced stability to a blend that is not kinetically trapped.

4.3.4. Long-Term Stability

Given the appreciable PCE of RP-TCS60 based BHJ blend and its previously-demonstrated overnight thermal stability, we also chose to explore its long-term stability. Surprisingly, the remarkable stability of RP-TCS60:$PC_{61}BM$ extended up to, and potentially beyond, a month of accelerated testing. Indeed, only less than 80% of the initial PCE was lost after 28 days of annealing at 150 °C (**Figure 4.8**). Curiously, there appears to be some recovery behavior peaking around 10 days, though the cause is unclear. The slight increase may be due to differences in the device measured, as a different device was made for each time point to avoid any confounding effects due to electrode degradation. This recovery behavior is not unheard of and may be due beneficial changes in morphology[203], so cannot be discounted without further and/or repeated stability testing. Fitting the data to stretched exponentials (**Equation (1.4)**) yields T_{80}s of ~ 100 or ~ 40 days (**Figure S4.1**), depending on whether or not the recovery behavior is considered. However, these numbers are for accelerated conditions. To convert them to real-time T_{80}s, at least one thermal stability test at a different temperature must be performed. Then, **Equation (1.7)** may be used to extract real-time T_{80}. It should also be noted that it is unknown whether the thermal degradation behavior of RP-TCS60:$PC_{61}BM$ is decoupled from its light-induced degradation behavior. Thus, it would also be necessary to conduct light stability testing on RP-TCS60:$PC_{61}BM$ to determine its lifetime more accurately. However, this is a topic for another study.

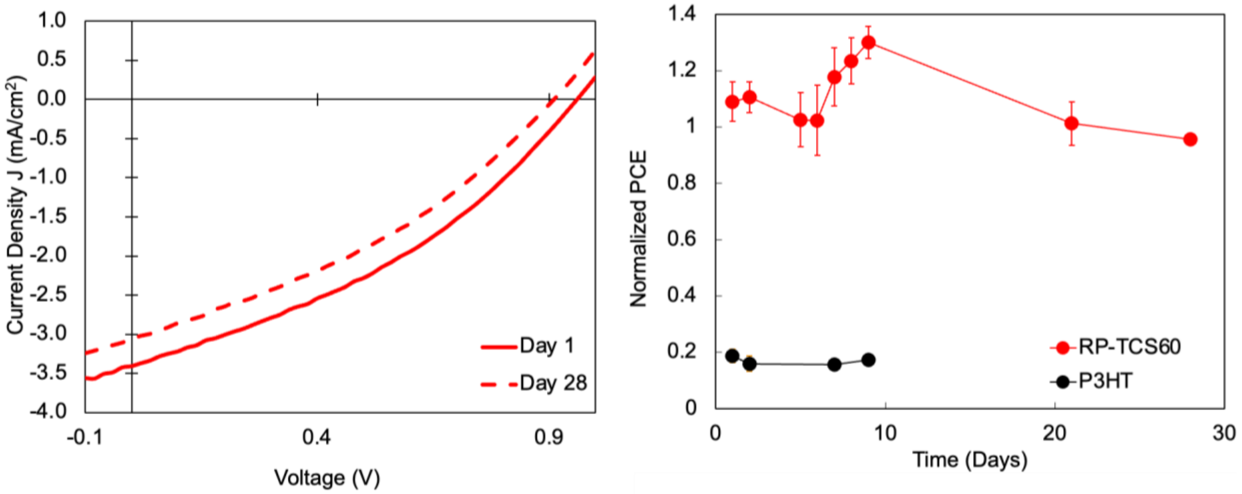

Figure 4.8. Long-term thermal stability of devices with architecture ITO/PEDOT:PSS/RP-TCS60:$PC_{61}BM$/Ca/Al. Accelerated aging was performed at 150 °C under N_2 in the dark.

4.4. Conclusions

In stabilizing an inherently unstable system, the optimal morphology is often disturbed, resulting in a decrease in PCE. In this work, we investigated the thermal stability P3HT-based random copolymers (RP) incorporating polythiophenes with alkyl and varying amounts of thermocleavable side chains (TCS), the RP-TCS series. The cause of the increased hole mobility μ_h was a transition to preferentially face-on stacking combined with a reduced π-π stacking distance. While this improvement in μ_h was seen across all donors in the series, few yielded devices with appreciable PCE. RP-TCS60 blends are not only more thermally stable than P3ET blends (despite P3ET having the highest T_g in the series), but also has a higher PCE than TCS20 and TCS40 (which are more P3HT-like) blends. Despite a largely amorphous morphology, the RP-TCS60:$PC_{61}BM$ based BHJ blend had a favorable domain spacing ~ 20 nm, allowing it to achieve and maintain ~ 1.5% PCE over 28 days. Furthermore, this morphology was largely unchanged despite prolonged thermal aging. While the RP-TCS40:$PC_{61}BM$ based BHJ blend also demonstrated appreciable PCE ~ 1.5%, its morphology evolved more than that of RP-TCS60 after thermal annealing. By contrast, the P3ET:$PC_{61}BM$ based BHJ blend, due either overly large or overly mixed domains, could not provide enhanced stability as the original morphology was not amenable to it. Overall, we showed that RP-TCS60 hits a “sweet spot” of appreciable PCE and significant thermal stability through superior morphology compared to other polymers in the TCS series. Even at temperatures exceeding T_g of the blend materials, the blend is stable, potentially due to intermolecular interactions such as hydrogen bonding. This means that future molecules employing this thermocleavable strategy may also benefit from partial, rather than full, cleavage as is the norm. This could lead to not only enhanced stability, but also may have implications in reducing material costs by reducing synthetic complexity of TCS-containing materials.

CHAPTER 5: CONCLUSION

5.1. Perspective

While OPVs have certain advantages that make them natural candidates for niche and emerging applications, their low PCE, short lifetime, and high cost (i.e., the three corners of the golden triangle) hinder the path to market viability. Fortunately, concerted research efforts have seen PCE skyrocket in recent years, approaching the 20% benchmark. In contrast, optimizing OPV cost and lifetime is a highly multifaceted affair: we must consider not only the active layer, but also the other device aspects such as the interlayers, metal contacts, and any interactions between them and/or with the active layer. These aspects must also be studied in the long term to properly assess lifetime. This is a time-consuming endeavor, though accelerated testing can guide lifetime investigations. Furthermore, the same carefully engineered donor and acceptor materials used in high performance solar cells come at a literal cost, as synthetic complexity has been scaling upwards with PCE. These costs are driven up further, should the device be sensitive to batch-to-batch material variation or impurities during processing. This dissertation aimed to highlight these difficulties and showcase approaches which can be taken to overcome them. Though not an exhaustive study of all potential routes to approach this complicated engineering challenge, the case studies contained here demonstrate that cheaper, more stable OPVs are not out-of-reach.

5.2. Design Requirements for Robust OPVs

To guide the design of OPVs toward commercial viability, we must be aware of costs incurred of both materials and processing as well as the stability of our devices.

5.2.1. Reduced Materials Cost

Batch-to-batch variability can strongly impact morphology and thus PCE. Many polymer donors have a relatively narrow MW range in which they adopt an optimal morphology (and thus peak PCE). Moreover, this range may differ depending on the acceptor material used. In contrast, FTAZ has previously been shown to afford peak PCE over MW ranging from 30 - 120 kg/mol for both archetypal fullerene and polymer donors, $PC_{61}BM$ and N2200. In Chapter 1, we probed for FTAZ's MW-insensitive behavior when blended with the archetypal FREA, ITIC. Once again, there is little change in morphology and PCE above donor MW 30 kg/mol. While PCE was consistent, there were changes in J_{SC}, FF, and V_{OC} trending with MW at the higher and lower ends of the MW range. J_{SC} and *FF* could largely be traced back to crystallinity and domain size, while V_{OC} was attributed to changes in recombination that are possibly stem from differences in domain purity. Despite these changes in PV FoM, the balance between them resulted in similar PCE. Though it is not yet clear exactly what causes this phenomenon over all donor categories, this study shows that such a material may be used to cut costs associated with stringent MW control.

5.2.2. Reduced Processing Cost

While active layer material synthesis comprises more than half the costs associated with OPVs, it is important to consider all parts of the manufacturing process. In particular, we must take care to remove impurities from our materials and solvents. Impurities are widely considered to be detrimental to the OPVs, potentially causing trap states and reducing morphological stability – especially if they remain in the film. In Chapter 3, we introduced solid conjugated solid small molecule additives (similar materials that may be encountered during polymer synthesis, for example) with active functionalities (i.e. acid, base, and ionic) to the low-cost archetypal system, P3HT:$PC_{61}BM$. Surprisingly, the additives were not always detrimental, even at concentrations up to 80 wt%. In fact, 3TZA and BA were found to positively impact inverted devices, primarily by passivating the ZnO ETL. AN was able to enhance morphology, improving crystallinity and inducing a face-on texture. The latter effect is especially surprising as not even CN could achieve such an effect. Even the ionic molecule PyHCl was not necessarily detrimental and was actually well-tolerated in the conventional architecture with PEDOT:PSS as the HTL. Moreover, most negative effects were traced back to the solid additives interacting with the interlayers, stressing the importance of considering interactions between all parts of the OPV. Finally, the last surprise was the absence of all solid additives (except for PyHCl) in the bulk after OPV fabrication, which involves mild heat and high vacuum. Our findings with these model molecules suggest that impurities may not always be detrimental and that it may be possible to relax stringent purification and processing to reduce costs. Furthermore, some of these solid additives may be useful in removing processing steps, such as 3TZA and BA, which can be used to deposit a ZnO passivation layer concurrently with the active layer.

5.2.3. Improved Lifetime

The PCE-optimized BHJ OPV is often fragile and prone to both intrinsic and extrinsic degradation initiated by stressors such as light, heat, and moisture. All these stressors would be expected during typical use and, while extrinsic degradation can often be avoided by proper encapsulation, the primarily morphological intrinsic degradation cannot. In Chapter 4, we investigated this morphological degradation using co-polymers based on low-cost donor, P3HT, featuring thermocleavable side chains (TCS). We found RP-TCS60 (featuring 60 mol% TCS) to be remarkably stable under aggressive thermal stress. Despite the temperature exceeding the T_g of our active layer materials, the carboxyl functionality granted by the TCS likely allowed for intermolecular interactions to help limit diffusion. The morphology of RP-TCS60:$PC_{61}BM$ was remarkably stable, showing little change over 28 days of accelerated testing and losing < 80% of its initial PCE. This corresponds to an impressive thermal T80 > 40 days under accelerated conditions. However, this behavior did not extend to the rest of the RP-TCS series. Although all RP-TCS polymers exhibited $\mu_h \sim 10^{-4}$ cm^2/Vs after TCS cleavage, only blends featuring RP-TCS40 and RP-TCS60 could achieve PCE > 1%. Unfortunately, RP-TCS40 blends did not demonstrate the same level of morphological stability, consistent with our observations for neat films (which require TCS ≥ 60 mol% for enhanced stability). Surprisingly, P3ET blends appeared to contradict our neat film observations. Though P3ET blends were expected to have high stability, we observed $PC_{61}BM$ crystallization after only one day of aging. We found P3ET:$PC_{61}BM$ likely had an excessively large domain size, suggesting that P3ET and $PC_{61}BM$ were too poorly miscible to afford high efficiency or enhanced stability. Thus, we showed that partial incorporation and cleavage of TCS is not only sufficient, but superior to, the complete cleavage of side chains in terms of PCE, stability, and processability.

5.3. Outlook

Undeniably, OPVs still fall short in terms of cost and lifetime. To add salt to the wound, less than 20% of OPV literature focuses on these shortcomings (**Figure 5.1**), meaning progress in these areas may not advance as quickly as PCE has over the last decade. Of course, this is not to say OPVs are forever doomed to be expensive, short-lived novelties. On the contrary, accelerated testing suggests that lifetimes upwards of decades may be achievable, though we must carefully temper our expectations of such estimates until field measurements can be acquired. In addition, syntheses can be revisited and streamlined to lower the cost of high-performance materials. Moreover, OPVs can be designed to perform robustly against material variation and potential impurities to lower processing costs. While we have highlighted these possibilities in this dissertation, there is certainly more work to be done on the road to commercial viability. Beyond hitting cost and lifetime benchmarks, the characterization of OPVs has yet to be standardized. Though standardized testing methodologies and industrial figures of merit have been proposed, they have not been widely adopted, making it difficult to directly compare cost and lifetime results between studies. Aside from the issues mentioned, OPVs must still meet other challenges related to processing including achieving large area, thickness-insensitivity, green processibility, and R2R compatibility. Still, filling in the corners of the golden triangle is a solid step toward realizing commercial OPV technology.

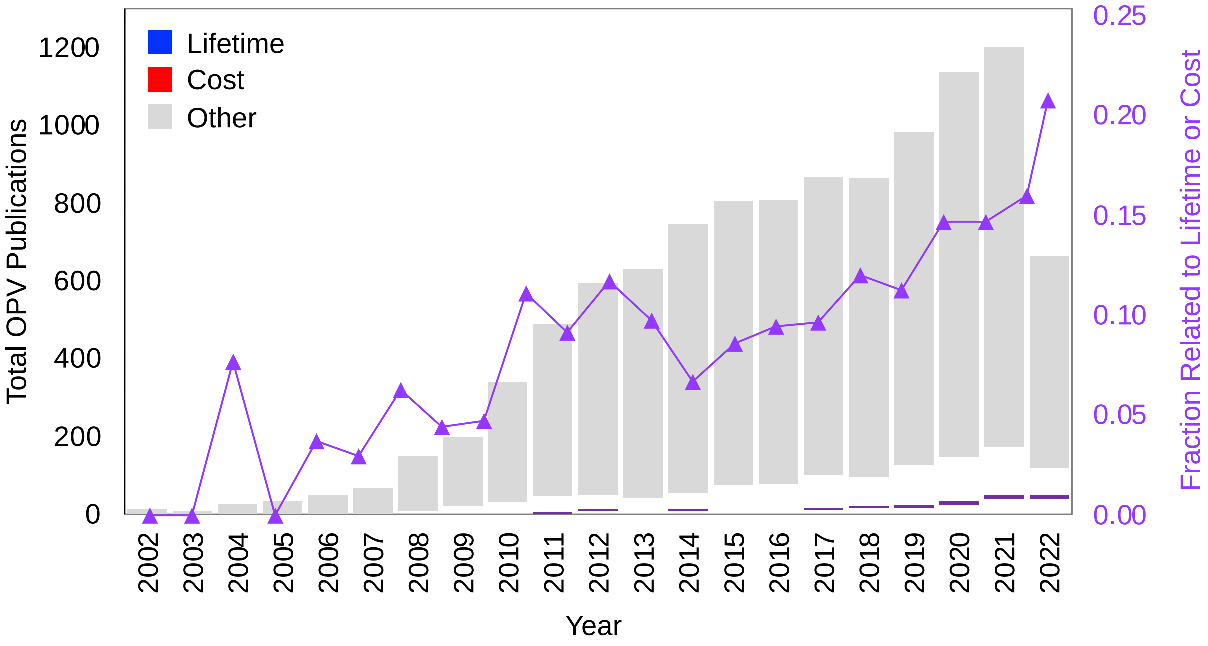

Figure 5.1. Annual fraction of OPV literature discussing lifetime or cost. Purple regions on the bar plot indicate publications that discuss both topics.

APPENDIX A: SUPPORTING INFORMATION FOR CHAPTER 2

Polymer Synthesis and Characterization

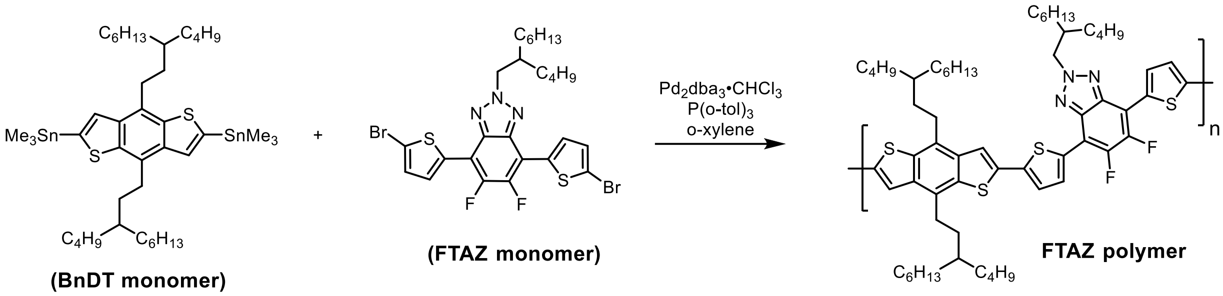

BnDT monomer (see below), FTAZ monomer (see below), $Pd_2(dba)_3{\cdot}CHCl_3$ (1.9-2.0 mg, 0.002 mmol, 0.02 eq.) and $P(o\text{-}tol)_3$ (4.9-5.0 mg, 0.016 mmol, 0.16 eq.) were charged into a 10 mL vial designed for microwave reactor. The mixture was evacuated and refilled with argon for three cycles before addition of anhydrous o-xylene under an argon stream. The reaction was heated up to 200 °C and held at that temperature for 10 min in a CEM microwave reactor. After the polymerization, the crude polymer was dissolved in hot chlorobenzene and precipitated into stirring methanol. The collected polymer was extracted via a Soxhlet extractor with ethyl acetate, hexanes, and chloroform. The polymer solution in chloroform was concentrated under reduced pressure/rotavap, and the polymer was redissolved into a minimal amount of hot chlorobenzene and precipitated into methanol. The polymer was then collected via vacuum filtration and formed a thin metallic golden colored film, which was then dried under vacuum.

Note: the molar mass of the polymer can be controlled by tuning the ratio of the BnDT and FTAZ monomers, as shown below:

10K FTAZ: BnDT (79.4 mg, 0.090 mmol, 1.20 eq) and FTAZ (48.5 mg, 0.075 mmol, 1.0 eq).

Yield = 80 mg (100%)

30K FTAZ: BnDT (94.4 mg, 0.107 mmol, 1.07 eq) and FTAZ (64.5 mg, 0.100 mmol, 1.0 eq).

Yield = 102 mg (93%)

40K FTAZ: BnDT (91.5 mg, 0.104 mmol, 1.04 eq) and FTAZ (64.5 mg, 0.100 mmol, 1.0 eq).

Yield = 105 mg (98%)

60K FTAZ: BnDT (89.8 mg, 0.102 mmol, 1.02 eq) and FTAZ (64.7 mg, 0.100 mmol, 1.0 eq).

Yield = 104 mg (98%)

100K FTAZ: BnDT (88.9 mg, 0.101 mmol, 1.01 eq) and FTAZ (64.5 mg, 0.100 mmol, 1.0 eq).

Yield = 105 mg (100%)

120K FTAZ: BnDT (88.0 mg, 0.100 mmol, 1.00 eq) and FTAZ (64.7 mg, 0100 mmol, 1.0 eq).

Yield = 97 mg (93%)

High temperature gel permeation chromatography. (HT-GPC) measurements were performed on an Agilent PL220 instrument with TCB as the eluent (stabilized with 250 ppm BHT) at 160 °C. The obtained molar mass is relative to the polystyrene standard.

Cylic Voltammetry. CV measurements were carried out on solid films using a Bioanalytical Systems (BAS) Epsilon potentiostat with a standard three-electrode configuration. A three electrode cell of a glassy carbon working electrode, Ag/Ag^+ reference electrode and Pt counter electrode were used. Films were drop-cast onto the glassy carbon electrode from hot chloroform solution (2 mg/mL, with tetrabutylammonium hexafluorophosphate added at 100% wt% relative to polymers) and dried using a heat gun. 0.1 M solution of tetrabutylammonium hexafluorophosphate in anhydrous acetonitrile was used as a supporting electrolyte. Scans were carried out under argon atmosphere at a scan rate of 100 mV/s. The reference electrode was calibrated using a ferrocene/ferrocenium redox couple. The HOMO in electron volts was calculated from the onset of the oxidation potential (E_{ox}) according to the following equation:

$$HOMO = -[4.8eV + e(E_{ox} - E_{Fc/Fc^+})]$$

UV-Visible absorption. Spectra were obtained with a Shimadzu UV-2600 spectrophotometer.

Device Fabrication

Patterned 25 mm × 25 mm ITO substrates were sonicated sequentially in deionized water, acetone, and isopropyl alcohol for 15 minutes each. The substrates were dried under a stream of nitrogen then treated with UV/Ozone for 15 minutes. Zinc oxide (ZnO) precursor solution was prepared from 1 g zinc acetate dihydrate and 0.28 g ethanolamine in 10 mL 2-methoxyethanol. The solution was stirred overnight, then filtered through a 0.2 µm PTFE syringe. The solution was spin-cast onto the clean ITO for 30 seconds at 4000 RPM then baked in air at 155 ℃ for 20 minutes. The substrates were transferred and stored in a nitrogen-filled glovebox until use. FTAZ:ITIC solutions were prepared with a 1:1 donor:acceptor ratio in toluene with a total mass concentration of 26, 19, 16, 12, 10, and 9 mg/mL for 10K, 30K, 40K, 60K, 100K, and 120K FTAZ, respectively. The solutions were stirred overnight at 80 ℃ in a nitrogen-filled glovebox, then heated to 100 ℃ for 30 minutes prior to spin coating. Afterwards, the solution was spin-cast on the prepared substrates for 1 minute at 1500 RPM then annealed at 150 ℃ for 15 minutes. The devices were finished by evaporating 10 nm MoO_3 and 70 nm Al through a shadow mask to produce 13 mm^2 devices. The devices were tested under AM 1.5G irradiation calibrated with an NREL-certified standard Si solar cell. J-V characteristics were measured with a Keithley 2400 digital source meter.

Morphology

Grazing Incidence Wide Angle X-ray Scattering. GIWAXS was measured at beamline 7.3.3 of Advanced Light Source (ALS) at Lawrence Berkeley National Laboratory.[204] The 10 keV X-ray beam was incident at a grazing angle of 0.13°, which maximized the scattering intensity from the samples and minimized the scattering intensity from the substrate. The scattered intensity was detected with a Dectris Pilatus 1M photon counting detector.

Resonant Soft X-ray Scattering. R-SoXS was measured at beamline 11.0.1.2 of the ALS[205] on blend films. Data were acquired at the photon energy of 283.6 eV where the contrast between polymer and fullerene is relatively high enough for these materials, yet does not lead to beam damage or background fluorescence.

Resistance Dependent Photovoltage

The source of a laser pulse to generate charges was a diode pumped, Q-switched Nd:YAG laser (NT242, EKSPLA) with 5 ns pulse duration at a repetition rate of 50 Hz. Photovoltage transients were recorded with an oscilloscope (Agilent DSO9104H) with a load resistance of 1 MΩ. Low laser pulse fluences were used to prevent screening of the internal field and a built-up of charges inside the device.[127]

Electroluminescence and EQE_{EL}

EL spectra were recorded with an Andor SR393i-B spectrometer equipped with a cooled silicon detector DU420ABR-DD and a cooled InGaAs DU491A-1.7 detector. EQE_{EL} values were obtained with a calibrated silicon photodiode (Newport) attached to a Keithley 485 Picoammeter, and a Keithley 2400 SourceMeter to apply the voltage and record the injected current.

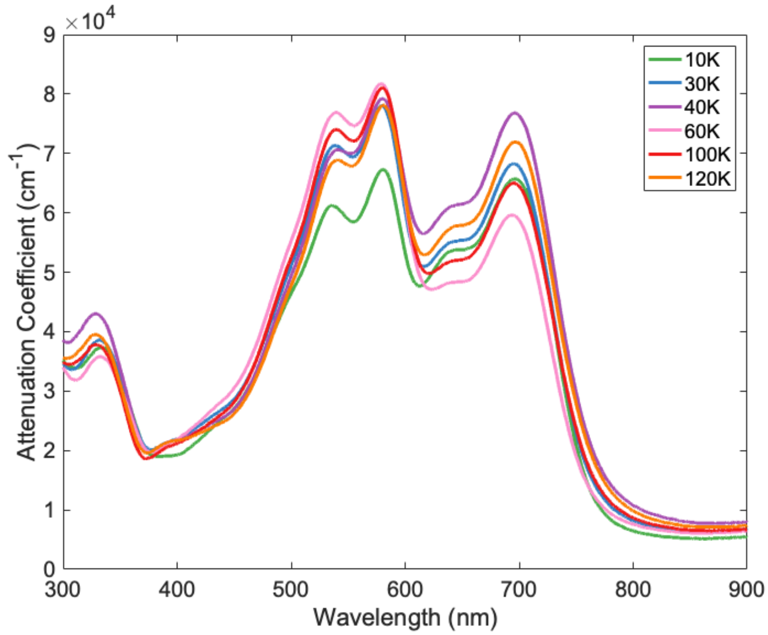

Figure S2.1. Absorption spectra for FTAZ:ITIC blend films.

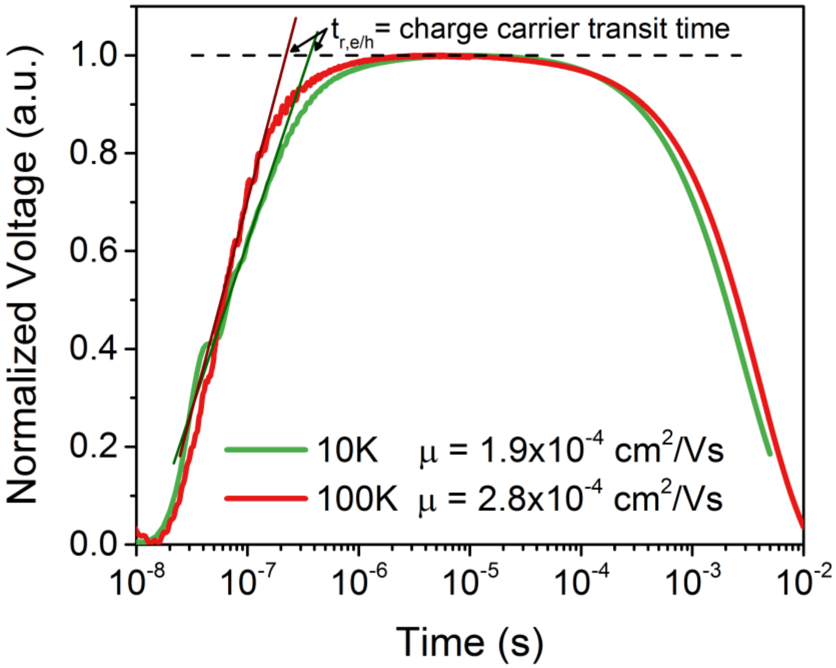

Figure S2.2. Resistance dependent photovoltage measurements used to measure charge carrier mobility in the blend films. The transients indicate balanced transport.

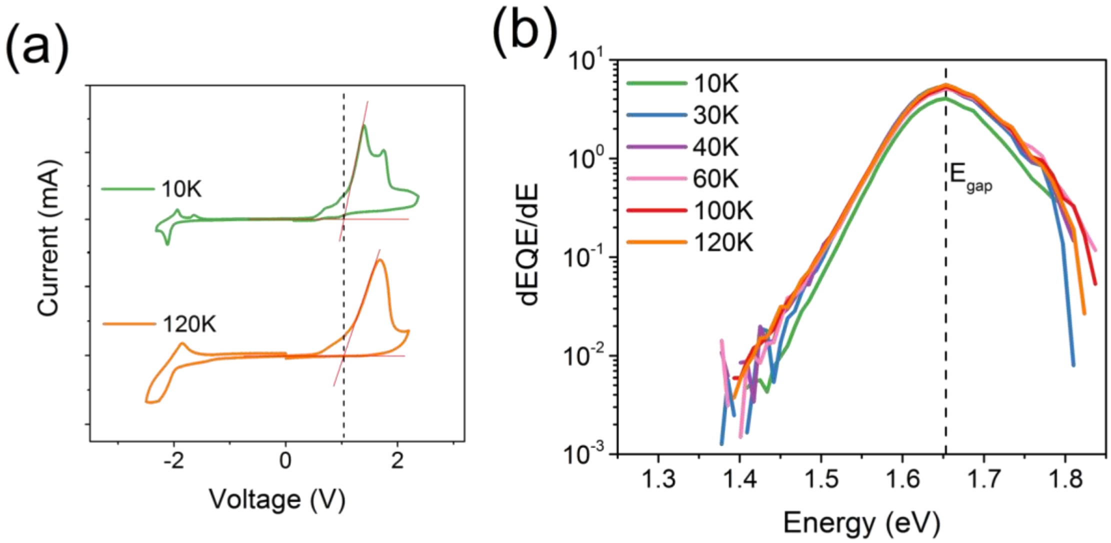

Figure S2.3. Methods of FTAZ bandgap measurement, **(a)** cyclic voltammetry and **(b)** EQE_{PV} derivative.

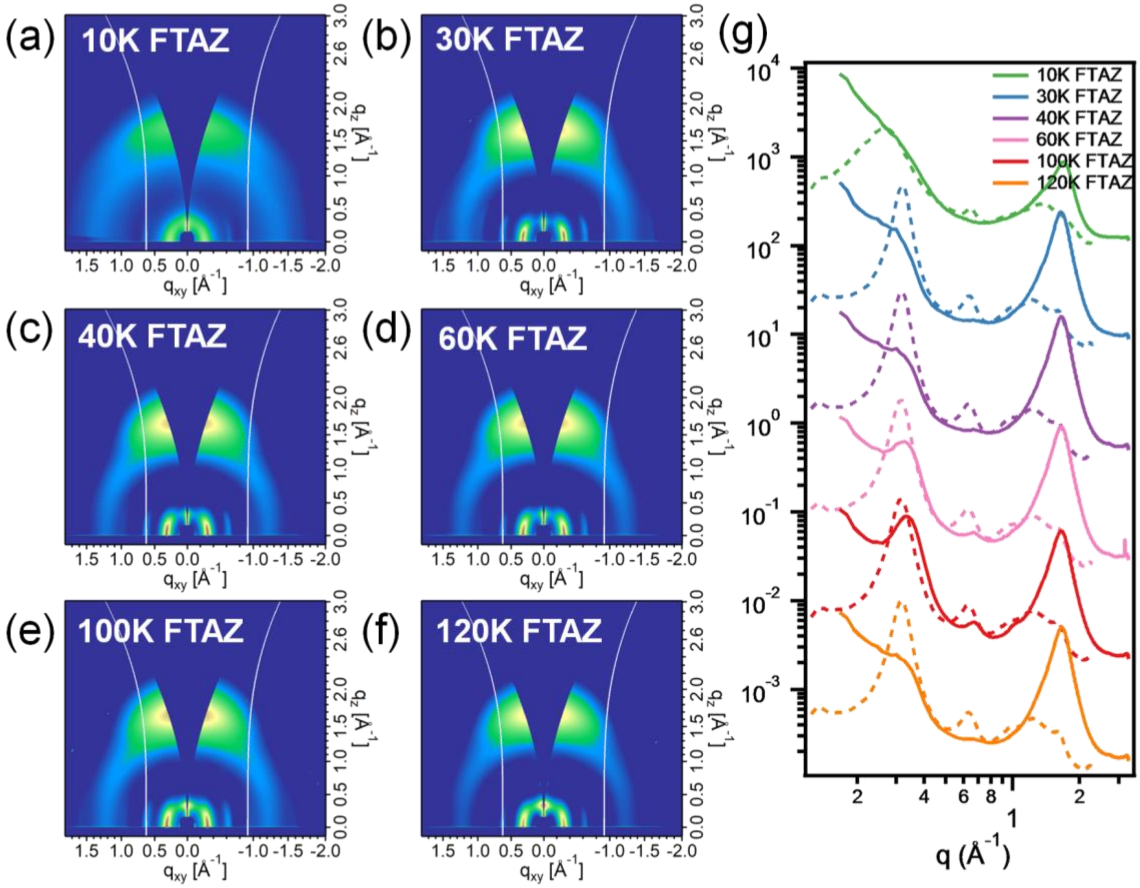

Figure S2.4. **(a)** - **(f)** 2D GIWAXS patterns and **(g)** line-cuts out-of-plane (solid) and in-plane (dashed) for neat FTAZ films with M_n of **(a)** 10, **(b)** 30, **(c)** 40, **(d)** 60, **(e)** 100, and **(f)** 120 kg/mol.

Table S2.1. Domain spacing and relative composition variations measured by RSoXS.

FTAZ	Peak Position (nm^{-1})	Long Period[a] (nm)	Thickness Normalized ISI	σ^b
10K	0.104	**60.4**	1.00	**1.00**
30K	0.188	**33.4**	0.82	**0.90**
40K	0.233	**27.0**	0.79	**0.89**
60K	0.272	**23.1**	0.79	**0.89**
100K	0.257	**24.4**	0.62	**0.79**
120K	0.292	**21.5**	0.42	**0.65**

[a] real-space domain spacing

[b] Lorentz-corrected and thickness normalized root-mean-square composition variation, which represents the average domain purity

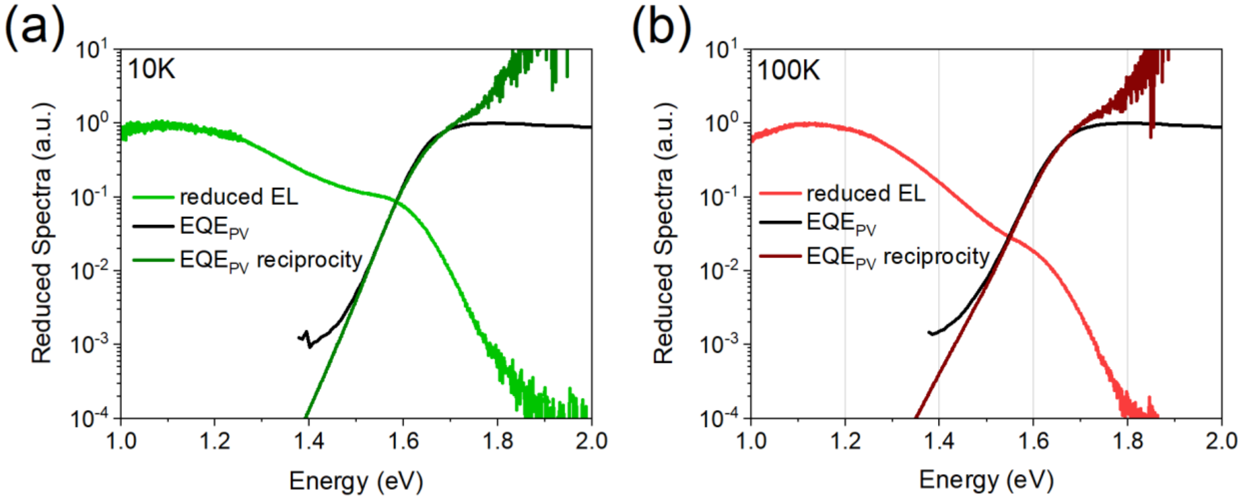

Figure S2.5. Reduced EQE_{PV} and EL spectra for determination of the charge transfer (CT) state, according to the work of Vandewal and coworkers. Unfortunately, the CT energy could not be determined due to overlap with ITIC singlet emission (shoulder at ~1.6 eV). EQE_{PV} reciprocity is the extension of the spectrum from the calculation of EL/blackbody spectrum.

APPENDIX B: SUPPORTING INFORMATION FOR CHAPTER 3

Device Fabrication

Patterned 12 mm × 12 mm ITO substrates were sonicated sequentially in deionized water, acetone, and isopropyl alcohol for 15 minutes each. The substrates were dried under a stream of nitrogen then treated with UV/Ozone for 15 minutes. For conventional devices, PEDOT:PSS Al4083 (purchased from Heraeus) was filtered through a 0.45 µm PVDF syringe filter and cast on the cleaned substrated at 4000 RPM for 1 minute. The substrates were then baked in air at 150 °C for 30 minutes, transferred, then storred under N_2 until use. For inverted devices, Zinc oxide (ZnO) precursor solution was prepared from 1 g zinc acetate dihydrate and 0.28 g ethanolamine in 10 mL 2-methoxyethanol. The solution was stirred overnight, then filtered through a 0.2 µm PTFE syringe filter. The solution was spin-cast onto the clean ITO for 30 seconds at 4000 RPM then baked in air at 155 °C for 20 minutes. The substrates were transferred and stored in a nitrogen-filled glovebox until use. P3HT (Rieke Metals, MW 49k) and $PC_{61}BM$ (Nano-C) solutions were prepared with a 1:1 donor:acceptor ratio in CF, CB, or oDCB with a total mass concentration of 28, 36, or 40 mg/mL, respectively, and stirred overnight at 40, 60, or 100 °C, respectively, in a nitrogen-filled glovebox. Any additives were dissolved in the corresponding solvent and added to the active layer solution 30 minutes prior to spin-coating. Afterwards, the solution was spin-cast on the prepared substrates for 1 minute at 1500 RPM then annealed at 110 ℃ for 10 minutes. The devices were finished by evaporating 50 nm Ca (conventional) or 10 nm MoO_3 (inverted) and then 70 nm Al through a shadow mask to produce 6.8 mm^2 devices. The devices were tested under AM 1.5G irradiation calibrated with an NREL-certified standard Si solar cell. J-V characteristics were measured with a Keithley 2400 digital source meter.

Morphology

Grazing Incidence Wide Angle X-ray Scattering. GIWAXS was measured at beamline 7.3.3 of Advanced Light Source (ALS) at Lawrence Berkeley National Laboratory.[204] The 10 keV X-ray beam was incident at a grazing angle of 0.13°, which maximized the scattering intensity from the samples and minimized the scattering intensity from the substrate. The scattered intensity was detected with a Dectris Pilatus 1M photon counting detector.

Resonant Soft X-ray Scattering. R-SoXS was measured at beamline 11.0.1.2 of the ALS[205] on blend films. Data were acquired at the photon energy of 283.6 eV where the contrast between polymer and fullerene is relatively high enough for these materials, yet does not lead to beam damage or background fluorescence.

Surface Spectroscopy

XPS and UPS data was collected on a Kratos Supra+ instrument. XPS data utilized a monochromatic Al Ka source, and pass energies of 80 eV and 20 eV were used for survey and high resolution spectra, respectively. A charge neutralizer was used when needed, and all spectra were corrected to the C 1s peak at 284.6 eV. UPS spectra were collected with He I illumination at 21.2 eV and a pass energy of 5 eV.

This work was performed in part at the Chapel Hill Analytical and Nanofabrication Laboratory, CHANL, a member of the North Carolina Research Triangle Nanotechnology Network, RTNN, which is supported by the National Science Foundation, Grant ECCS-2025064, as part of the National Nanotechnology Coordinated Infrastructure, NNCI. A portion of this work was performed using XPS and UPS instrumentation supported by the Center for Hybrid Approaches in Solar Energy to Liquid Fuels (CHASE), an Energy Innovation Hub funded by the

U.S. Department of Energy, Office of Science, Office of Basic Energy Sciences under Award Number DE-SC0021173.

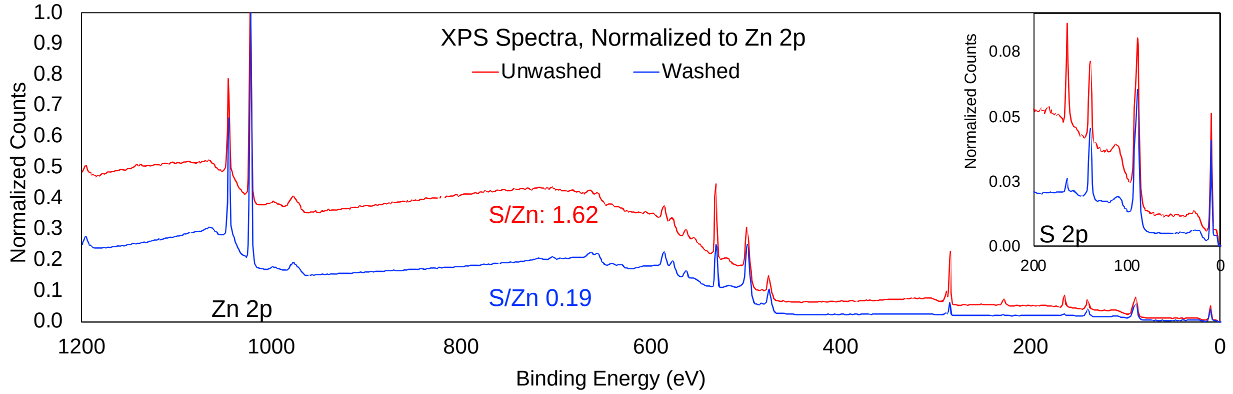

Figure S3.1. X-Ray Photoelectron Spectroscopy (XPS) of washed and unwashed ZnO/3TZA films.

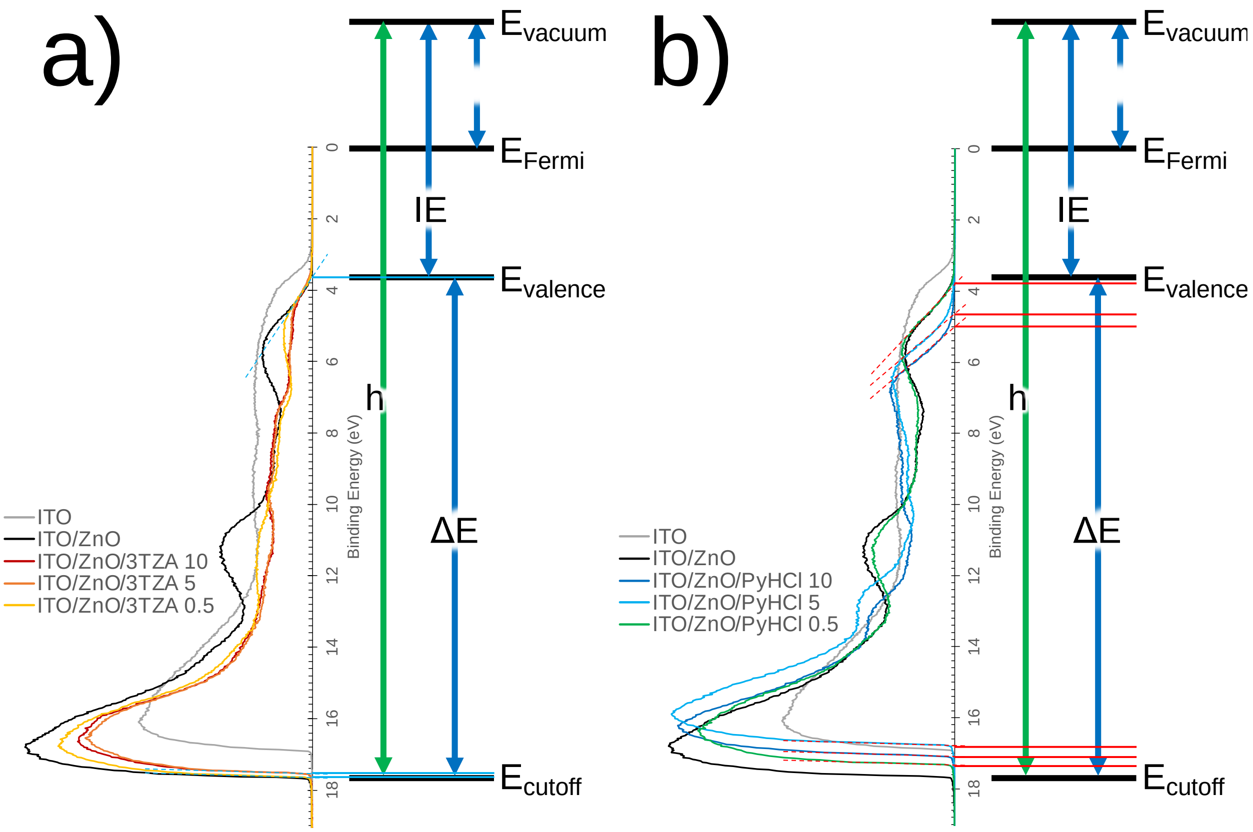

Figure S3.2. UPS spectra of ITO/ZnO with a thin film of **a)** 3TZA or **b)** PyHCl cast at 10, 5, and 0.5 mg/mL.

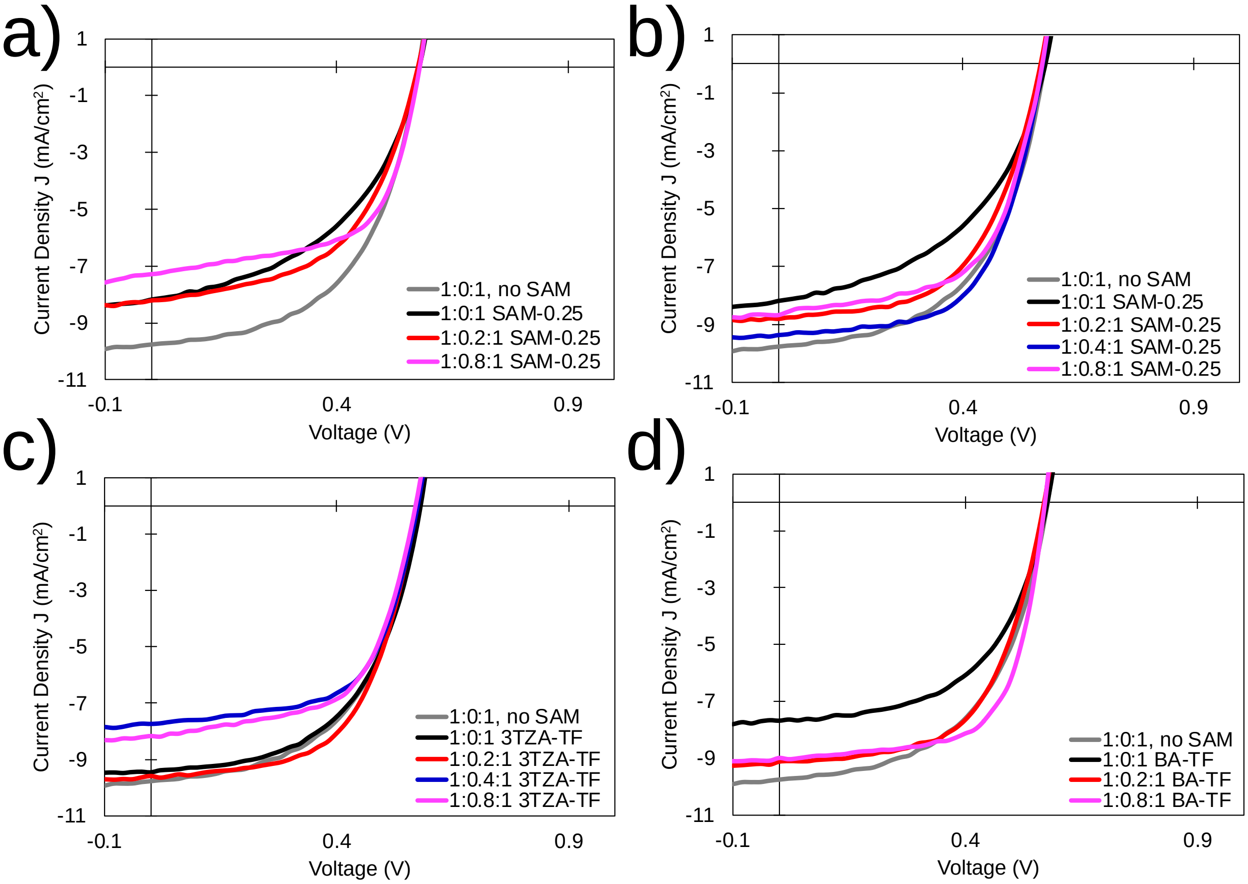

Figure S3.3. PV properties of P3HT:3TZA or BA:PC$_{61}$BM blend devices. "SAM-0.25" is IC-SAM, cast from a 0.25 mg/mL solution. 3TZA-TF and BA-TF are thin film of 3TZA or BA cast from 0.25 mg/mL onto ZnO. Shown are the J-V curves of **a)** P3HT:3TZA:PC$_{61}$BM on IC-SAM treated ZnO, **b)** P3HT:BA:PC$_{61}$BM on IC-SAM treated ZnO, **c)** P3HT:3TZA:PC$_{61}$BM on 3TZA-TF treated ZnO, and **d)** P3HT:BA:PC$_{61}$BM on BA-TF treated ZnO.

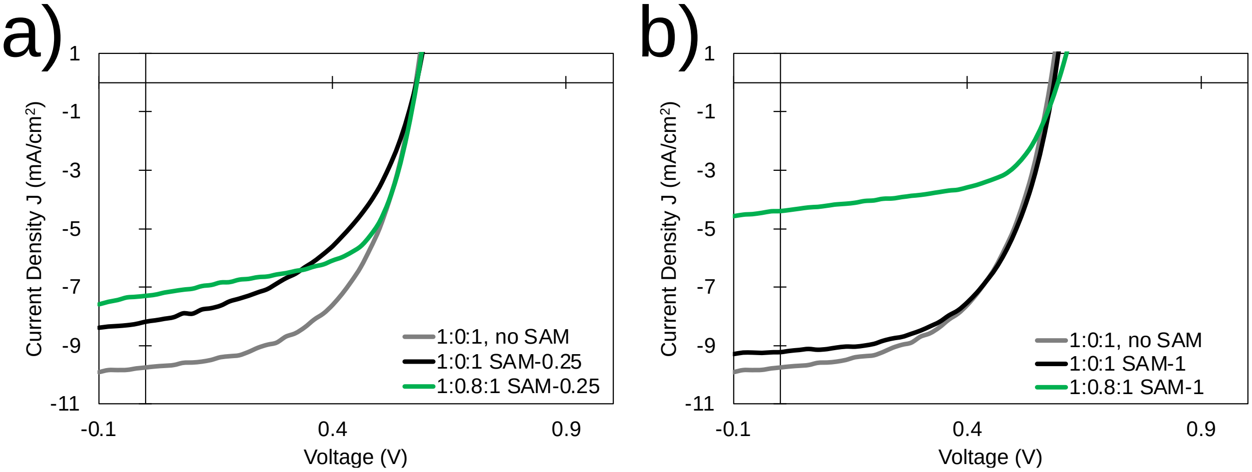

Figure S3.4. J-V characteristics of P3HT:3TZA:PC61BM solar cells with IC-SAM cast at **a)** 0.25 mg/mL and **b)** 1 mg/mL.

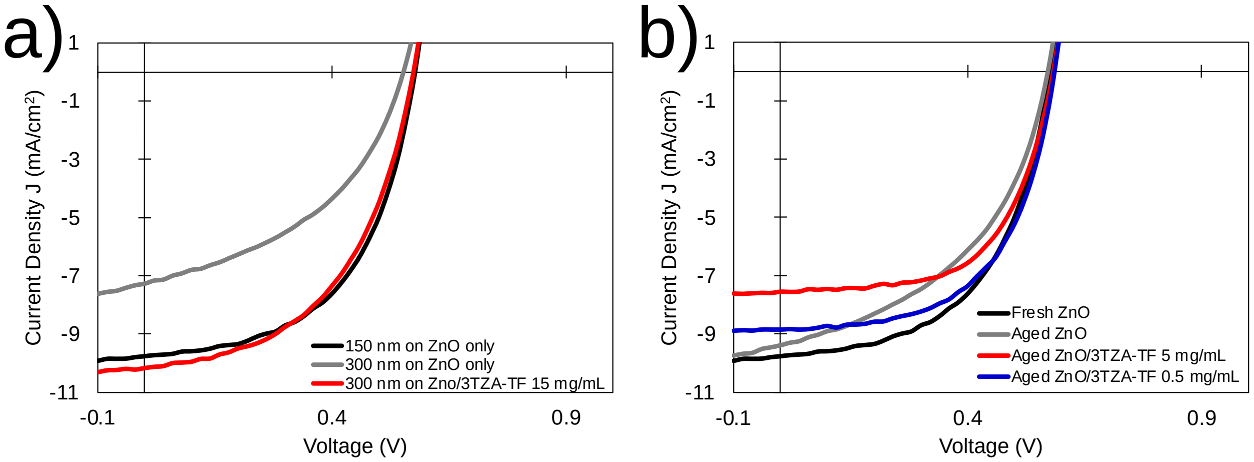

Figure S3.5. Recovery in **a)** thick and **b)** aged devices using 3TZA thin films cast onto ZnO.

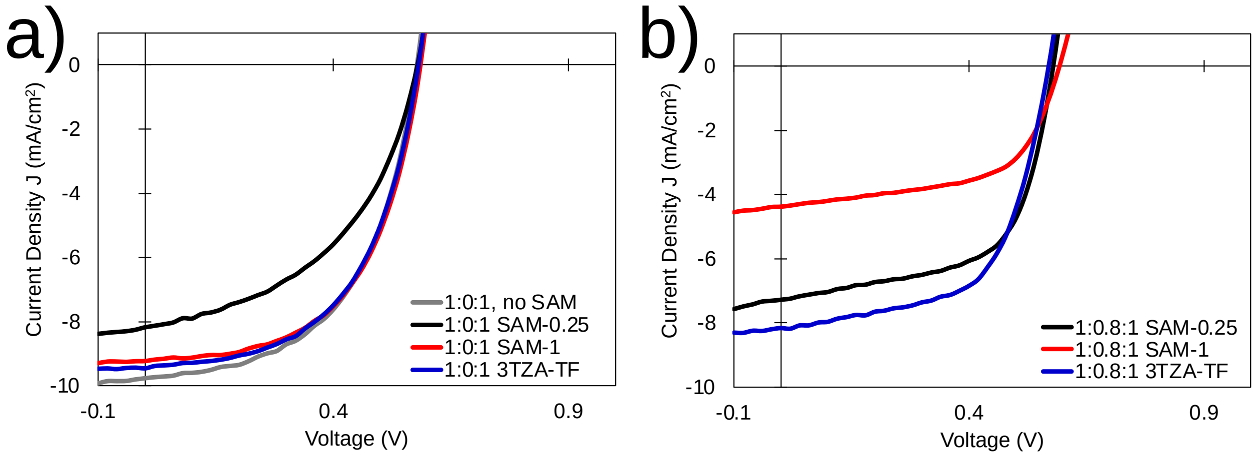

Figure S3.6. The impact of IC-SAM at 0.25 mg/mL and 1 mg/L and 3TZA 0.25 mg/mL passivation layers a) without and b) with 3TZA (80 wt% relative to P3HT) present in the blend.

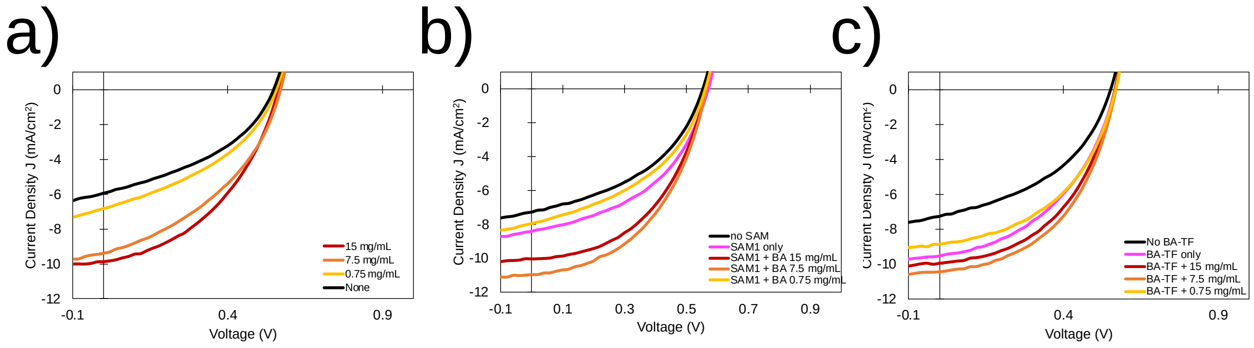

Figure S3.7. J-V curves of devices with architecture ITO/ZnO/x/BA/P3HT:PCBM/MoOx/Al, where x is **a)** absent, **b)** IC-SAM at 0.25 mg/mL (denoted SAM1), or **c)** 15 mg/mL BA. The BA layer following layer x is spin cast at 15, 7.5, and 0.75 mg/mL.

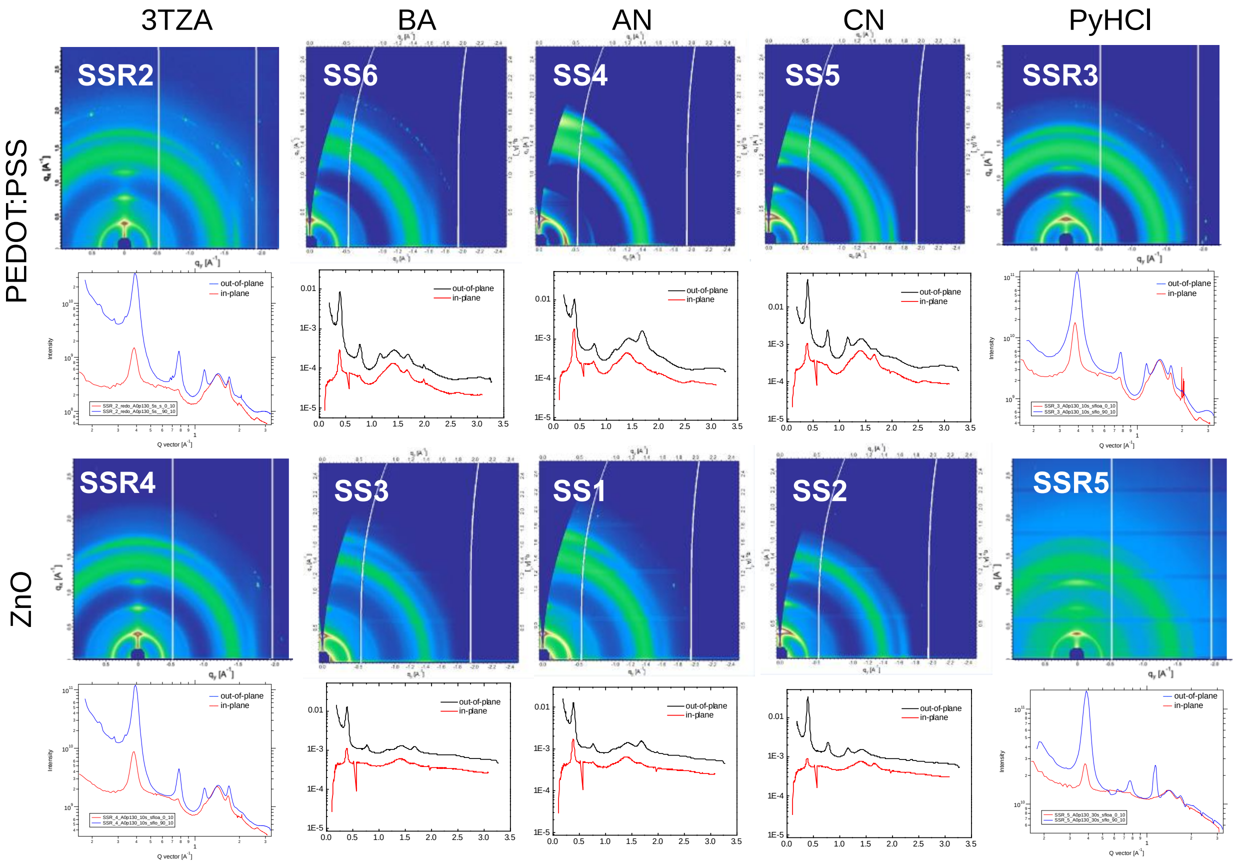

Figure S3.8. Grazing incidence X-Ray Spectroscopy (GIWAXS) scattering data and in-/out-of-plane linecuts of additives on PEDOT:PSS and ZnO.

Table S3.1. Morphological properties extracted from GIWAXS and RSoXS. IL is the interlayer, P:P is PEDOT:PSS, AF is additive fraction, TA is thermal anneal (110 °C for 10 min), OOP/IP are out-of- and in-plane, and LP is long period.

Add.	IL	AF	TA	(100) OOP		(200) OOP		(300) OOP		PCBM		(010) OOP		(100) IP		(010) IP		LP (nm)
				q (Å^{-1})	d (Å)	q (Å-1)	d (Å)	q (Å-1)	d (Å)	q (Å-1)	d (Å)	q (Å-1)	d (Å)	q (Å-1)	d (Å)	q (Å^{-1})	d (Å)	
none	none	0.0	N	0.37	16.89	0.78	8.08	--	--	1.44	4.37	1.66	3.78	0.40	15.71	--	--	--
			Y	0.39	16.24	0.78	8.09	1.15	5.44	1.43	4.38	1.69	3.72	0.38	16.55	1.66	3.79	34
3TZA	none	0.2	Y	0.39	16.24	0.76	8.22	1.15	5.44	1.43	4.40	1.69	3.72	0.40	15.71	1.62	3.88	
		0.8	Y	0.39	16.28	0.77	8.18	1.15	5.47	1.43	4.39	1.69	3.72	0.40	15.71	1.63	3.85	33
	P:P	0.8	Y	0.39	15.97	0.78	8.09	1.15	5.44	1.43	4.38	1.70	3.70	0.39	16.29	1.68	3.75	
	ZnO	0.8	Y	0.39	15.97	0.78	8.09	1.15	5.44	1.44	4.36	1.69	3.71	0.39	16.29	1.68	3.75	
BA	none	0.2	Y	0.39	16.24	0.78	8.09	1.15	5.44	1.43	4.38	1.70	3.70	0.39	16.29	1.66	3.79	
		0.8	Y	0.39	15.97	0.78	8.09	1.15	5.44	1.43	4.40	1.69	3.71	0.38	16.55	1.66	3.78	100
	P:P	0.8	Y	0.39	16.03	0.77	8.14	1.15	5.45	1.42	4.42	1.69	3.72	0.40	15.71	1.64	3.83	
	ZnO	0.8	Y	0.39	16.15	0.77	8.15	1.16	5.44	1.42	4.42	1.69	3.73	0.40	15.71	1.63	3.85	
AN	none	0.8	N	0.40	15.91	0.78	8.08	1.17	5.39	1.42	4.43	1.67	3.76	0.40	15.71	1.65	3.81	39
		0.8	Y	0.39	15.95	0.78	8.11	1.16	5.43	1.42	4.43	1.69	3.72	0.40	15.71	1.65	3.81	66
	P:P	0.8	Y	0.39	16.19	0.77	8.16	1.17	5.39	1.43	4.41	1.69	3.72	0.40	15.71	1.62	3.88	
	ZnO	0.8	Y	0.39	16.19	0.77	8.19	--	--	1.42	4.41	1.69	3.72	0.40	15.71	1.63	3.85	
CN	none	0.8	Y	0.39	15.95	0.78	8.11	1.16	5.43	1.42	4.43	1.69	3.72	0.40	15.71	1.63	3.85	34
	P:P	0.8	Y	0.39	15.95	0.78	8.11	1.16	5.43	1.41	4.46	1.69	3.72	0.40	15.71	1.63	3.85	
	ZnO	0.8	Y	0.39	15.99	0.78	8.10	1.16	5.43	1.42	4.44	--	--	0.40	15.71	1.65	3.81	
PyHCl	none	0.2	Y	0.39	16.24	0.76	8.22	1.15	5.44	1.42	4.42	1.68	3.74	0.38	16.55	1.66	3.79	
		0.8	Y	0.39	16.28	0.77	8.20	1.15	5.48	1.42	4.43	1.68	3.74	0.38	16.55	1.65	3.82	40
	P:P	0.8	Y	0.39	15.97	0.77	8.15	1.15	5.44	1.42	4.42	1.68	3.74	0.38	16.55	1.68	3.75	

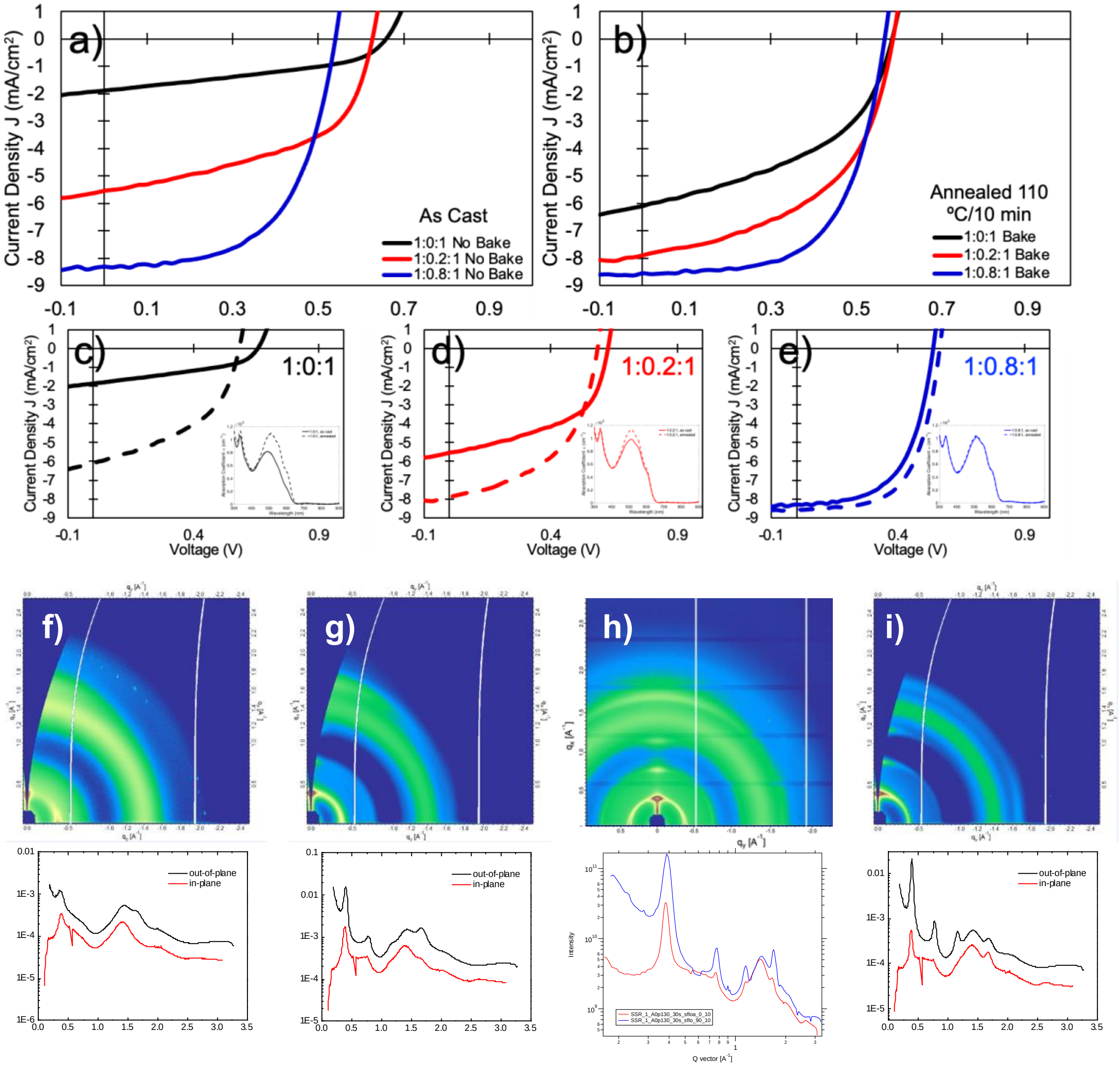

Figure S3.9. J-V characteristics of P3HT:AN:PC$_{61}$BM devices **a)** as cast and **b)** after thermal annealing at 110 °C for 10 minutes. The bottom row compares the J-V characteristics of as cast (solid) and annealed (dashed) at **c)** 0 wt%, **d)** 20 wt%, and **e)** 80 wt% AN. The inset of each is the corresponding UV-Vis spectra before and after thermal annealing. The GIWAXS of P3HT:AN:PC$_{61}$BM as cast with **f)** 0 wt% and **g)** 80 wt% AN are markedly different from their annealed counterparts **h)** and **i)**, respectively.

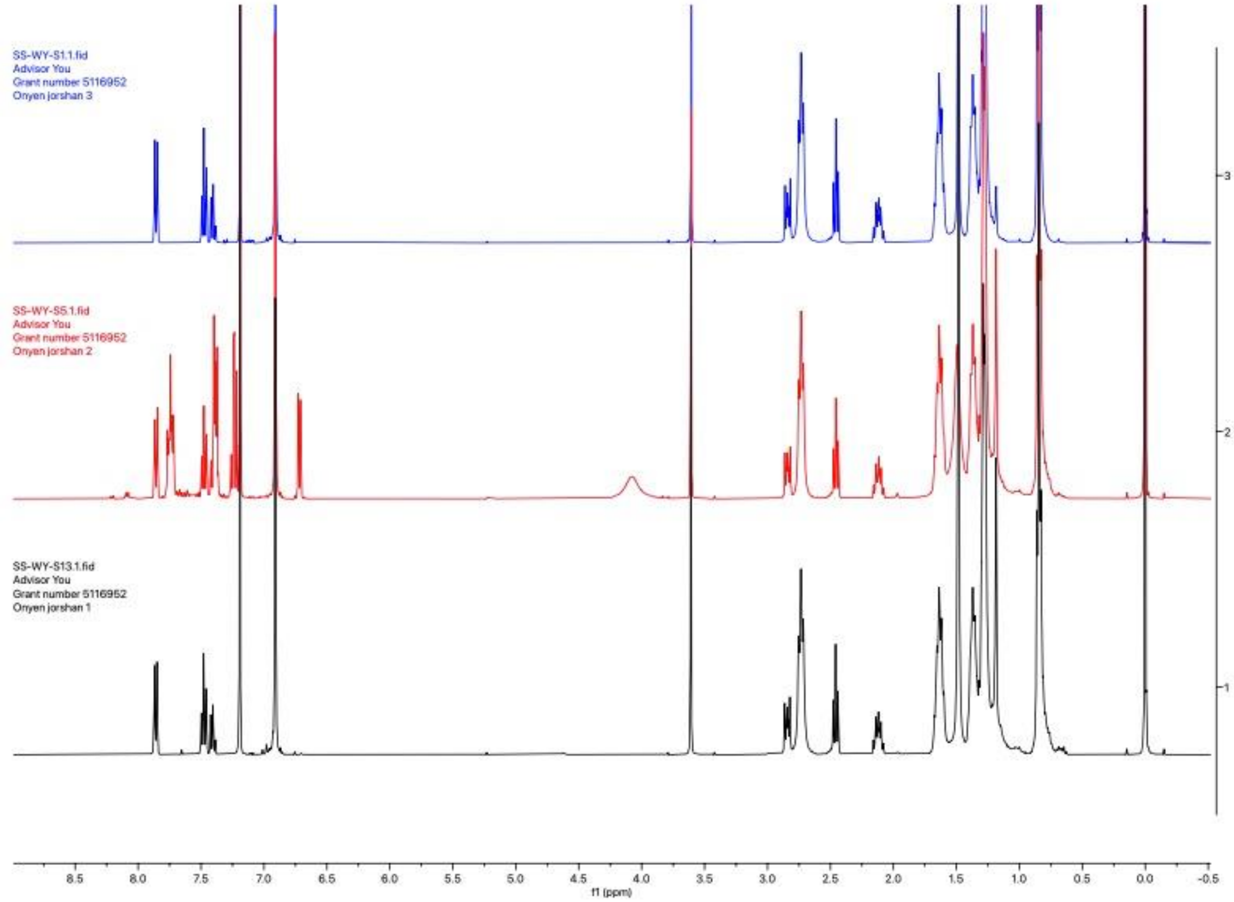

Figure S3.10. NMR spectra of P3HT:AN:$PC_{61}BM$ before addition (top), after addition (middle), and after all processing (bottom).

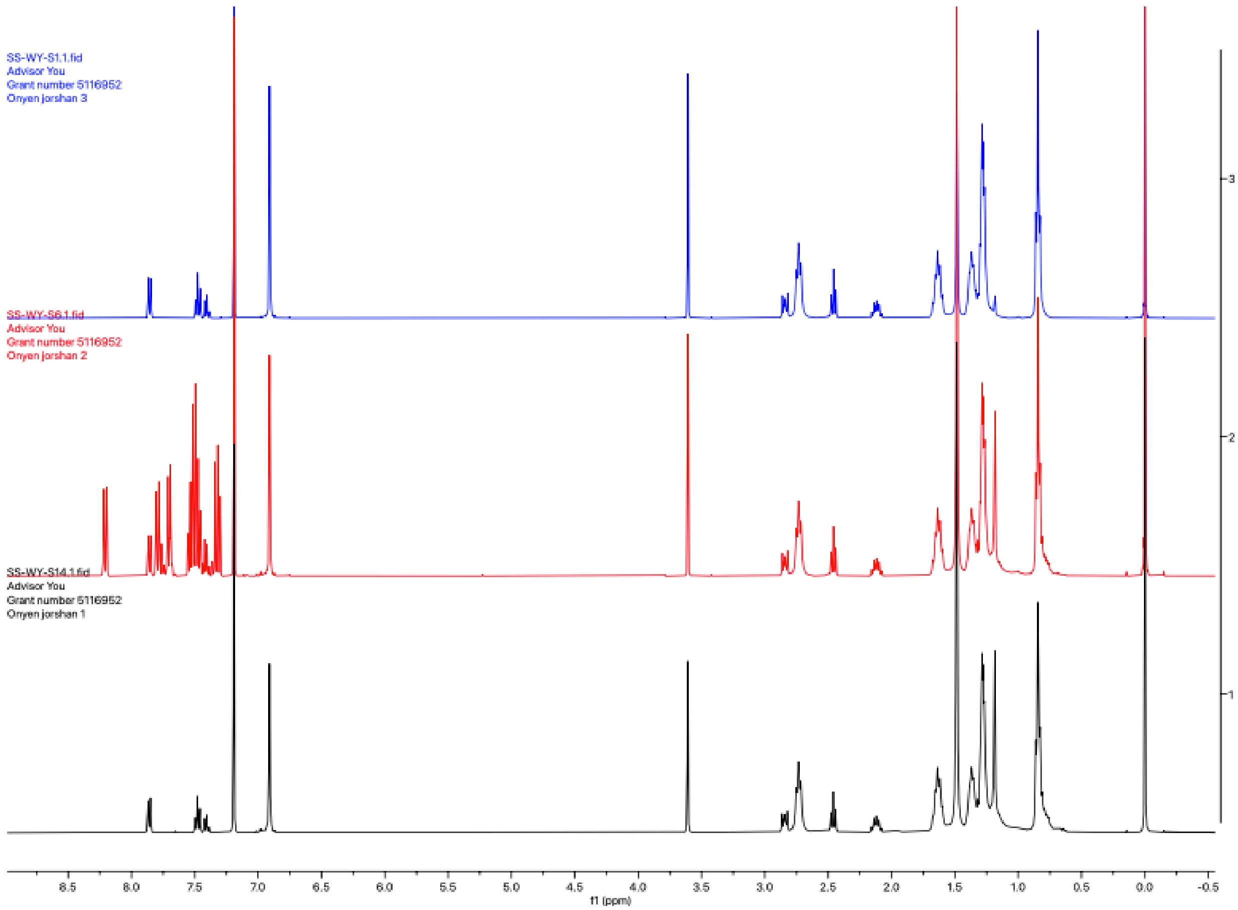

Figure S3.11. NMR spectra of P3HT:CN:PC$_{61}$BM before addition (top), after addition (middle), and after all processing (bottom).

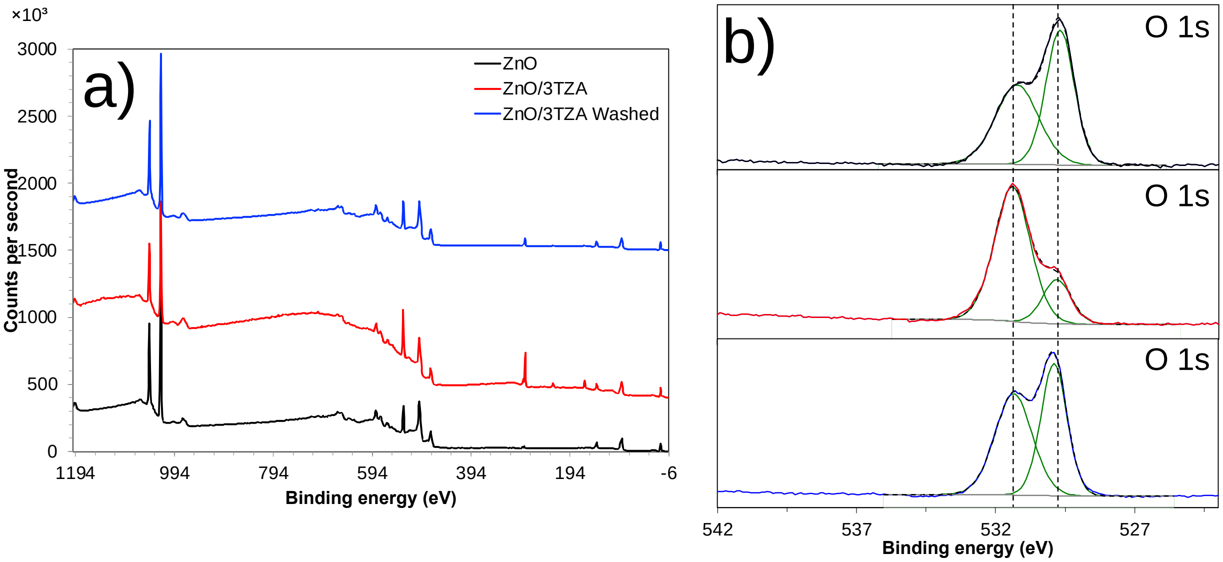

Figure S3.12. XPS **a)** survey scans and **b)** S 2p spectra of PEDOT:PSS and PEDOT:PSS/AN surfaces.

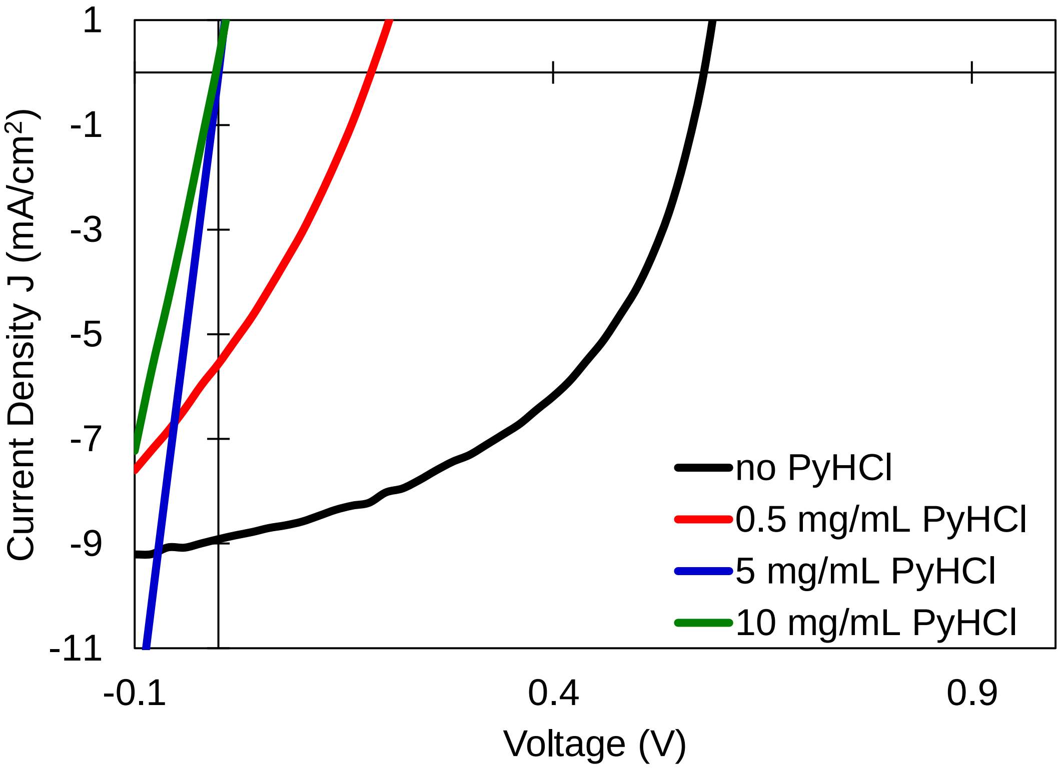

Figure S3.13. J-V curves for ITO/ZnO/PyHCl/P3HT:PC$_{61}$BM/MoOx/Al devices using PyHCl of various concentrations.

Table S3.2. Estimated shunt and series resistance for ITO/ZnO/PyHCl/P3HT:PC$_{61}$BM/MoOx/Al devices using PyHCl of various concentrations. The "Meas." column contains the contact and series resistance for ITO/ZnO/PyHCl/MoOx/Al devices.

PyHCl conc. (mg/mL)	Estimated from J-V Curve		Meas. (no active layer)
	R_{sh} (kΩ)	R_s (kΩ)	R (Ω)
0	3.95	0.20	9.29
0.5	0.69	0.19	8.61
5	0.11	0.11	16.99
10	0.18	0.18	15.24

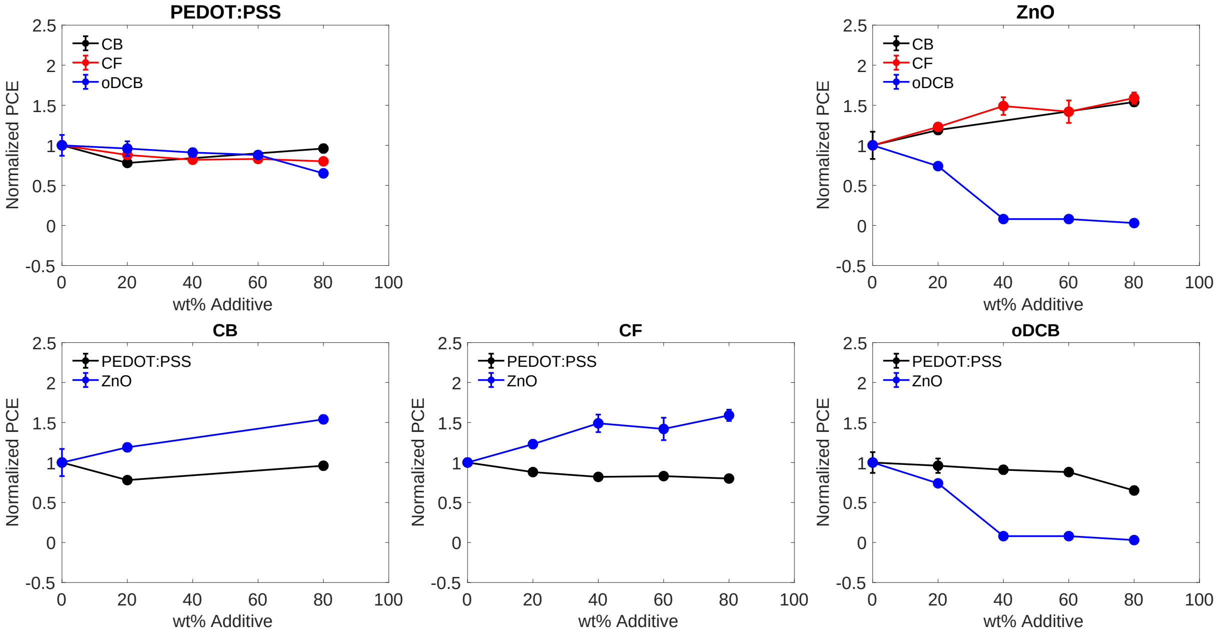

Figure S3.14. Normalized PCE for P3HT:3TZA:PC$_{61}$BM plotted by interlayer (top row) or by solvent (bottom row).

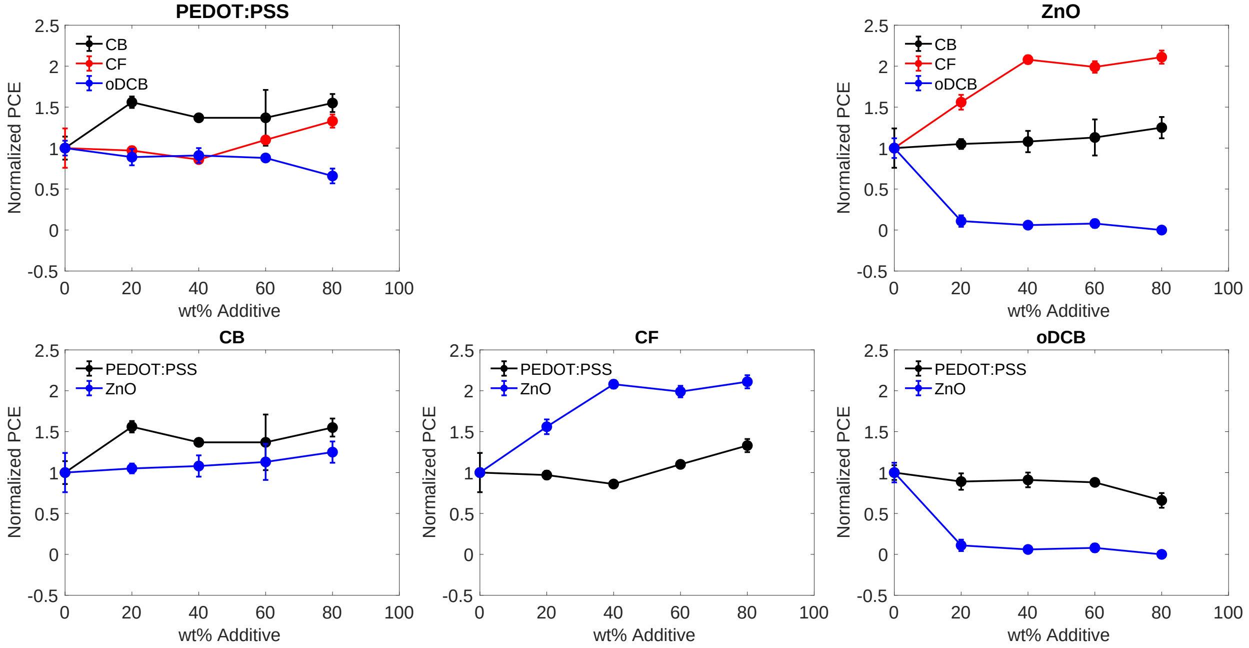

Figure S3.15. Normalized PCE for P3HT:BA:PC$_{61}$BM plotted by interlayer (top row) or by solvent (bottom row).

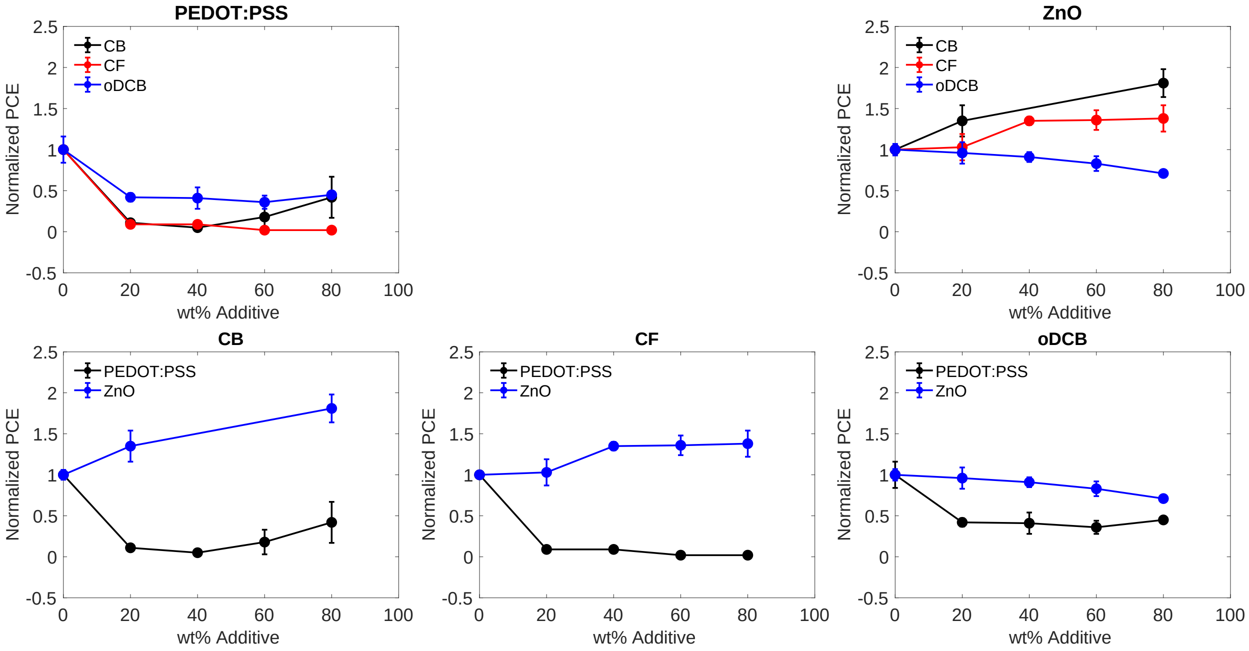

Figure S3.16. Normalized PCE for P3HT:AN:PC$_{61}$BM plotted by interlayer (top row) or by solvent (bottom row).

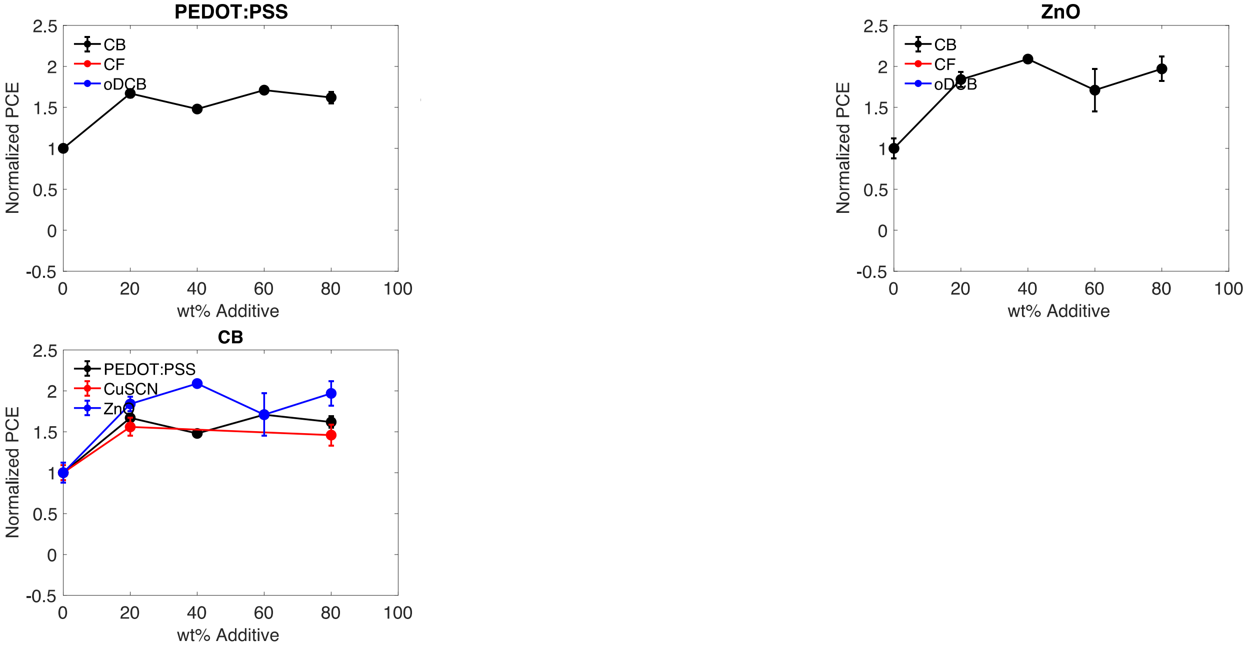

Figure S3.17. Normalized PCE for P3HT:CN:PC$_{61}$BM plotted by interlayer (top row) or by solvent (bottom row).

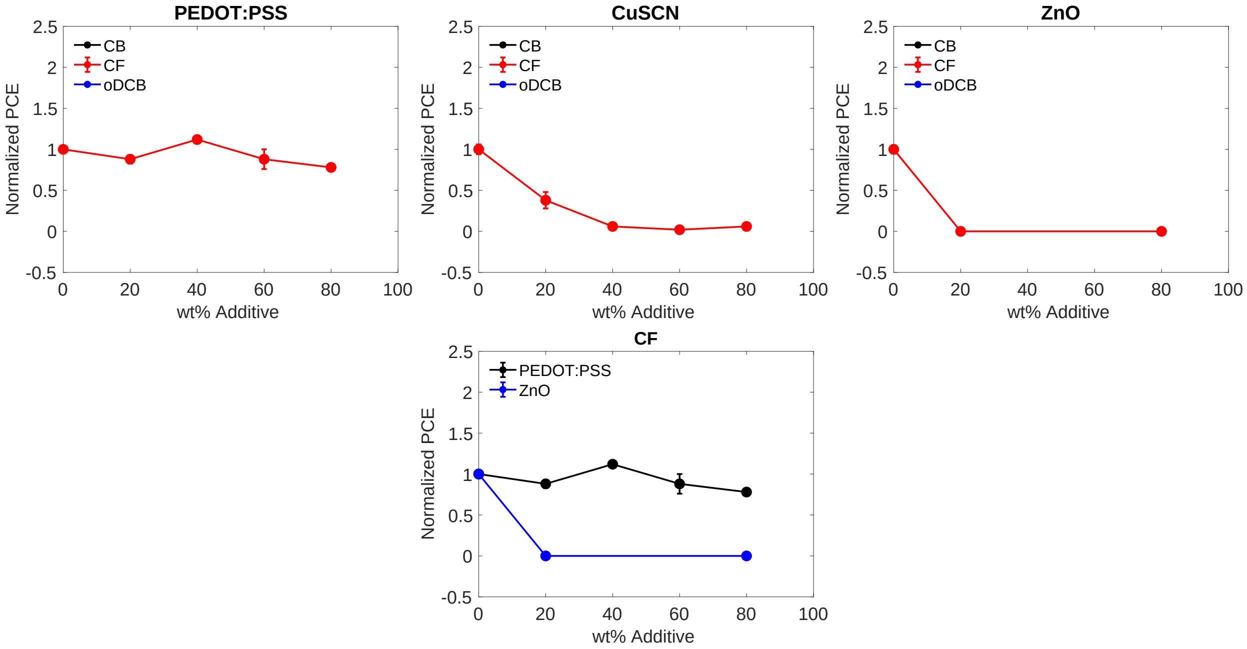

Figure S3.18. Normalized PCE for P3HT:PyHCl:PC$_{61}$BM plotted by interlayer (top row) or by solvent (bottom row).

Figure S3.19. Crystallites observed on the surface of P3HT:3TZA:PC$_{61}$BM 1:0.8:1 films cast from oDCB.

APPENDIX C: SUPPORTING INFORMATION FOR CHAPTER 4

Device Fabrication

Patterned 12 mm × 12 mm ITO substrates were sonicated sequentially in deionized water, acetone, and isopropyl alcohol for 15 minutes each. The substrates were dried under a stream of nitrogen then treated with UV/Ozone for 15 minutes. For conventional devices, PEDOT:PSS Al4083 (purchased from Heraeus) was filtered through a 0.45 µm PVDF syringe filter and cast on the cleaned substrated at 4000 RPM for 1 minute. The substrates were then baked in air at 150 °C for 30 minutes, transferred, then storred under N_2 until use. Donor:$PC_{61}BM$ solutions were prepared with a 1:1 donor:acceptor ratio in CB with a total mass concentration of 36 mg/mL and left to stir overnight at 100 °C in a nitrogen-filled glovebox. The solution was spin-cast on the prepared substrates for 1 minute at 1500 RPM then annealed at 110 °C for 10 minutes. Samples for thermal cleavage were additionally annealed for 30 minutes at 200 °C. The devices were finished by evaporating 50 nm Ca and 70 nm Al through a shadow mask to produce 6.8 mm^2 devices. The devices were tested under AM 1.5G irradiation calibrated with an NREL-certified standard Si solar cell. J-V characteristics were measured with a Keithley 2400 digital source meter.

Mobility Measurements.

Patterned 12 mm × 12 mm ITO substrates were sonicated sequentially in deionized water, acetone, and isopropyl alcohol for 15 minutes each. The substrates were dried under a stream of nitrogen then treated with UV/Ozone for 15 minutes. Hole-only devices were fabricated with the architecture ITO/PEDOT:PSS/Donor/MoOx/Al. The PEDOT:PSS and top electrode conditions are the same as those used for the devices described in the previous section. Donor material was dissolved in CB at a concentration of 25 mg/mL and left to stir overnight at 60 °C. Devices were cast at various thicknesses by varying the spin speed. For thermally-cleaved devices, the devices were annealed at 150 °C overnight in the dark under N_2. Mobility was then measured using the space charge limited current (SCLC) method. Current was extracted as a function of bias under 1-sun and dark conditions using a Keithley 2400 digital source meter. The voltage data was corrected for built-in voltage and parasitic resistances. The corrected J-V data was plotted and fit the SCLC region to the Mott-Gurney law,

$$J = \frac{9}{8}\varepsilon_0 \varepsilon_r \mu \frac{V^2}{d^3}, \tag{S4.1}$$

Where J is the current density, ε_r is the dielectric constant (typically 2-5 for organic semiconductors),[206] ε_0 is the permittivity of free space, μ is the charge carrier mobility, V is the voltage, and d is the thickness of the film.

Morphology

Grazing Incidence Wide Angle X-ray Scattering. GIWAXS was measured at beamline 7.3.3 of Advanced Light Source (ALS) at Lawrence Berkeley National Laboratory.[204] The 10 keV X-ray beam was incident at a grazing angle of 0.13°, which maximized the scattering intensity from the samples and minimized the scattering intensity from the substrate. The scattered intensity was detected with a Dectris Pilatus 1M photon counting detector.

Resonant Soft X-ray Scattering. R-SoXS was measured at beamline 11.0.1.2 of the ALS[205] on blend films. Data were acquired at the photon energy of 283.6 eV where the contrast between polymer and fullerene is relatively high enough for these materials, yet does not lead to beam damage or background fluorescence.

Table S4.1. SCLC mobility the RP-TCS series before and after thermal cleavage.

Donor Polymer	Mobility (cm^2/Vs)	
	110 °C, 10 minutes	150 °C, 24 hours
P3HT	$(9.18 \pm 5.44) \times 10^{-4}$	$(6.67 \pm 2.67) \times 10^{-4}$
RP-TCS20	$(3.66 \pm 2.41) \times 10^{-5}$	$(9.28 \pm 1.11) \times 10^{-5}$
RP-TSC40	$(4.34 \pm 1.04) \times 10^{-8}$	$(6.87 \pm 1.97) \times 10^{-5}$
RP-TSC60	4.11×10^{-7}	$(5.85 \pm 4.14) \times 10^{-5}$
RP-TSC80	$(5.36 \pm 0.21) \times 10^{-8}$	$(6.97 \pm 1.58) \times 10^{-5}$
P3ET	$(1.76 \pm 0.01) \times 10^{-6}$	$(1.53 \pm 0.29) \times 10^{-4}$

Table S4.2. Peak locations in reciprocal-space with corresponding lengths in real-space. OOP is out-of-plane and IP is in-plane.

Donor	**Anneal Condition**	**Age (Day)**	**OOP (100)**		**OOP (200)**		**OOP (300)**		**OOP (010)**		**IP (100)**		**IP (010)**	
			q (Å^{-1})	**d (Å)**	**q (Å^{-1})**	**d (Å)**	**q (Å^{-1})**	**d (Å)**	**q (Å^{-1})**	**d (Å)**	**q (Å^{-1})**	**d (Å)**	**q (Å^{-1})**	**d (Å)**
P3HT	110 °C/10 min	0	0.40	15.71	0.78	8.06	1.16	5.42	1.68	3.74	0.38	16.53	1.60	3.93
		1	0.40	15.71	0.80	7.85	1.2	5.24	1.65	3.81	0.38	16.53	1.60	3.93
		7	0.40	15.71	0.80	7.85	1.2	5.24	1.70	3.70	0.38	16.53	1.65	3.81
P3ET	110 °C/10 min	0	0.45	13.96	--	--	--	--	--	--	0.45	13.96	--	--
	200 °C/30 min	0	--	--	--	--	--	--	--	--	--	--	--	--
		1	0.40	15.71	0.78	8.06	1.18	5.32	1.65	3.81	0.50	12.57	1.65	3.81
		7	0.41	15.32	0.8	7.85	1.25	5.03	1.55	4.05	0.40	15.71	1.45	4.33
TCS40	110 °C/10 min	0	0.37	16.98	0.79	7.95	1.10	5.71	--	--	0.50	12.57	--	--
	200 °C/30 min	0	--	--	--	--	--	--	--	--	--	--	--	--
		1	--	--	--	--	--	--	--	--	--	--	--	--
TCS60	110 °C/10 min	0	--	--	--	--	--	--	--	--	--	--	--	--
	200 °C/30 min	0	--	--	--	--	--	--	--	--	--	--	--	--
		1	--	--	--	--	--	--	--	--	--	--	--	--
		7		--	--	--	--	--	--	--	--	--	--	--

Table S4.3. Photovoltaic properties of OPVs with the architecture ITO/PEDOT:PSS/donor: $PC_{61}BM$/Ca/Al with a device area of 0.13 mm^2. TCS Frac indicates the fraction of monomer in the donor incorporating TCS, i.e. TCS Frac of 0 is P3HT while TCS Frac 0.6 is RP-TCS60.

TCS Frac	Anneal Condition	$J_{SC} \pm \sigma$ (mA/cm^2)	$V_{OC} \pm \sigma$ (V)	FF ± σ (%)	PCE ± σ (best) (%)
0	110 °C, 10 min	7.49 ± 1.08	0.57 ± 0.01	43.1% ± 3.9%	1.84% ± 0.41% (2.40%)
	200 °C, 30 min	8.20 ± 0.35	0.59 ± 0.00	54.4% ± 3.6%	2.65% ± 0.27% (2.97%)
0.2	110 °C, 10 min	1.58 ± 0.30	0.74 ± 0.01	49.2% ± 3.9%	0.58% ± 0.14% (0.70%)
	200 °C, 30 min	1.54 ± 0.05	0.89 ± 0.01	35.5% ± 0.1%	0.49% ± 0.02% (0.51%)
0.4	110 °C, 10 min	0.39 ± 0.03	0.85 ± 0.05	27.2% ± 1.0%	0.09% ± 0.01% (0.10%)
	200 °C, 30 min	3.59 ± 0.35	0.93 ± 0.01	39.4% ± 1.1%	1.32% ± 0.17% (1.48%)
0.6	110 °C, 10 min	0.08 ± 0.00	0.89 ± 0.05	27.0% ± 0.4%	0.02% ± 0.00% (0.02%)
	200 °C, 30 min	4.10 ± 0.35	0.95 ± 0.07	32.7% ± 3.6%	1.2% ± 0.20% (1.50%)
0.8	110 °C, 10 min	0.03 ± 0.00	0.87 ± 0.00	23.0% ± 0.1%	0.01% ± 0.00% (0.01%)
	200 °C, 30 min	2.94 ± 0.35	0.89 ± 0.06	31.0% ± 2.4%	0.81% ± 0.13% (0.96%)
1	110 °C, 10 min	0.01 ± 0.00	0.76 ± 0.03	28.2% ± 8.7%	0.00% ± 0.00% (0.00%)
	200 °C, 30 min	0.28 ± 0.01	0.77 ± 0.02	30.8% ± 0.5%	0.07% ± 0.00% (0.07%)

Table S4.4. Mesoscale morphological information extracted from RSoXS for the donor:$PC_{61}BM$ systems. Data was acquired at 286.3 eV.

Donor	Anneal Cond	Days at 150 °C	Long period (nm)[a]	RMS Comp. Variation[b]
P3HT	110 °C, 10 min	0	21.66	0.81
		1	33.75, 22.35, 17.63	--
	200 °C, 30 min	0	25.12	1
		1	88.50	--
RP-TCS40	110 °C, 10 min	0	41.86	0.64
	200 °C, 30 min	0	41.86	1
RP-TCS60	110 °C, 10 min	0	17.94	0.95
	200 °C, 30 min	0	17.44	1
		1	20.33	--
		7	26.29	--
P3ET	200 °C, 30 min	1	n.m.	--
		7	n.m.	--

[a] Center-to-center domain spacing. Multiple values indicate multiple domain sizes. n.m. indicates the value was not measurable. In this case, this is due to the q value being too, making the integrated spectra difficult to fit.

[b] Composition variations are referenced for a single material system. P3HT and P3ET RMS composition variation cannot be directly compared, for example.

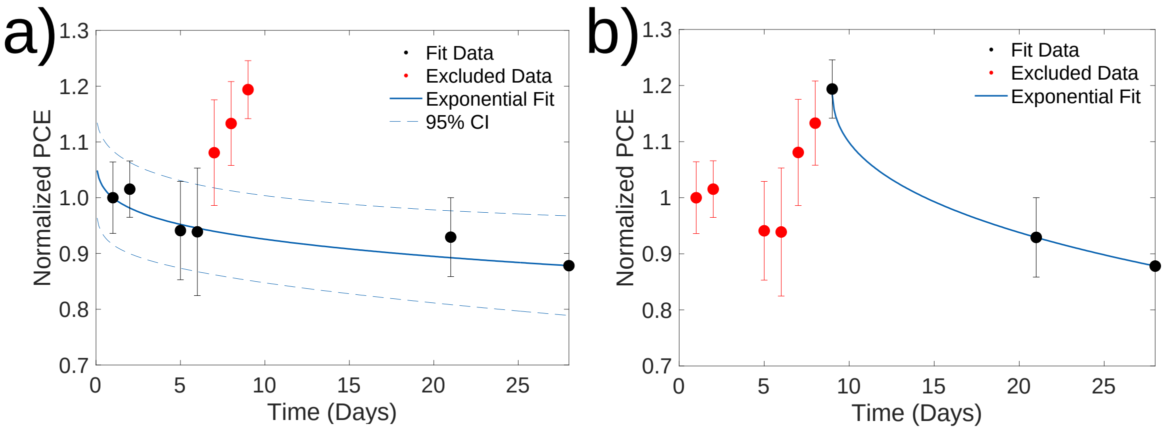

Figure S4.1. Extrapolated lifetime plots models fit to stretched exponentials $PCE_0\exp[(-t/a)^b]$, in the case where the recovery behavior **a)** is or **b)** is not a real feature. Here, t is time, PCE_0 is initial PCE, and a and b are fitting parameters. The fitting parameters for each are as follows: **a)** a = 9002, b = 0.2582 and **b)** a = 272.8, b = 0.4431.

REFERENCES

(1) Lewis, N. S.; Nocera, D. G. Powering the Planet: Chemical Challenges in Solar Energy Utilization. *Proc Natl Acad Sci U S A* **2006**, *103* (43), 15729–15735. https://doi.org/10.1073/pnas.0603395103.

(2) Kabir, E.; Kumar, P.; Kumar, S.; Adelodun, A. A.; Kim, K.-H. Solar Energy: Potential and Future Prospects. *Renewable and Sustainable Energy Reviews* **2018**, *82*, 894–900. https://doi.org/10.1016/J.RSER.2017.09.094.

(3) U.S. Department of Energy Energy Information Administration. *Primary Energy Production by Source*. Monthly Energy Review. https://www.eia.gov/totalenergy/data/monthly/pdf/sec1_5.pdf (accessed 2019-08-04).

(4) U.S. Energy Information Administration. *Total Energy Monthly Data*. Monthly Energy Review. https://www.eia.gov/totalenergy/data/monthly/ (accessed 2022-04-21).

(5) U.S. Energy Information Administration. *Electric Power Annual 2020*. Electric Power Annual. https://www.eia.gov/electricity/annual/ (accessed 2022-04-21).

(6) Facchetti, A. π-Conjugated Polymers for Organic Electronics and Photovoltaic Cell Applications. *Chemistry of Materials* **2011**, *23* (3), 733–758. https://doi.org/10.1021/cm102419z.

(7) Nelson, J. Polymer:Fullerene Bulk Heterojunction Solar Cells. *Materials Today* **2011**, *14* (10), 462–470. https://doi.org/10.1016/S1369-7021(11)70210-3.

(8) Søndergaard, R.; Hösel, M.; Angmo, D.; Larsen-Olsen, T. T.; Krebs, F. C. Roll-to-Roll Fabrication of Polymer Solar Cells. *Materials Today* **2012**, *15* (1–2), 36–49. https://doi.org/10.1016/S1369-7021(12)70019-6.

(9) Manceau, M.; Angmo, D.; Jørgensen, M.; Krebs, F. C. ITO-Free Flexible Polymer Solar Cells: From Small Model Devices to Roll-to-Roll Processed Large Modules. *Organic Electronics: physics, materials, applications* **2011**, *12* (4), 566–574. https://doi.org/10.1016/j.orgel.2011.01.009.

(10) Espinosa, N.; Hösel, M.; Angmo, D.; Krebs, F. C. Solar Cells with One-Day Energy Payback for the Factories of the Future. *Energy and Environmental Science* **2012**, *5* (1), 5117–5132. https://doi.org/10.1039/c1ee02728j.

(11) Kaltenbrunner, M.; White, M. S.; Głowacki, E. D.; Sekitani, T.; Someya, T.; Sariciftci, N. S.; Bauer, S. Ultrathin and Lightweight Organic Solar Cells with High Flexibility. *Nature Communications* **2012**, *3*. https://doi.org/10.1038/ncomms1772.

(12) Lipomi, D. J. Organic Photovoltaics: Focus on Its Strengths. *Joule* **2017**. https://doi.org/10.1016/j.joule.2017.12.011.

(13) Søndergaard, R. R.; Espinosa, N.; Jørgensen, M.; Krebs, F. C. Efficient Decommissioning and Recycling of Polymer Solar Cells: Justification for Use of Silver. *Energy and Environmental Science* **2014**, *7* (3), 1006–1012. https://doi.org/10.1039/c3ee43746a.

(14) Burke, D. J.; Lipomi, D. J. Green Chemistry for Organic Solar Cells. *Energy and Environmental Science* **2013**, *6* (7), 2053–2066. https://doi.org/10.1039/c3ee41096j.

(15) Li, G.; Zhu, R.; Yang, Y. Polymer Solar Cells. *Nature Photonics* **2012**, *6* (3), 153–161. https://doi.org/10.1038/nphoton.2012.11.

(16) Ilievski, F.; Mazzeo, A. D.; Shepherd, R. F.; Chen, X.; Whitesides, G. M. Soft Robotics for Chemists. *Angewandte Chemie International Edition* **2011**, *50* (8), 1890–1895. https://doi.org/10.1002/anie.201006464.

(17) Jinno, H.; Fukuda, K.; Xu, X.; Park, S.; Suzuki, Y.; Koizumi, M.; Yokota, T.; Osaka, I.; Takimiya, K.; Someya, T. Stretchable and Waterproof Elastomer-Coated Organic Photovoltaics for Washable Electronic Textile Applications. *Nature Energy* **2017**, *2* (10), 780–785. https://doi.org/10.1038/s41560-017-0001-3.

(18) Krebs, F. C.; Biancardo, M.; Winther-Jensen, B.; Spanggard, H.; Alstrup, J. Strategies for Incorporation of Polymer Photovoltaics into Garments and Textiles. *Solar Energy Materials and Solar Cells* **2006**, *90* (7–8), 1058–1067. https://doi.org/10.1016/j.solmat.2005.06.003.

(19) O'Connor, T. F.; Zaretski, A. V.; Shiravi, B. A.; Savagatrup, S.; Printz, A. D.; Diaz, M. I.; Lipomi, D. J. Stretching and Conformal Bonding of Organic Solar Cells to Hemispherical Surfaces. *Energy and Environmental Science* **2014**, *7* (1), 370–378. https://doi.org/10.1039/c3ee42898b.

(20) Shirakawa, H.; Louis, E. J.; MacDiarmid, A. G.; Chiang, C. K.; Heeger, A. J. Synthesis of Electrically Conducting Organic Polymers: Halogen Derivatives of Polyacetylene, (CH) x. *Journal of the Chemical Society, Chemical Communications* **1977**, *36* (16), 578. https://doi.org/10.1039/c39770000578.

(21) Weinberger, B. R.; Akhtar, M.; Gau, S. C. Polyacetylene Photovoltaic Devices. *Synthetic Metals* **1982**, *4* (3), 187–197. https://doi.org/10.1016/0379-6779(82)90012-1.

(22) Marks, R. N.; Halls, J. J. M.; Bradley, D. D. C.; Friend, R. H.; Holmes, A. B. The Photovoltaic Response in Poly(p-Phenylene Vinylene) Thin-Film Devices. *Journal of Physics: Condensed Matter* **1994**, *6* (7), 1379–1394. https://doi.org/10.1088/0953-8984/6/7/009.

(23) Tang, C. W. Two-layer Organic Photovoltaic Cell. *Applied Physics Letters* **1986**, *48* (2), 183–185. https://doi.org/10.1063/1.96937.

(24) Sariciftci, N. S.; Smilowitz, L.; Heeger, A. J.; Wudl, F. Photoinduced Electron Transfer from a Conducting Polymer to Buckminsterfullerene. *Science (1979)* **1992**, *258* (5087), 1474–1476. https://doi.org/10.1126/science.258.5087.1474.

(25) Sariciftci, N. S.; Braun, D.; Zhang, C.; Srdanov, V. I.; Heeger, A. J.; Stucky, G.; Wudl, F. Semiconducting Polymer-buckminsterfullerene Heterojunctions: Diodes, Photodiodes, and Photovoltaic Cells. *Applied Physics Letters* **1993**, *62* (6), 585–587. https://doi.org/10.1063/1.108863.

(26) Halls, J. J. M.; Pichler, K.; Friend, R. H.; Moratti, S. C.; Holmes, A. B. Exciton Diffusion and Dissociation in a Poly(p -phenylenevinylene)/C 60 Heterojunction Photovoltaic Cell. *Applied Physics Letters* **1996**, *68* (22), 3120–3122. https://doi.org/10.1063/1.115797.

(27) Najafov, H.; Lee, B.; Zhou, Q.; Feldman, L. C.; Podzorov, V. Observation of Long-Range Exciton Diffusion in Highly Ordered Organic Semiconductors. *Nature Materials* **2010**, *9* (11), 938–943. https://doi.org/10.1038/nmat2872.

(28) Lunt, R. R.; Giebink, N. C.; Belak, A. A.; Benziger, J. B.; Forrest, S. R. Exciton Diffusion Lengths of Organic Semiconductor Thin Films Measured by Spectrally Resolved Photoluminescence Quenching. *Journal of Applied Physics* **2009**, *105* (5). https://doi.org/10.1063/1.3079797.

(29) Luhman, W. A.; Holmes, R. J. Investigation of Energy Transfer in Organic Photovoltaic Cells and Impact on Exciton Diffusion Length Measurements. *Advanced Functional Materials* **2011**, *21* (4), 764–771. https://doi.org/10.1002/adfm.201001928.

(30) Yu, G.; Gao, J.; Hummelen, J. C.; Wudl, F.; Heeger, A. J. Polymer Photovoltaic Cells: Enhanced Efficiencies via a Network of Internal Donor-Acceptor Heterojunctions. *Science (1979)* **1995**, *270* (5243), 1789–1791. https://doi.org/10.1126/science.270.5243.1789.

(31) Sariciftci, N. S.; Heeger, A. J. Conjugated Polymer-Accepter Heterojunctions: Diodes, Photodiodes, and Photovoltaic Cells. 5331183, 1994.

(32) Dou, L.; You, J.; Hong, Z.; Xu, Z.; Li, G.; Street, R. A.; Yang, Y. 25th Anniversary Article: A Decade of Organic/Polymeric Photovoltaic Research. *Advanced Materials*. John Wiley & Sons, Ltd December 1, 2013, pp 6642–6671. https://doi.org/10.1002/adma.201302563.

(33) Hummelen, J. C.; Knight, B. W.; Lepeq, F.; Wudl, F.; Yao, J.; Wilkins, C. L. Preparation and Characterization of Fulleroid and Methanofullerene Derivatives. *Journal of Organic Chemistry* **1995**, *60* (3), 532–538. https://doi.org/10.1021/jo00108a012.

(34) Yu, G.; Heeger, A. J. Charge Separation and Photovoltaic Conversion in Polymer Composites with Internal Donor/Acceptor Heterojunctions. *Journal of Applied Physics* **1995**, *78* (7), 4510–4515. https://doi.org/10.1063/1.359792.

(35) Halls, J. J. M.; Walsh, C. A.; Greenham, N. C.; Marseglia, E. A.; Friend, R. H.; Moratti, S. C.; Holmes, A. B. Efficient Photodiodes from Interpenetrating Polymer Networks. *Nature* **1995**, *376* (6540), 498–500. https://doi.org/10.1038/376498a0.

(36) Li, W.; Yao, H.; Zhang, H.; Li, S.; Hou, J. Potential of Nonfullerene Small Molecules with High Photovoltaic Performance. *Chemistry - An Asian Journal* **2017**, *12* (17), 2160–2171. https://doi.org/10.1002/asia.201700692.

(37) Cheng, P.; Li, G.; Zhan, X.; Yang, Y. Next-Generation Organic Photovoltaics Based on Non-Fullerene Acceptors. *Nature Photonics* **2018**, *12* (3), 131–142. https://doi.org/10.1038/s41566-018-0104-9.

(38) Fabiano, S.; Chen, Z.; Vahedi, S.; Facchetti, A.; Pignataro, B.; Loi, M. A. Role of Photoactive Layer Morphology in High Fill Factor All-Polymer Bulk Heterojunction Solar Cells. *Journal of Materials Chemistry* **2011**, *21* (16), 5891–5896. https://doi.org/10.1039/c0jm03405c.

(39) Moore, J. R.; Albert-Seifried, S.; Rao, A.; Massip, S.; Watts, B.; Morgan, D. J.; Friend, R. H.; McNeill, C. R.; Sirringhaus, H. Polymer Blend Solar Cells Based on a High-Mobility Naphthalenediimide-Based Polymer Acceptor: Device Physics, Photophysics and Morphology. *Advanced Energy Materials* **2011**, *1* (2), 230–240. https://doi.org/10.1002/aenm.201000035.

(40) Lin, Y.; Wang, J.; Zhang, Z.-G.; Bai, H.; Li, Y.; Zhu, D.; Zhan, X. An Electron Acceptor Challenging Fullerenes for Efficient Polymer Solar Cells. *Advanced Materials* **2015**, *27* (7), 1170–1174. https://doi.org/10.1002/adma.201404317.

(41) Roth, B.; Savagatrup, S.; V. de los Santos, N.; Hagemann, O.; Carlé, J. E.; Helgesen, M.; Livi, F.; Bundgaard, E.; Søndergaard, R. R.; Krebs, F. C.; Lipomi, D. J. Mechanical Properties of a Library of Low-Band-Gap Polymers. *Chemistry of Materials* **2016**, *28* (7), 2363–2373. https://doi.org/10.1021/acs.chemmater.6b00525.

(42) Zhou, H.; Yang, L.; Stoneking, S.; You, W. A Weak Donor−Strong Acceptor Strategy to Design Ideal Polymers for Organic Solar Cells. *ACS Applied Materials & Interfaces* **2010**, *2* (5), 1377–1383. https://doi.org/10.1021/am1000344.

(43) Zhao, J.; Li, Y.; Yang, G.; Jiang, K.; Lin, H.; Ade, H.; Ma, W.; Yan, H. Efficient Organic Solar Cells Processed from Hydrocarbon Solvents. *Nature Energy* **2016**, *1* (2). https://doi.org/10.1038/NENERGY.2015.27.

(44) Sun, H.; Liu, B.; Ma, Y.; Lee, J. W.; Yang, J.; Wang, J.; Li, Y.; Li, B.; Feng, K.; Shi, Y.; Zhang, B.; Han, D.; Meng, H.; Niu, L.; Kim, B. J.; Zheng, Q.; Guo, X. Regioregular Narrow-Bandgap n-Type Polymers with High Electron Mobility Enabling Highly Efficient All-Polymer Solar Cells. *Advanced Materials* **2021**, *33* (37), 2102635. https://doi.org/10.1002/ADMA.202102635.

(45) Green, M. A.; Hishikawa, Y.; Dunlop, E. D.; Levi, D. H.; Hohl-Ebinger, J.; Yoshita, M.; Ho-Baillie, A. W. Y. Solar Cell Efficiency Tables (Version 53). *Progress in Photovoltaics: Research and Applications* **2019**, *27* (1), 3–12. https://doi.org/10.1002/pip.3102.

(46) Branker, K.; Pathak, M. J. M.; Pearce, J. M. A Review of Solar Photovoltaic Levelized Cost of Electricity. *Renewable and Sustainable Energy Reviews* **2011**, *15* (9), 4470–4482. https://doi.org/10.1016/J.RSER.2011.07.104.

(47) Feldman, D.; Margolis, R. *Q4 2018 / Q1 2019 Solar Industry Update*; 2018.

(48) Park, S.; Kim, T.; Yoon, S.; Woo Koh, C.; Young Woo, H.; Jung Son, H.; Park, S.; Kim, T.; Yoon, S.; Son, H. J.; Koh, C. W.; Woo, H. Y. Progress in Materials, Solution Processes, and Long-Term Stability for Large-Area Organic Photovoltaics. *Advanced Materials* **2020**, *32* (51), 2002217. https://doi.org/10.1002/ADMA.202002217.

(49) Meng, L.; You, J.; Yang, Y. Addressing the Stability Issue of Perovskite Solar Cells for Commercial Applications. https://doi.org/10.1038/s41467-018-07255-1.

(50) Moro, A.; Boelman, E.; Joanny, G.; Lopez-Garcia, J. A Bibliometric-Based Technique to Identify Emerging Photovoltaic Technologies in a Comparative Assessment with Expert Review. *Renewable Energy* **2018**, *123*, 407–416. https://doi.org/10.1016/J.RENENE.2018.02.016.

(51) Azzopardi, B.; Emmott, C. J. M.; Urbina, A.; Krebs, F. C.; Mutale, J.; Nelson, J. Economic Assessment of Solar Electricity Production from Organic-Based Photovoltaic Modules in a Domestic Environment. *Energy and Environmental Science* **2011**, *4* (10), 3741–3753. https://doi.org/10.1039/c1ee01766g.

(52) Guo, J.; Min, J. A Cost Analysis of Fully Solution-Processed ITO-Free Organic Solar Modules. *Advanced Energy Materials* **2019**, *9* (3), 1–9. https://doi.org/10.1002/aenm.201802521.

(53) Green, M. A.; Dunlop, E. D.; Hohl-Ebinger, J.; Yoshita, M.; Kopidakis, N.; Bothe, K.; Hinken, D.; Rauer, M.; Hao, X. Solar Cell Efficiency Tables (Version 60). **2022**. https://doi.org/10.1002/pip.3595.

(54) Li, Y.; Huang, X.; Ding, K.; Sheriff, H. K. M.; Ye, L.; Liu, H.; Li, C. Z.; Ade, H.; Forrest, S. R. Non-Fullerene Acceptor Organic Photovoltaics with Intrinsic Operational Lifetimes over 30 Years. *Nature Communications 2021 12:1* **2021**, *12* (1), 1–9. https://doi.org/10.1038/s41467-021-25718-w.

(55) Zhang, Y.; Samuel, I. D. W.; Wang, T.; Lidzey, D. G. Current Status of Outdoor Lifetime Testing of Organic Photovoltaics. *Advanced Science* **2018**, *5* (8). https://doi.org/10.1002/advs.201800434.

(56) Po, R.; Bianchi, G.; Carbonera, C.; Pellegrino, A. “All That Glisters Is Not Gold”: An Analysis of the Synthetic Complexity of Efficient Polymer Donors for Polymer Solar Cells. *Macromolecules* **2015**, *48* (3), 453–461. https://doi.org/10.1021/ma501894w.

(57) Sun, C.; Pan, F.; Bin, H.; Zhang, J.; Xue, L.; Qiu, B.; Wei, Z.; Zhang, Z. G.; Li, Y. A Low Cost and High Performance Polymer Donor Material for Polymer Solar Cells. *Nature*

Communications 2018 9:1 **2018**, *9* (1), 1–10. https://doi.org/10.1038/s41467-018-03207-x.

(58) Rech, J. J.; Neu, J.; Qin, Y.; Samson, S.; Shanahan, J.; Josey, R. F.; Ade, H.; You, W. Designing Simple Conjugated Polymers for Scalable and Efficient Organic Solar Cells. *ChemSusChem* **2021**, *14* (17), 3561–3568. https://doi.org/10.1002/CSSC.202100910.

(59) Lanzani, G.; Petrozza, A.; Caironi, M. Organics Go Hybrid. *Nature Photonics* **2017**, *11* (1), 20–22. https://doi.org/10.1038/nphoton.2016.260.

(60) You, Y. J.; Song, C. E.; Hoang, Q. V.; Kang, Y.; Goo, J. S.; Ko, D. H.; Lee, J. J.; Shin, W. S.; Shim, J. W. Highly Efficient Indoor Organic Photovoltaics with Spectrally Matched Fluorinated Phenylene-Alkoxybenzothiadiazole-Based Wide Bandgap Polymers. *Advanced Functional Materials* **2019**, *1901171*, 1–11. https://doi.org/10.1002/adfm.201901171.

(61) Cutting, C. L.; Bag, M.; Venkataraman, D. Indoor Light Recycling: A New Home for Organic Photovoltaics. *Journal of Materials Chemistry C* **2016**, *4* (43), 10367–10370. https://doi.org/10.1039/c6tc03344j.

(62) Cui, Y.; Wang, Y.; Bergqvist, J.; Yao, H.; Xu, Y.; Gao, B.; Yang, C.; Zhang, S.; Inganäs, O.; Gao, F.; Hou, J. Wide-Gap Non-Fullerene Acceptor Enabling High-Performance Organic Photovoltaic Cells for Indoor Applications. *Nature Energy* **2019**, *4* (9), 768–775. https://doi.org/10.1038/s41560-019-0448-5.

(63) Li, N.; Brabec, C. J. Washing Away Barriers. *Nature Energy 2017 2:10* **2017**, *2* (10), 772–773. https://doi.org/10.1038/s41560-017-0011-1.

(64) Mateker, W. R.; McGehee, M. D.; Mateker, W. R.; McGehee, M. D. Progress in Understanding Degradation Mechanisms and Improving Stability in Organic Photovoltaics. *Advanced Materials* **2017**, *29* (10), 1603940. https://doi.org/10.1002/ADMA.201603940.

(65) Cheng, P.; Zhan, X. Stability of Organic Solar Cells: Challenges and Strategies. *Chemical Society Reviews* **2016**, *45* (9), 2544–2582. https://doi.org/10.1039/C5CS00593K.

(66) Suzuki, M.; Suzuki, K.; Won, T.; Yamada, H. Impact of Substituents on the Performance of Small-Molecule Semiconductors in Organic Photovoltaic Devices *via* Regulating Morphology. *Journal of Materials Chemistry C* **2022**, *10* (4), 1162–1195. https://doi.org/10.1039/D1TC04237H.

(67) Gaspar, H.; Figueira, F.; Pereira, L.; Mendes, A.; Viana, J.; Bernardo, G. Recent Developments in the Optimization of the Bulk Heterojunction Morphology of Polymer: Fullerene Solar Cells. *Materials* **2018**, *11* (12), 2560. https://doi.org/10.3390/ma11122560.

(68) Yoon, S.; Shin, E.-Y.; Cho, N.-K.; Park, S.; Woo, H. Y.; Son, H. J. Progress in Morphology Control from Fullerene to Nonfullerene Acceptors for Scalable High-

Performance Organic Photovoltaics. *Journal of Materials Chemistry A* **2021**, *9* (44), 24729–24758. https://doi.org/10.1039/D1TA06861J.

(69) Collins, B. A.; Tumbleston, J. R.; Ade, H. Miscibility, Crystallinity, and Phase Development in P3HT/PCBM Solar Cells: Toward an Enlightened Understanding of Device Morphology and Stability. *Journal of Physical Chemistry Letters* **2011**, *2* (24), 3135–3145. https://doi.org/10.1021/jz2014902.

(70) Ma, W.; Tumbleston, J. R.; Wang, M.; Gann, E.; Huang, F.; Ade, H. Domain Purity, Miscibility, and Molecular Orientation at Donor/Acceptor Interfaces in High Performance Organic Solar Cells: Paths to Further Improvement. *Advanced Energy Materials* **2013**, *3* (7), 864–872. https://doi.org/10.1002/aenm.201200912.

(71) Hu, H.; Ghasemi, M.; Peng, Z.; Zhang, J.; Rech, J. J.; You, W.; Yan, H.; Ade, H. The Role of Demixing and Crystallization Kinetics on the Stability of Non-Fullerene Organic Solar Cells. *Advanced Materials* **2020**, *32* (49), 1–9. https://doi.org/10.1002/adma.202005348.

(72) Liu, Y.; Zhao, J.; Li, Z.; Mu, C.; Ma, W.; Hu, H.; Jiang, K.; Lin, H.; Ade, H.; Yan, H. Aggregation and Morphology Control Enables Multiple Cases of High-Efficiency Polymer Solar Cells. *Nature Communications* **2014**, *5* (9), 1–8. https://doi.org/10.1038/ncomms6293.

(73) Ghasemi, M.; Hu, H.; Peng, Z.; Rech, J. J.; Angunawela, I.; Carpenter, J. H.; Stuard, S. J.; Wadsworth, A.; McCulloch, I.; You, W.; Ade, H. Delineation of Thermodynamic and Kinetic Factors That Control Stability in Non-Fullerene Organic Solar Cells. *Joule* **2019**, *3* (5), 1328–1348. https://doi.org/10.1016/j.joule.2019.03.020.

(74) Ghasemi, M.; Balar, N.; Peng, Z.; Hu, H.; Qin, Y.; Kim, T.; Rech, J. J.; Bidwell, M.; Mask, W.; McCulloch, I.; You, W.; Amassian, A.; Risko, C.; O'Connor, B. T.; Ade, H. A Molecular Interaction–Diffusion Framework for Predicting Organic Solar Cell Stability. *Nature Materials* **2021**. https://doi.org/10.1038/s41563-020-00872-6.

(75) Brédas, J. L.; Cornil, J.; Heeger, A. J. The Exciton Binding Energy in Luminescent Conjugated Polymers. *Advanced Materials* **1996**, *8* (5), 447–452. https://doi.org/10.1002/adma.19960080517.

(76) Nakano, K.; Chen, Y.; Xiao, B.; Han, W.; Huang, J.; Yoshida, H.; Zhou, E.; Tajima, K. Anatomy of the Energetic Driving Force for Charge Generation in Organic Solar Cells. *Nature Communications* **2019**, *10* (1), 2520. https://doi.org/10.1038/s41467-019-10434-3.

(77) Clarke, T. M.; Durrant, J. R. Charge Photogeneration in Organic Solar Cells. *Chemical Reviews* **2010**, *110* (11), 6736–6767. https://doi.org/10.1021/cr900271s.

(78) Gaspar, H.; Figueira, F.; Pereira, L.; Mendes, A.; Viana, J.; Bernardo, G.; Gaspar, H.; Figueira, F.; Pereira, L.; Mendes, A.; Viana, J. C.; Bernardo, G. Recent Developments in the Optimization of the Bulk Heterojunction Morphology of Polymer: Fullerene Solar Cells. *Materials* **2018**, *11* (12), 2560. https://doi.org/10.3390/ma11122560.

(79) Zhao, F.; Wang, C.; Zhan, X. Morphology Control in Organic Solar Cells. *Advanced Energy Materials* **2018**, *8* (28), 1703147. https://doi.org/10.1002/aenm.201703147.

(80) Mihailetchi, V. D.; Blom, P. W. M.; Hummelen, J. C.; Rispens, M. T. Cathode Dependence of the Open-Circuit Voltage of Polymer:Fullerene Bulk Heterojunction Solar Cells. *Journal of Applied Physics* **2003**, *94* (10), 6849–6854. https://doi.org/10.1063/1.1620683.

(81) Müller-Buschbaum, P. The Active Layer Morphology of Organic Solar Cells Probed with Grazing Incidence Scattering Techniques. *Advanced Materials* **2014**, *26* (46), 7692–7709. https://doi.org/10.1002/adma.201304187.

(82) Reynolds, J. R.; Thompson, B. C.; Skotheim, T. A.; Ye, L.; Stuard, S. J.; Ade, H. *Conjugated Polymers: Properties, Processing, and Applications*; 2019. https://doi.org/10.1201/9780429190520-13.

(83) Müller-Buschbaum, P. The Active Layer Morphology of Organic Solar Cells Probed with Grazing Incidence Scattering Techniques. *Advanced Materials* **2014**, *26* (46), 7692–7709. https://doi.org/10.1002/adma.201304187.

(84) Gu, K. L.; Zhou, Y.; Morrison, W. A.; Park, K.; Park, S.; Bao, Z. Nanoscale Domain Imaging of All-Polymer Organic Solar Cells by Photo-Induced Force Microscopy. *ACS Nano* **2018**, *12* (2), 1473–1481. https://doi.org/10.1021/acsnano.7b07865.

(85) Hexemer, A.; Müller-Buschbaum, P. Advanced Grazing-Incidence Techniques for Modern Soft-Matter Materials Analysis. *IUCrJ* **2015**, *2*, 106–125. https://doi.org/10.1107/S2052252514024178.

(86) Pfannmöller, M.; Kowalsky, W.; Schröder, R. R. Visualizing Physical, Electronic, and Optical Properties of Organic Photovoltaic Cells. *Energy & Environmental Science* **2013**, *6* (10), 2871. https://doi.org/10.1039/c3ee41773e.

(87) Santoro, G.; Yu, S. Grazing Incidence Small Angle X-Ray Scattering as a Tool for In-Situ Time-Resolved Studies. In *X-ray Scattering*; InTech, 2017. https://doi.org/10.5772/64877.

(88) Pham, T.; Goldstein, A. P.; Lewicki, J. P.; Kucheyev, S. O.; Wang, C.; Russell, T. P.; Worsley, M. A.; Woo, L.; Mickelson, W.; Zettl, A. Nanoscale Structure and Superhydrophobicity of Sp ^{2} -Bonded Boron Nitride Aerogels. *Nanoscale* **2015**, *7* (23), 10449–10458. https://doi.org/10.1039/C5NR01672J.

(89) Wang, C.; Hexemer, A.; Nasiatka, J.; Chan, E. R.; Young, A. T.; Padmore, H. A.; Schlotter, W. F.; Lüning, J.; Swaraj, S.; Watts, B.; Gann, E.; Yan, H.; Ade, H. Resonant Soft X-Ray Scattering of Polymers with a 2D Detector: Initial Results and System Developments at the Advanced Light Source. *IOP Conference Series: Materials Science and Engineering* **2010**, *14*, 012016. https://doi.org/10.1088/1757-899x/14/1/012016.

(90) Schuettfort, T.; Thomsen, L.; McNeill, C. R. Observation of a Distinct Surface Molecular Orientation in Films of a High Mobility Conjugated Polymer. *J Am Chem Soc* **2013**, *135* (3), 1092–1101. https://doi.org/10.1021/ja310240q.

(91) Liu, F.; Brady, M. A.; Wang, C. Resonant Soft X-Ray Scattering for Polymer Materials. *European Polymer Journal* **2016**, *81*, 555–568. https://doi.org/10.1016/j.eurpolymj.2016.04.014.

(92) Ade, H.; Wang, C.; Yan, H. The Case for Soft X-Rays: Improved Compositional Contrast for Structure and Morphology Determination with Real and Reciprocal Space Methods. *IOP Conference Series: Materials Science and Engineering* **2010**, *14* (1), 012020. https://doi.org/10.1088/1757-899X/14/1/012020.

(93) Ruderer, M. A.; Wang, C.; Schaible, E.; Hexemer, A.; Xu, T.; Müller-Buschbaum, P. Morphology and Optical Properties of P3HT:MEH-CN-PPV Blend Films. *Macromolecules* **2013**, *46* (11), 4491–4501. https://doi.org/10.1021/ma4006999.

(94) Collins, B. A.; Li, Z.; Tumbleston, J. R.; Gann, E.; McNeill, C. R.; Ade, H. Absolute Measurement of Domain Composition and Nanoscale Size Distribution Explains Performance in PTB7:PC $_{71}$ BM Solar Cells. *Advanced Energy Materials* **2013**, *3* (1), 65–74. https://doi.org/10.1002/aenm.201200377.

(95) Du, X.; Heumueller, T.; Gruber, W.; Classen, A.; Unruh, T.; Li, N.; Brabec, C. J. Efficient Polymer Solar Cells Based on Non-Fullerene Acceptors with Potential Device Lifetime Approaching 10 Years. *Joule* **2019**, *3* (1), 215–226. https://doi.org/10.1016/J.JOULE.2018.09.001/ATTACHMENT/112E74E3-48EF-41A5-BCB7-0ACC69F17D4C/MMC1.PDF.

(96) Forrest, S. R. *Organic Electronics: Foundations to Applications*; Oxford University Press, 2020. https://doi.org/10.1093/oso/9780198529729.001.0001.

(97) Burlingame, Q.; Huang, X.; Liu, X.; Jeong, C.; Coburn, C.; Forrest, S. R. Intrinsically Stable Organic Solar Cells under High-Intensity Illumination. *Nature 2019 573:7774* **2019**, *573* (7774), 394–397. https://doi.org/10.1038/s41586-019-1544-1.

(98) Reese, M. O.; Gevorgyan, S. A.; Jørgensen, M.; Bundgaard, E.; Kurtz, S. R.; Ginley, D. S.; Olson, D. C.; Lloyd, M. T.; Morvillo, P.; Katz, E. A.; Elschner, A.; Haillant, O.; Currier, T. R.; Shrotriya, V.; Hermenau, M.; Riede, M.; Kirov, K. R.; Trimmel, G.; Rath, T.; Inganäs, O.; Zhang, F.; Andersson, M.; Tvingstedt, K.; Lira-Cantu, M.; Laird, D.; McGuiness, C.; Gowrisanker, S.; Pannone, M.; Xiao, M.; Hauch, J.; Steim, R.; Delongchamp, D. M.; Rösch, R.; Hoppe, H.; Espinosa, N.; Urbina, A.; Yaman-Uzunoglu, G.; Bonekamp, J. B.; van Breemen, A. J. J. M.; Girotto, C.; Voroshazi, E.; Krebs, F. C. Consensus Stability Testing Protocols for Organic Photovoltaic Materials and Devices. *Solar Energy Materials and Solar Cells* **2011**, *95* (5), 1253–1267. https://doi.org/10.1016/j.solmat.2011.01.036.

(99) Burlingame, Q.; Huang, X.; Liu, X.; Jeong, C.; Coburn, C.; Forrest, S. R. Intrinsically Stable Organic Solar Cells under High-Intensity Illumination. *Nature 2019 573:7774* **2019**, *573* (7774), 394–397. https://doi.org/10.1038/s41586-019-1544-1.

(100) Haillant, O.; Dumbleton, D.; Zielnik, A. An Arrhenius Approach to Estimating Organic Photovoltaic Module Weathering Acceleration Factors. *Solar Energy Materials and Solar Cells* **2011**, *95* (7), 1889–1895. https://doi.org/10.1016/j.solmat.2011.02.013.

(101) Dixon, R. R. *THERMAL AGING PREDICTIONS FROM AN ARRHENIUS PLOT WITH ONLY ONE DATA POINT*; 1980. https://doi.org/10.1109/TEI.1980.298259.

(102) Burlingame, Q.; Huang, X.; Liu, X.; Jeong, C.; Coburn, C.; Forrest, S. R. Intrinsically Stable Organic Solar Cells under High-Intensity Illumination. *Nature* **2019**, *573* (7774), 394–397. https://doi.org/10.1038/s41586-019-1544-1.

(103) Nunes, R. W.; Martin, J. R.; Johnson, J. F. Influence of Molecular Weight and Molecular Weight Distribution on Mechanical Properties of Polymers. *Polymer Engineering & Science* **1982**, *22* (4), 205–228. https://doi.org/10.1002/pen.760220402.

(104) Seitz, J. T. The Estimation of Mechanical Properties of Polymers from Molecular Structure. *Journal of Applied Polymer Science* **1993**, *49* (8), 1331–1351. https://doi.org/10.1002/app.1993.070490802.

(105) Choi, J.; Kim, W.; Kim, D.; Kim, S.; Chae, J.; Choi, S. Q.; Kim, F. S.; Kim, T. S.; Kim, B. J. Importance of Critical Molecular Weight of Semicrystalline N-Type Polymers for Mechanically Robust, Efficient Electroactive Thin Films. *Chemistry of Materials* **2019**, *31* (9), 3163–3173. https://doi.org/10.1021/acs.chemmater.8b05114.

(106) Savagatrup, S.; Printz, A. D.; O'Connor, T. F.; Zaretski, A. V.; Lipomi, D. J. Molecularly Stretchable Electronics. *Chemistry of Materials* **2014**, *26* (10), 3028–3041. https://doi.org/10.1021/cm501021v.

(107) Ma, W.; Kim, J. Y.; Lee, K.; Heeger, A. J. Effect of the Molecular Weight of Poly(3-Hexylthiophene) on the Morphology and Performance of Polymer Bulk Heterojunction Solar Cells. *Macromolecular Rapid Communications* **2007**, *28* (17), 1776–1780. https://doi.org/10.1002/marc.200700280.

(108) Ma, W.; Yang, G.; Jiang, K.; Carpenter, J. H.; Wu, Y.; Meng, X.; McAfee, T.; Zhao, J.; Zhu, C.; Wang, C.; Ade, H.; Yan, H. Influence of Processing Parameters and Molecular Weight on the Morphology and Properties of High-Performance PffBT4T-2OD:PC71BM Organic Solar Cells. *Advanced Energy Materials* **2015**, *5* (23), 1–9. https://doi.org/10.1002/aenm.201501400.

(109) Zhou, N.; Dudnik, A. S.; Li, T. I. N. G. N. G.; Manley, E. F.; Aldrich, T. J.; Guo, P.; Liao, H.-C. C.; Chen, Z.; Chen, L. X.; Chang, R. P. H. H.; Facchetti, A.; Olvera de la Cruz, M.; Marks, T. J. All-Polymer Solar Cell Performance Optimized via Systematic Molecular Weight Tuning of Both Donor and Acceptor Polymers. *J Am Chem Soc* **2016**, *138* (4), 1240–1251. https://doi.org/10.1021/jacs.5b10735.

(110) Balar, N.; Rech, J. J.; Henry, R.; Ye, L.; Ade, H.; You, W.; O'Connor, B. T. The Importance of Entanglements in Optimizing the Mechanical and Electrical Performance of All-Polymer Solar Cells. *Chemistry of Materials* **2019**, *31* (14), 5124–5132. https://doi.org/10.1021/acs.chemmater.9b01011.

(111) Savagatrup, S.; Printz, A. D.; Rodriquez, D.; Lipomi, D. J. Best of Both Worlds: Conjugated Polymers Exhibiting Good Photovoltaic Behavior and High Tensile Elasticity. *Macromolecules* **2014**, *47* (6), 1981–1992. https://doi.org/10.1021/ma500286d.

(112) Grand, C.; Reynolds, J. R. The Interplay between Structure, Processing, and Properties in Organic Photovoltaic Devices: How to Translate Recent Laboratory-Scale Developments to Modules. *MRS Communications* **2015**, *5* (2), 155–167. https://doi.org/10.1557/mrc.2015.24.

(113) Li, W.; Yang, L.; Tumbleston, J. R.; Yan, L.; Ade, H.; You, W. Controlling Molecular Weight of a High Efficiency Donor-Acceptor Conjugated Polymer and Understanding Its Significant Impact on Photovoltaic Properties. *Advanced Materials* **2014**, *26* (26), 4456–4462. https://doi.org/10.1002/adma.201305251.

(114) Khan, J. I.; Ashraf, R. S.; Alamoudi, M. A.; Nabi, M. N.; Mohammed, H. N.; Wadsworth, A.; Firdaus, Y.; Zhang, W.; Anthopoulos, T. D.; McCulloch, I.; Laquai, F. P3HT Molecular Weight Determines the Performance of P3HT:O-IDTBR Solar Cells. *Solar RRL* **2019**, *3* (April), 1900023. https://doi.org/10.1002/solr.201900023.

(115) Deshmukh, K. D.; Matsidik, R.; Prasad, S. K. K.; Connal, L. A.; Liu, A. C. Y.; Gann, E.; Thomsen, L.; Hodgkiss, J. M.; Sommer, M.; McNeill, C. R. Tuning the Molecular Weight of the Electron Accepting Polymer in All-Polymer Solar Cells: Impact on Morphology and Charge Generation. *Advanced Functional Materials* **2018**, *28* (18), 1–13. https://doi.org/10.1002/adfm.201707185.

(116) Nicolet, C.; Deribew, D.; Renaud, C.; Fleury, G.; Brochon, C.; Cloutet, E.; Vignau, L.; Wantz, G.; Cramail, H.; Geoghegan, M.; Hadziioannou, G. Optimization of the Bulk Heterojunction Composition for Enhanced Photovoltaic Properties: Correlation between the Molecular Weight of the Semiconducting Polymer and Device Performance. *Journal of Physical Chemistry B* **2011**, *115* (44), 12717–12727. https://doi.org/10.1021/jp207669j.

(117) Osaka, I.; Saito, M.; Mori, H.; Koganezawa, T.; Takimiya, K. Drastic Change of Molecular Orientation in a Thiazolothiazole Copolymer by Molecular-Weight Control and Blending with PC 61BM Leads to High Efficiencies in Solar Cells. *Advanced Materials* **2012**, *24* (3), 425–430. https://doi.org/10.1002/adma.201103065.

(118) Xiong, W.; Qi, F.; Liu, T.; Huo, L.; Xue, X.; Bi, Z.; Zhang, Y.; Ma, W.; Wan, M.; Liu, J.; Sun, Y. Controlling Molecular Weight to Achieve High-Efficient Polymer Solar Cells With Unprecedented Fill Factor of 79% Based on Non-Fullerene Small Molecule Acceptor. *Solar RRL* **2018**, *2* (9), 1800129. https://doi.org/10.1002/solr.201800129.

(119) Wadsworth, A.; Hamid, Z.; Bidwell, M.; Ashraf, R. S.; Khan, J. I.; Anjum, D. H.; Cendra, C.; Yan, J.; Rezasoltani, E.; Guilbert, A. A. Y. Y.; Azzouzi, M.; Gasparini, N.; Bannock,

J. H.; Baran, D.; Wu, H.; de Mello, J. C.; Brabec, C. J.; Salleo, A.; Nelson, J.; Laquai, F.; McCulloch, I. Progress in Poly (3-Hexylthiophene) Organic Solar Cells and the Influence of Its Molecular Weight on Device Performance. *Advanced Energy Materials* **2018**, *8* (28), 1–15. https://doi.org/10.1002/aenm.201801001.

(120) Choi, J.; Kim, W.; Kim, S.; Kim, T. S.; Kim, B. J. Influence of Acceptor Type and Polymer Molecular Weight on the Mechanical Properties of Polymer Solar Cells. *Chemistry of Materials* **2019**, *31*, 9057–9069. https://doi.org/10.1021/acs.chemmater.9b03333.

(121) Mauer, R.; Kastler, M.; Laquai, F. The Impact of Polymer Regioregularity on Charge Transport and Efficiency of P3HT:PCBM Photovoltaic Devices. *Advanced Functional Materials* **2010**, *20* (13), 2085–2092. https://doi.org/10.1002/adfm.201000320.

(122) Ballantyne, A. M.; Chen, L.; Dane, J.; Hammant, T.; Braun, F. M.; Heeney, M.; Duffy, W.; McCulloch, I.; Bradley, D. D. C.; Nelson, J. The Effect of Poly(3-Hexylthiophene) Molecular Weight on Charge Transport and the Performance of Polymer: Fullerene Solar Cells. *Advanced Functional Materials* **2008**, *18* (16), 2373–2380. https://doi.org/10.1002/adfm.200800145.

(123) Spoltore, D.; Vangerven, T.; Verstappen, P.; Piersimoni, F.; Bertho, S.; Vandewal, K.; Van Den Brande, N.; Defour, M.; Van Mele, B.; De Sio, A.; Parisi, J.; Lutsen, L.; Vanderzande, D.; Maes, W.; Manca, J. V. Effect of Molecular Weight on Morphology and Photovoltaic Properties in P3HT:PCBM Solar Cells. *Organic Electronics: physics, materials, applications* **2015**, *21*, 160–170. https://doi.org/10.1016/j.orgel.2015.02.017.

(124) Huang, Z.; Fregoso, E. C.; Dimitrov, S.; Tuladhar, P. S.; Soon, Y. W.; Bronstein, H.; Meager, I.; Zhang, W.; McCulloch, I.; Durrant, J. R. Optimisation of Diketopyrrolopyrrole:Fullerene Solar Cell Performance through Control of Polymer Molecular Weight and Thermal Annealing. *Journal of Materials Chemistry A* **2014**, *2* (45), 19282–19289. https://doi.org/10.1039/c4ta03589e.

(125) McNeill, C. R.; Abrusci, A.; Zaumseil, J.; Wilson, R.; McKiernan, M. J.; Burroughes, J. H.; Halls, J. J. M.; Greenham, N. C.; Friend, R. H. Dual Electron Donor/Electron Acceptor Character of a Conjugated Polymer in Efficient Photovoltaic Diodes. *Applied Physics Letters* **2007**, *90* (19), 4–7. https://doi.org/10.1063/1.2738197.

(126) Price, S. C.; Stuart, A. C.; Yang, L.; Zhou, H.; You, W. Fluorine Substituted Conjugated Polymer of Medium Band Gap Yields 7% Efficiency in Polymer-Fullerene Solar Cells. *J Am Chem Soc* **2011**, *133* (12), 4625–4631. https://doi.org/10.1021/ja1112595.

(127) Philippa, B.; Stolterfoht, M.; Burn, P. L.; Juška, G.; Meredith, P.; White, R. D.; Pivrikas, A. The Impact of Hot Charge Carrier Mobility on Photocurrent Losses in Polymer-Based Solar Cells. *Scientific Reports* **2014**, *4*, 1–7. https://doi.org/10.1038/srep05695.

(128) Noriega, R.; Rivnay, J.; Vandewal, K.; Koch, F. P. V.; Stingelin, N.; Smith, P.; Toney, M. F.; Salleo, A. A General Relationship between Disorder, Aggregation and Charge

Transport in Conjugated Polymers. *Nature Materials* **2013**, *12* (11), 1038–1044. https://doi.org/10.1038/nmat3722.

(129) Benduhn, J.; Tvingstedt, K.; Piersimoni, F.; Ullbrich, S.; Fan, Y.; Tropiano, M.; McGarry, K. A.; Zeika, O.; Riede, M. K.; Douglas, C. J.; Barlow, S.; Marder, S. R.; Neher, D.; Spoltore, D.; Vandewal, K. Intrinsic Non-Radiative Voltage Losses in Fullerene-Based Organic Solar Cells. *Nature Energy* **2017**, *2* (6), 17053. https://doi.org/10.1038/nenergy.2017.53.

(130) Jiao, X.; Ye, L.; Ade, H. Quantitative Morphology–Performance Correlations in Organic Solar Cells: Insights from Soft X-Ray Scattering. *Advanced Energy Materials* **2017**, *7* (18), 1700084. https://doi.org/10.1002/aenm.201700084.

(131) Müller-Buschbaum, P. The Active Layer Morphology of Organic Solar Cells Probed with Grazing Incidence Scattering Techniques. *Advanced Materials* **2014**, *26* (46), 7692–7709. https://doi.org/10.1002/adma.201304187.

(132) Huang, W.; Gann, E.; Chandrasekaran, N.; Thomsen, L.; Prasad, S. K. K.; Hodgkiss, J. M.; Kabra, D.; Cheng, Y.-B.; McNeill, C. R. Isolating and Quantifying the Impact of Domain Purity on the Performance of Bulk Heterojunction Solar Cells. *Energy & Environmental Science* **2017**, *10* (8), 1843–1853. https://doi.org/10.1039/C7EE01387F.

(133) Mukherjee, S.; Jiao, X.; Ade, H. Charge Creation and Recombination in Multi-Length Scale Polymer:Fullerene BHJ Solar Cell Morphologies. *Advanced Energy Materials* **2016**, *6* (18), 1600699. https://doi.org/10.1002/aenm.201600699.

(134) Ye, L.; Zhao, W.; Li, S.; Mukherjee, S.; Carpenter, J. H.; Awartani, O.; Jiao, X.; Hou, J.; Ade, H. High-Efficiency Nonfullerene Organic Solar Cells: Critical Factors That Affect Complex Multi-Length Scale Morphology and Device Performance. *Advanced Energy Materials* **2017**, *7* (7), 1602000. https://doi.org/10.1002/aenm.201602000.

(135) Ma, W.; Ye, L.; Zhang, S.; Hou, J.; Ade, H. Competition between Morphological Attributes in the Thermal Annealing and Additive Processing of Polymer Solar Cells. *Journal of Materials Chemistry C* **2013**, *1* (33), 5023–5030. https://doi.org/10.1039/c3tc30679h.

(136) Elumalai, N. K.; Uddin, A. Open Circuit Voltage of Organic Solar Cells: An in-Depth Review. *Energy and Environmental Science* **2016**, *9* (2), 391–410. https://doi.org/10.1039/c5ee02871j.

(137) Koster, L. J. A.; Kemerink, M.; Wienk, M. M.; Maturová, K.; Janssen, R. A. J. Quantifying Bimolecular Recombination Losses in Organic Bulk Heterojunction Solar Cells. *Advanced Materials* **2011**, *23* (14), 1670–1674. https://doi.org/10.1002/adma.201004311.

(138) Stolterfoht, M.; Armin, A.; Philippa, B.; White, R. D.; Burn, P. L.; Meredith, P.; Juška, G.; Pivrikas, A. Photocarrier Drift Distance in Organic Solar Cells and Photodetectors. *Scientific Reports* **2015**, *5* (1), 1–7. https://doi.org/10.1038/srep09949.

(139) Koster, L. J. A.; Mihailetchi, V. D.; Ramaker, R.; Xie, H.; Blom, P. W. Light Intensity Dependence of Open-Circuit Voltage and Short-Circuit Current of Polymer/Fullerene Solar Cells. *Organic Optoelectronics and Photonics II* **2006**, *6192* (April 2006), 61922G. https://doi.org/10.1117/12.665471.

(140) Kyaw, A. K. K.; Wang, D. H.; Gupta, V.; Leong, W. L.; Ke, L.; Bazan, G. C.; Heeger, A. J. Intensity Dependence of Current-Voltage Characteristics and Recombination in High-Efficiency Solution-Processed Small-Molecule Solar Cells. *ACS Nano* **2013**, *7* (5), 4569–4577. https://doi.org/10.1021/nn401267s.

(141) Würfel, U.; Perdigón-Toro, L.; Kurpiers, J.; Wolff, C. M.; Caprioglio, P.; Rech, J. J.; Zhu, J.; Zhan, X.; You, W.; Shoaee, S.; Neher, D.; Stolterfoht, M. Recombination between Photogenerated and Electrode-Induced Charges Dominates the Fill Factor Losses in Optimized Organic Solar Cells. *Journal of Physical Chemistry Letters* **2019**, *10* (12), 3473–3480. https://doi.org/10.1021/acs.jpclett.9b01175.

(142) Cowan, S. R.; Roy, A.; Heeger, A. J. Recombination in Polymer-Fullerene Bulk Heterojunction Solar Cells. *Physical Review B* **2010**, *82* (24), 245207. https://doi.org/10.1103/PhysRevB.82.245207.

(143) Tress, W.; Yavari, M.; Domanski, K.; Yadav, P.; Niesen, B.; Correa Baena, J. P.; Hagfeldt, A.; Graetzel, M. Interpretation and Evolution of Open-Circuit Voltage, Recombination, Ideality Factor and Subgap Defect States during Reversible Light-Soaking and Irreversible Degradation of Perovskite Solar Cells. *Energy and Environmental Science* **2018**, *11* (1), 151–165. https://doi.org/10.1039/c7ee02415k.

(144) Vandewal, K.; Benduhn, J.; Nikolis, V. C. How to Determine Optical Gaps and Voltage Losses in Organic Photovoltaic Materials. *Sustainable Energy and Fuels* **2018**, *2* (3), 538–544. https://doi.org/10.1039/c7se00601b.

(145) Vandewal, K.; Tvingstedt, K.; Gadisa, A.; Inganäs, O.; Manca, J. V. Relating the Open-Circuit Voltage to Interface Molecular Properties of Donor:Acceptor Bulk Heterojunction Solar Cells. *Physical Review B - Condensed Matter and Materials Physics* **2010**, *81* (12), 1–8. https://doi.org/10.1103/PhysRevB.81.125204.

(146) Liu, Z.; Krückemeier, L.; Krogmeier, B.; Klingebiel, B.; Márquez, J. A.; Levcenko, S.; Öz, S.; Mathur, S.; Rau, U.; Unold, T.; Kirchartz, T. Open-Circuit Voltages Exceeding 1.26 v in Planar Methylammonium Lead Iodide Perovskite Solar Cells. *ACS Energy Letters* **2019**, *4* (1), 110–117. https://doi.org/10.1021/acsenergylett.8b01906.

(147) Yao, J.; Kirchartz, T.; Vezie, M. S.; Faist, M. A.; Gong, W.; He, Z.; Wu, H.; Troughton, J.; Watson, T.; Bryant, D.; Nelson, J. Quantifying Losses in Open-Circuit Voltage in Solution-Processable Solar Cells. *Physical Review Applied* **2015**, *4* (1), 1–10. https://doi.org/10.1103/PhysRevApplied.4.014020.

(148) Lipomi, D. J.; Chong, H.; Vosgueritchian, M.; Mei, J.; Bao, Z. Toward Mechanically Robust and Intrinsically Stretchable Organic Solar Cells: Evolution of Photovoltaic

Properties with Tensile Strain. *Solar Energy Materials and Solar Cells* **2012**, *107*, 355–365. https://doi.org/10.1016/j.solmat.2012.07.013.

(149) Tang, Z.; Wang, J.; Melianas, A.; Wu, Y.; Kroon, R.; Li, W.; Ma, W.; Andersson, M. R.; Ma, Z.; Cai, W.; Tress, W.; Inganäs, O. Relating Open-Circuit Voltage Losses to the Active Layer Morphology and Contact Selectivity in Organic Solar Cells. *Journal of Materials Chemistry A* **2018**, *6* (26), 12574–12581. https://doi.org/10.1039/c8ta01195h.

(150) Azzouzi, M.; Yan, J.; Kirchartz, T.; Liu, K.; Wang, J.; Wu, H.; Nelson, J. Nonradiative Energy Losses in Bulk-Heterojunction Organic Photovoltaics. *Physical Review X* **2018**, *8* (3), 31055. https://doi.org/10.1103/PhysRevX.8.031055.

(151) Kotova, M.; Londi, G.; Junker, J.; Dietz, S.; Privitera, A.; Tvingstedt, K.; Beljonne, D.; Sperlich, A.; Dyakonov, V. On the Absence of Triplet Exciton Loss Pathways in Non-Fullerene Acceptor Based Organic Solar Cells. *Materials Horizons* **2020**, *7* (6), 1641–1649. https://doi.org/10.1039/D0MH00286K.

(152) Eisner, F. D.; Azzouzi, M.; Fei, Z.; Hou, X.; Anthopoulos, T. D.; Dennis, T. J. S.; Heeney, M.; Nelson, J. Hybridization of Local Exciton and Charge-Transfer States Reduces Nonradiative Voltage Losses in Organic Solar Cells. *J Am Chem Soc* **2019**, *141* (15), 6362–6374. https://doi.org/10.1021/jacs.9b01465.

(153) Yang, W.; Wang, W.; Wang, Y.; Sun, R.; Guo, J.; Li, H.; Shi, M.; Guo, J.; Wu, Y.; Wang, T.; Lu, G.; Brabec, C. J.; Li, Y.; Min, J. Balancing the Efficiency, Stability, and Cost Potential for Organic Solar Cells via a New Figure of Merit. *Joule* **2021**, *5* (5), 1209–1230. https://doi.org/10.1016/j.joule.2021.03.014.

(154) Baran, D.; Ashraf, R. S.; Hanifi, D. A.; Abdelsamie, M.; Gasparini, N.; Röhr, J. A.; Holliday, S.; Wadsworth, A.; Lockett, S.; Neophytou, M.; Emmott, C. J. M. M.; Nelson, J.; Brabec, C. J.; Amassian, A.; Salleo, A.; Kirchartz, T.; Durrant, J. R.; McCulloch, I. Reducing the Efficiency-Stability-Cost Gap of Organic Photovoltaics with Highly Efficient and Stable Small Molecule Acceptor Ternary Solar Cells. *Nature Materials* **2017**, *16* (3), 363–369. https://doi.org/10.1038/nmat4797.

(155) Lee, T. H.; Park, S. Y.; Walker, B.; Ko, S.-J.; Heo, J.; Woo, H. Y.; Choi, H.; Kim, J. Y. A Universal Processing Additive for High-Performance Polymer Solar Cells. *RSC Advances* **2017**, *7* (13), 7476–7482. https://doi.org/10.1039/C6RA27944A.

(156) Machui, F.; Maisch, P.; Burgués-Ceballos, I.; Langner, S.; Krantz, J.; Ameri, T.; Brabec, C. J. Classification of Additives for Organic Photovoltaic Devices. *ChemPhysChem* **2015**, *16* (6), 1275–1280. https://doi.org/10.1002/cphc.201402734.

(157) Chang, L.; Jacobs, I. E.; Augustine, M. P.; Moulé, A. J. Correlating Dilute Solvent Interactions to Morphology and OPV Device Performance. *Organic Electronics* **2013**, *14* (10), 2431–2443. https://doi.org/10.1016/j.orgel.2013.06.016.

(158) Fontana, M. T.; Kang, H.; Yee, P. Y.; Fan, Z.; Hawks, S. A.; Schelhas, L. T.; Subramaniyan, S.; Hwang, Y.-J.; Jenekhe, S. A.; Tolbert, S. H.; Schwartz, B. J. Low-

Vapor-Pressure Solvent Additives Function as Polymer Swelling Agents in Bulk Heterojunction Organic Photovoltaics. *The Journal of Physical Chemistry C* **2018**, *122* (29), 16574–16588. https://doi.org/10.1021/acs.jpcc.8b04192.

(159) van Franeker, J. J.; Turbiez, M.; Li, W.; Wienk, M. M.; Janssen, R. A. J. A Real-Time Study of the Benefits of Co-Solvents in Polymer Solar Cell Processing. *Nature Communications* **2015**, *6*. https://doi.org/10.1038/NCOMMS7229.

(160) Tournebize, A.; Rivaton, A.; Peisert, H.; Chassé, T. The Crucial Role of Confined Residual Additives on the Photostability of P3HT:PCBM Active Layers. *Journal of Physical Chemistry C* **2015**, *119* (17), 9142–9148. https://doi.org/10.1021/ACS.JPCC.5B01733/SUPPL_FILE/JP5B01733_SI_001.PDF.

(161) McDowell, C.; Abdelsamie, M.; Toney, M. F.; Bazan, G. C. Solvent Additives: Key Morphology-Directing Agents for Solution-Processed Organic Solar Cells. *Advanced Materials*. Wiley-VCH Verlag August 16, 2018. https://doi.org/10.1002/adma.201707114.

(162) Yu, R.; Yao, H.; Hong, L.; Qin, Y.; Zhu, J.; Cui, Y.; Li, S.; Hou, J. Design and Application of Volatilizable Solid Additives in Non-Fullerene Organic Solar Cells. *Nature Communications 2018 9:1* **2018**, *9* (1), 1–9. https://doi.org/10.1038/s41467-018-07017-z.

(163) Song, X.; Zhang, K.; Guo, R.; Sun, K.; Zhou, Z.; Huang, S.; Huber, L.; Reus, M.; Zhou, J.; Schwartzkopf, M.; Roth, S. v; Liu, W.; Liu, Y.; Zhu, W.; Müller-Buschbaum, P.; Song, X.; Zhang, K.; Zhou, Z.; Liu, Y.; Zhu, W.; Guo, R.; Sun, K.; Huber, L.; Reus, M.; Zhou, J.; Müller-Buschbaum, P.; Huang, S.; Liu, W.; Schwartzkopf, M.; Roth, S. v; Maier-Leibnitz-Zentrum, H. Process-Aid Solid Engineering Triggers Delicately Modulation of Y-Series Non-Fullerene Acceptor for Efficient Organic Solar Cells. *Advanced Materials* **2022**, 2200907. https://doi.org/10.1002/ADMA.202200907.

(164) Chen, F.; Zhang, Y.; Wang, Q.; Gao, M.; Kirby, N.; Peng, Z.; Deng, Y.; Li, M.; Ye, L. High Tg Polymer Insulator Yields Organic Photovoltaic Blends with Superior Thermal Stability at 150 OC. *Chinese Journal of Chemistry* **2021**, *39* (9), 2570–2578. https://doi.org/10.1002/cjoc.202100270.

(165) Sun, Y. P.; Cui, C. H.; Li, Y. F.; Wang, H.; Sun, Y.; Cui, C.; Wang, H.; Li, Y. Efficiency Enhancement of Polymer Solar Cells Based on Poly(3-Hexylthiophene)/Indene-C70 Bisadduct via Methylthiophene Additive. *Advanced Energy Materials* **2011**, *1* (6), 1058–1061. https://doi.org/10.1002/AENM.201100378.

(166) Kitchen, B.; Awartani, O.; Kline, R. J.; McAfee, T.; Ade, H.; O'Connor, B. T. Tuning Open-Circuit Voltage in Organic Solar Cells with Molecular Orientation. *ACS Applied Materials and Interfaces* **2015**, *7* (24), 13208–13216. https://doi.org/10.1021/AM508855S/SUPPL_FILE/AM508855S_SI_001.PDF.

(167) Manley, E. F.; Strzalka, J.; Fauvell, T. J.; Jackson, N. E.; Leonardi, M. J.; Eastham, N. D.; Marks, T. J.; Chen, L. X.; Manley, E. F.; Fauvell, T. J.; Jackson, N. E.; Leonardi, M. J.; Eastham, N. D.; Marks, T. J.; Chen, L. X.; Strzalka, J. In Situ GIWAXS Analysis of Solvent and Additive Effects on PTB7 Thin Film Microstructure Evolution during Spin

Coating. *Advanced Materials* **2017**, *29* (43), 1703933. https://doi.org/10.1002/ADMA.201703933.

(168) Campoy-Quiles, M.; Ferenczi, T.; Agostinelli, T.; Etchegoin, P. G.; Kim, Y.; Anthopoulos, T. D.; Stavrinou, P. N.; Bradley, D. D. C.; Nelson, J. Morphology Evolution via Self-Organization and Lateral and Vertical Diffusion in Polymer:Fullerene Solar Cell Blends. *Nature Materials 2008 7:2* **2008**, *7* (2), 158–164. https://doi.org/10.1038/NMAT2102.

(169) Kim, J. S.; Park, J. H.; Lee, J. H.; Jo, J.; Kim, D. Y.; Cho, K. Control of the Electrode Work Function and Active Layer Morphology via Surface Modification of Indium Tin Oxide for High Efficiency Organic Photovoltaics. *Applied Physics Letters* **2007**, *91* (11), 112111. https://doi.org/10.1063/1.2778548.

(170) Li, M.; Li, J.; Yu, L.; Zhang, Y.; Dai, Y.; Chen, R.; Huang, W. Trap-Filling of ZnO Buffer Layer for Improved Efficiencies of Organic Solar Cells. *Frontiers in Chemistry* **2020**, *8*. https://doi.org/10.3389/fchem.2020.00399.

(171) Moreira, N. H.; Domiinguez, A.; Frauenheim, T.; da Rosa, A. L. On the Stabilization Mechanisms of Organic Functional Groups on ZnO Surfaces. *Physical Chemistry Chemical Physics* **2012**, *14* (44), 15445–15451. https://doi.org/10.1039/C2CP42435E.

(172) Perkins, C. L. Molecular Anchors for Self-Assembled Monolayers on Zno: A Direct Comparison of the Thiol and Phosphonic Acid Moieties. *Journal of Physical Chemistry C* **2009**, *113* (42), 18276–18286. https://doi.org/10.1021/JP906013R/ASSET/IMAGES/LARGE/JP-2009-06013R_0012.JPEG.

(173) Liang, Q.; Yao, J.; Hu, Z.; Wei, P.; Lu, H.; Yin, Y.; Wang, K.; Liu, J. Recent Advances of Film–Forming Kinetics in Organic Solar Cells. *Energies*. MDPI November 1, 2021. https://doi.org/10.3390/en14227604.

(174) Tress, W.; Corvers, S.; Leo, K.; Riede, M. Investigation of Driving Forces for Charge Extraction in Organic Solar Cells: Transient Photocurrent Measurements on Solar Cells Showing S-Shaped Current–Voltage Characteristics. *Advanced Energy Materials* **2013**, *3* (7), 873–880. https://doi.org/10.1002/AENM.201200931.

(175) Cai, W.; Österberg, T.; Jafari, M. J.; Musumeci, C.; Wang, C.; Zuo, G.; Yin, X.; Luo, X.; Johansson, J.; Kemerink, M.; Ouyang, L.; Ederth, T.; Inganäs, O. Dedoping-Induced Interfacial Instability of Poly(Ethylene Imine)s-Treated PEDOT:PSS as a Low-Work-Function Electrode. *Journal of Materials Chemistry C* **2019**, *8* (1), 328–336. https://doi.org/10.1039/c9tc05018c.

(176) Son, S. Y.; Samson, S.; Siddika, S.; O’Connor, B. T.; You, W. Thermocleavage of Partial Side Chains in Polythiophenes Offers Appreciable Photovoltaic Efficiency and Significant Morphological Stability. *Chemistry of Materials* **2021**, *33* (12), 4745–4756. https://doi.org/10.1021/ACS.CHEMMATER.1C01305/SUPPL_FILE/CM1C01305_SI_001.PDF.

(177) Gevorgyan, S. A.; Madsen, M. v.; Roth, B.; Corazza, M.; Hösel, M.; Søndergaard, R. R.; Jørgensen, M.; Krebs, F. C. Lifetime of Organic Photovoltaics: Status and Predictions. *Advanced Energy Materials* **2016**, *6* (2), 1501208. https://doi.org/10.1002/AENM.201501208.

(178) Brabec, C. J.; Distler, A.; Du, X.; Egelhaaf, H.-J.; Hauch, J.; Heumueller, T.; Li, N. Material Strategies to Accelerate OPV Technology Toward a GW Technology. *Advanced Energy Materials* **2020**, *10* (43), 2001864. https://doi.org/10.1002/AENM.202001864.

(179) Ye, L.; Hu, H.; Ghasemi, M.; Wang, T.; Collins, B. A.; Kim, J.-H. H.; Jiang, K.; Carpenter, J. H.; Li, H.; Li, Z.; McAfee, T.; Zhao, J.; Chen, X.; Lai, J. L. Y.; Ma, T.; Bredas, J.-L. L.; Yan, H.; Ade, H. Quantitative Relations between Interaction Parameter, Miscibility and Function in Organic Solar Cells. *Nature Materials* **2018**, *17* (3), 253–260. https://doi.org/10.1038/s41563-017-0005-1.

(180) Ye, L.; Li, S.; Liu, X.; Zhang, S.; Ghasemi, M.; Xiong, Y.; Hou, J.; Ade, H. Quenching to the Percolation Threshold in Organic Solar Cells. *Joule* **2019**, *3* (2), 443–458. https://doi.org/10.1016/j.joule.2018.11.006.

(181) Rumer, J. W.; McCulloch, I. Organic Photovoltaics: Crosslinking for Optimal Morphology and Stability. *Materials Today* **2015**, *18* (8), 425–435. https://doi.org/10.1016/j.mattod.2015.04.001.

(182) Kahle, F. J.; Saller, C.; Köhler, A.; Strohriegl, P. Crosslinked Semiconductor Polymers for Photovoltaic Applications. *Advanced Energy Materials* **2017**, *7* (16). https://doi.org/10.1002/aenm.201700306.

(183) He, D.; Du, X.; Zhang, W.; Xiao, Z.; Ding, L. Improving the Stability of P3HT/PC61BM Solar Cells by a Thermal Crosslinker. *Journal of Materials Chemistry A* **2013**, *1* (14), 4589–4594. https://doi.org/10.1039/c3ta01525d.

(184) Wu, S. C.; Strover, L. T.; Yao, X.; Chen, X. Q.; Xiao, W. J.; Liu, L. N.; Wang, J.; Visoly-Fisher, I.; Katz, E. A.; Li, W. S. UV-Cross-Linkable Donor-Acceptor Polymers Bearing a Photostable Conjugated Backbone for Efficient and Stable Organic Photovoltaics. *ACS Applied Materials and Interfaces* **2018**, *10* (41), 35430–35440. https://doi.org/10.1021/acsami.8b11506.

(185) Wantz, G.; Derue, L.; Dautel, O.; Rivaton, A.; Hudhomme, P.; Dagron-Lartigau, C. Stabilizing Polymer-Based Bulk Heterojunction Solar Cells via Crosslinking. *Polymer International* **2014**, *63* (8), 1346–1361. https://doi.org/10.1002/pi.4712.

(186) Griffini, G.; Douglas, J. D.; Piliego, C.; Holcombe, T. W.; Turri, S.; Fréchet, J. M. J.; Mynar, J. L. Long-Term Thermal Stability of High-Efficiency Polymer Solar Cells Based on Photocrosslinkable Donor-Acceptor Conjugated Polymers. *Advanced Materials* **2011**, *23* (14), 1660–1664. https://doi.org/10.1002/adma.201004743.

(187) Müller, C. On the Glass Transition of Polymer Semiconductors and Its Impact on Polymer Solar Cell Stability. *Chemistry of Materials* **2015**, *27* (8), 2740–2754.

https://doi.org/10.1021/ACS.CHEMMATER.5B00024/ASSET/IMAGES/LARGE/CM-2015-00024G_0003.JPEG.

(188) Guo, C.; Quinn, J.; Sun, B.; Li, Y. An Indigo-Based Polymer Bearing Thermocleavable Side Chains for n-Type Organic Thin Film Transistors. *Journal of Materials Chemistry C* **2015**, *3* (20), 5226–5232. https://doi.org/10.1039/C5TC00512D.

(189) Krebs, F. C.; Spanggaard, H. Significant Improvement of Polymer Solar Cell Stability. *Chemistry of Materials* **2005**, *17* (21), 5235–5237. https://doi.org/10.1021/CM051320Q/SUPPL_FILE/CM051320QSI20050826_010711.PDF.

(190) Rumer, J. W.; Ashraf, R. S.; Eisenmenger, N. D.; Huang, Z.; Meager, I.; Nielsen, C. B.; Schroeder, B. C.; Chabinyc, M. L.; McCulloch, I. Dual Function Additives: A Small Molecule Crosslinker for Enhanced Efficiency and Stability in Organic Solar Cells. *Advanced Energy Materials* **2015**, *5* (9). https://doi.org/10.1002/aenm.201401426.

(191) Liao, H. C.; Ho, C. C.; Chang, C. Y.; Jao, M. H.; Darling, S. B.; Su, W. F. Additives for Morphology Control in High-Efficiency Organic Solar Cells. *Materials Today* **2013**, *16* (9), 326–336. https://doi.org/10.1016/J.MATTOD.2013.08.013.

(192) Fu, J.; Chen, H.; Huang, P.; Yu, Q.; Tang, H.; Chen, S.; Jung, S.; Sun, K.; Yang, C.; Lu, S.; Kan, Z.; Xiao, Z.; Li, G. Eutectic Phase Behavior Induced by a Simple Additive Contributes to Efficient Organic Solar Cells. *Nano Energy* **2021**, *84*. https://doi.org/10.1016/j.nanoen.2021.105862.

(193) Xu, B.; Gopalan, S. A.; Gopalan, A. I.; Muthuchamy, N.; Lee, K. P.; Lee, J. S.; Jiang, Y.; Lee, S. W.; Kim, S. W.; Kim, J. S.; Jeong, H. M.; Kwon, J. B.; Bae, J. H.; Kang, S. W. Functional Solid Additive Modified PEDOT:PSS as an Anode Buffer Layer for Enhanced Photovoltaic Performance and Stability in Polymer Solar Cells. *Scientific Reports* **2017**, *7*. https://doi.org/10.1038/srep45079.

(194) Liu, J.; Kadnikova, E. N.; Liu, Y.; McGehee, M. D.; Fréchet, J. M. J. Polythiophene Containing Thermally Removable Solubilizing Groups Enhances the Interface and the Performance of Polymer-Titania Hybrid Solar Cells. *J Am Chem Soc* **2004**, *126* (31), 9486–9487. https://doi.org/10.1021/JA047452M/SUPPL_FILE/JA047452MSI20040622_035123.PDF.

(195) Gevorgyan, S. A.; Krebs, F. C. Bulk Heterojunctions Based on Native Polythiophene. *Chemistry of Materials* **2008**, *20* (13), 4386–4390. https://doi.org/10.1021/CM800431S/SUPPL_FILE/CM800431S-FILE002.PDF.

(196) Bjerring, M.; Nielsen, J. S.; Siu, A.; Nielsen, N. C.; Krebs, F. C. An Explanation for the High Stability of Polycarboxythiophenes in Photovoltaic Devices-A Solid-State NMR Dipolar Recoupling Study. *Solar Energy Materials and Solar Cells* **2008**, *92* (7), 772–784. https://doi.org/10.1016/j.solmat.2007.11.008.

(197) Kularatne, R. S.; Magurudeniya, H. D.; Sista, P.; Biewer, M. C.; Stefan, M. C. Donor-Acceptor Semiconducting Polymers for Organic Solar Cells. https://doi.org/10.1002/pola.26425.

(198) Foster, S.; Deledalle, F.; Mitani, A.; Kimura, T.; Kim, K. B.; Okachi, T.; Kirchartz, T.; Oguma, J.; Miyake, K.; Durrant, J. R.; Doi, S.; Nelson, J. Electron Collection as a Limit to Polymer:PCBM Solar Cell Efficiency: Effect of Blend Microstructure on Carrier Mobility and Device Performance in PTB7:PCBM. *Advanced Energy Materials* **2014**, *4* (14), 1400311. https://doi.org/10.1002/AENM.201400311.

(199) Mahmood, A.; Wang, J. A Review of Grazing Incidence Small- and Wide-Angle X-Ray Scattering Techniques for Exploring the Film Morphology of Organic Solar Cells. *Solar RRL* **2020**, *4* (10), 2000337. https://doi.org/10.1002/solr.202000337.

(200) Liang, Z.; Li, M.; Wang, Q.; Qin, Y.; Stuard, S. J.; Peng, Z.; Deng, Y.; Ade, H.; Ye, L.; Geng, Y. Optimization Requirements of Efficient Polythiophene:Nonfullerene Organic Solar Cells. *Joule* **2020**, *4* (6), 1278–1295. https://doi.org/10.1016/J.JOULE.2020.04.014.

(201) Sun, Y.; Han, Y.; Liu, J. Controlling PCBM Aggregation in P3HT/PCBM Film by a Selective Solvent Vapor Annealing. *Chinese Science Bulletin* **2013**, *58* (22), 2767–2774. https://doi.org/10.1007/s11434-013-5944-6.

(202) Dazzi, A.; Prater, C. B.; Hu, Q.; Chase, D. B.; Rabolt, J. F.; Marcott, C. AFM-IR: Combining Atomic Force Microscopy and Infrared Spectroscopy for Nanoscale Chemical Characterization. *Appl Spectrosc* **2012**, *66* (12), 1365–1384. https://doi.org/10.1366/12-06804.

(203) Meitzner, R.; Faber, T.; Alam, S.; Amand, A.; Roesch, R.; Büttner, M.; Herrmann-Westendorf, F.; Presselt, M.; Ciammaruchi, L.; Visoly-Fisher, I.; Veenstra, S.; Diaz de Zerio, A.; Xu, X.; Wang, E.; Müller, C.; Troshin, P.; Hager, M. D.; Köhn, S.; Dusza, M.; Krassas, M.; Züfle, S.; Kymakis, E.; Katz, E. A.; Berson, S.; Granek, F.; Manceau, M.; Brunetti, F.; Polino, G.; Schubert, U. S.; Lira-Cantu, M.; Hoppe, H. Impact of P3HT Materials Properties and Layer Architecture on OPV Device Stability. *Solar Energy Materials and Solar Cells* **2019**, *202*. https://doi.org/10.1016/j.solmat.2019.110151.

(204) Hexemer, A.; Bras, W.; Glossinger, J.; Schaible, E.; Gann, E.; Kirian, R.; MacDowell, A.; Church, M.; Rude, B.; Padmore, H. A SAXS/WAXS/GISAXS Beamline with Multilayer Monochromator. *Journal of Physics: Conference Series* **2010**, *247* (1), 012007. https://doi.org/10.1088/1742-6596/247/1/012007.

(205) Gann, E.; Young, A. T.; Collins, B. A.; Yan, H.; Nasiatka, J.; Padmore, H. A.; Ade, H.; Hexemer, A.; Wang, C. Soft X-Ray Scattering Facility at the Advanced Light Source with Real-Time Data Processing and Analysis. *Review of Scientific Instruments* **2012**, *83* (4), 045110. https://doi.org/10.1063/1.3701831.

(206) Hughes, M. P.; Rosenthal, K. D.; Ran, N. A.; Seifrid, M.; Bazan, G. C.; Nguyen, T. Determining the Dielectric Constants of Organic Photovoltaic Materials Using Impedance

Spectroscopy. *Advanced Functional Materials* **2018**, *28* (32), 1801542.
https://doi.org/10.1002/adfm.201801542.